A High Resolution View of Galactic Centers: Arp 220 and M31

A DISSERTATION SUBMITTED TO THE GRADUATE DIVISION OF THE UNIVERSITY OF HAWAIʻI AT MĀNOA IN PARTIAL FULFILLMENT OF THE REQUIREMENTS FOR THE DEGREE OF

DOCTOR OF PHILOSOPHY

IN

ASTRONOMY

August 2017

By
Kelly E. Lockhart

Dissertation Committee:

Jessica Lu, Chairperson
Joshua Barnes
Kimberly Binsted
Lisa Kewley
Rolf Kudritzki

Acknowledgements

This work would not be possible without my advisor, Jessica Lu. To her endless credit, when I knocked on her door looking for an advisor before she'd even officially taken up her faculty position, she took me on as her first PhD student. Through the vagaries of science and the TAC, we figured this thing out together. I'm grateful to her for our sometimes meandering science discussions, her unwavering financial support, her ability to ground my occasional scientific flights of fancy, and her encouragement of my non-traditional career goals. I wouldn't be the scientist I am today without her.

I'd also like to thank my committee: Lisa Kewley, my first advisor who helped set me up for future success with her support and encouragement; and Josh Barnes, Rolf Kudritzki, and Kim Binsted, who have been nothing but supportive as this project has grown and changed.

I'm grateful to my collaborators Hiranya Peiris, Mark Allen, and the OSIRIS Pipeline Working Group. Of the latter, I'd especially like to thank Tuan Do, James Larkin, and Shelley Wright. All of my collaborators have helped to make my work stronger and I'm grateful for their attention and care for our work.

I couldn't have made it through my time in grad school without the support and friendship of my fellow grad students. I'd especially like to thank my former housemates Lauren Zuckerberg, Dani Atkinson, Louis Scuderi, and Bon Huang, and the others in my cohort: Will Best, Yanxia Li, Hyewon Suh, Po-Feng Wu, and Li-Yen Hsu. We stumbled through those early grad school years together and managed to also occasionally have some fun. I'd also like to thank Evan Sinukoff and Kelly Blumenthal for getting me out of my

office for occasional coffee breaks, and Matt Hosek for his willingness to almost always let me pick where we were going for group lunch. I'd also like to thank former IfA postdocs Caitlin Casey and Nicholas McConnell for providing their grown-up scientific advice and for also always being up for adventures.

My family and friends have been a rock for these last six years, even if they don't quite know what I've been working on all this time. I'd especially like to thank my parents, Steve and Janie Lockhart, and my sister Nikki for their love and encouragement, and my non-astronomy friends near and far, who occasionally let me pretend that I didn't have work I should be doing.

And thanks go most of all to Jeff Breitenfeldt. For getting excited about space lasers and for taking care of me when things were hard, for going on adventures with me and for making me laugh, and for being my partner in the best sense of the word. This journey would have been way less fun without you.

Abstract

The centers of galaxy are small in size and yet incredibly complex. They play host to supermassive black holes and nuclear star clusters (NSCs) and are subject to large gas inflows, nuclear starbursts, and active galactic nuclear (AGN) activity. They can also be the launching site for large-scale galactic outflows. However, though these systems are quite important to galactic evolution, observations are quite difficult due to their small size.

Using high spatial resolution narrowband imaging with HST/WFC3 of Arp 220, a late-stage galaxy merger, I discover an ionized gas bubble feature (r = 600 pc) just off the nucleus. The bubble is aligned with both the western nucleus and with the large-scale galactic outflow. Using energetics arguments, I link the bubble with a young, obscured AGN or with an intense nuclear starburst. Given its alignment along the large-scale outflow axis, I argue that the bubble presents evidence for a link between the galactic center and the large-scale outflow.

I also present new observations of the NSC in M31, the closest large spiral galaxy to our own. Using the OSIRIS near-infrared integral field spectrograph (IFS) on Keck, I map the kinematics of the old stellar population in the eccentric disk of the NSC. I compare the observations to models to derive a precession speed of the disk of 0$\pm$5 km s^{-1} pc^{-1}, and hence confirm that winds from the old stellar population may be the source of gas needed to form the young stellar population in the NSC.

Studies of galactic centers are dependent on high spatial resolution observations. In particular, IFSs are ideal instruments for these studies as they provide two-dimensional spectroscopy of the field of view, enabling 2D kinematic studies. I report on work to

characterize and improve the data reduction pipeline of the OSIRIS IFS, and discuss implications for future generations of IFS instrumentation.

Table of Contents

List of Tables

List of Figures

Chapter 1

Background

The centers of galaxies are small in relation to their host galaxy, but their size belies their importance. Most large galaxies contain a supermassive black hole (SMBH, $M_\bullet \sim 10^6$–10^{10} $M_\odot$), which resides at the center of the galaxy. Most smaller galaxies are also host to nuclear star clusters (NSCs, $M_{NSC} \sim 10^4$–10^8 $M_\odot$), some of the densest known stellar clusters. The formation of these NSCs is a mystery: their density and compact size in the presence of strong tidal forces from the SMBH suggests that migration from a larger galactic radius is unlikely. However, though many NSCs host young stellar populations, not all galaxies with a known NSC harbor a nuclear reservoir of molecular gas out of which these massive clusters could form.

Observations have shown a tight relation between the mass of the SMBH and the mass of the host galaxy's bulge (McConnell & Ma 2013), implying that the galaxy and the SMBH grow in concert. In the smallest galaxies, NSCs reside alone at the center of their host galaxies, while in larger galaxies, the SMBH is embedded within the NSC. In these systems, including the mass of the NSC tightens the relation between the mass of the central dense object (SMBH+NSC) and the mass of the host galaxy (Georgiev et al. 2016). The exact mechanism by which the galaxy "knows" about the size of its SMBH and NSC, a system $\sim$1000$\times$ less massive, is unclear.

As implied by the relationship between the size of galaxies and their central regions, the two are kinematically linked. Simulations of merging galaxies show that mergers can induce

large-scale tidal gas inflows into the galactic center, which in turn can trigger a burst of nuclear star formation or fuel active galactic nucleus (AGN) activity (Barnes & Hernquist 1996; Mihos & Hernquist 1996). On the other hand, outflows from AGN can remove gas from galaxies and may quench star formation.

Though the importance of galactic centers to galaxy evolution is clear, the systems are difficult to observe. NSCs have a typical radius of a few pc, while SMBH are even smaller. Many studies rely on unresolved observations; focus on the large-scale effects of galactic centers, such as large-scale galactic winds; or study bright AGN. High spatial resolution observations are needed to truly understand this complex region and its effects on the galaxy as a whole.

In this dissertation, we present high spatial resolution studies of the centers of two nearby galaxies, in order to understand their formation and effects on their galactic hosts. We also explore improvements in instrumentation that have implications for future studies of these complex systems.

1.1 Observing galactic centers: Arp 220 and M31

The purpose of this dissertation is two-fold: first, we use existing high resolution instrumentation to explore the complex centers of two local galaxies. The first, Arp 220, is a prototypical ultraluminous infrared galaxy (ULIRG, $L_{IR} > 10^{12}$ $L_\odot$, Sanders et al. 1988; Soifer et al. 1987) in the final stages of a merger between two similarly sized galaxies. It is host to a young, obscured AGN (Paggi et al. 2013) in at least one of its two closely separated ($0\farcs98 = 368$ pc, Baan & Haschick 1995) SMBH. Merger-induced tidal gas inflows have deposited $\sim 10^{10}$ $M_\odot$ of molecular gas within the inner kpc of the system (Scoville et al. 1997); this dense nuclear disk is home to a 100 pc-scale nuclear starburst (240 ± 30 $M_\odot$ yr^{-1}, Farrah et al. 2003). Arp 220 is also host to a large-scale outflow (Heckman et al. 1987) which has been tentatively observationally linked to the nucleus (Arribas et al. 2001). However, previous observations have not been able to directly link nuclear activity with the large-scale outflow, mostly due to poor spatial resolution in the appropriate bandpasses.

The second galaxy we focus on is M31, the closest large spiral galaxy to our own. Unlike Arp 220, M31 is a quiescent galaxy that shows no AGN activity, nor is it disturbed by recent mergers. However, M31 is host to a large nuclear star cluster (NSC, M$\sim 10^7$ M$_\odot$) in which its SMBH is embedded. Observations show that the structure of the NSC is quite complex and consists of two distinct components. The massive old stellar disk is eccentric ($r \sim 4$ pc, Lauer et al. 1993), with the majority of light off-center from the SMBH. This is due to the eccentric stellar orbits—the stars linger at apoapse, producing a red peak in the surface brightness displaced from the SMBH position. The young nuclear cluster (YNC) is much smaller (M$\sim$4200 M$_\odot$) and much younger ($\sim$200 Myr, Bender et al. 2005) than the eccentric disk. Unlike Arp 220 or our own Galactic center, there is very little molecular gas in the center of M31 (Sofue & Yoshida 1993; Nieten et al. 2006). The origin of the YNC is unknown. A number of long-slit (Kormendy & Bender 1999; Statler et al. 1999; Bender et al. 2005) and integral-field (Bacon et al. 2001; Menezes et al. 2013) spectroscopic studies have studied the NSC, but have been hampered by lack of two-dimensional coverage or limited spatial resolution.

1.2 Improving our view of galactic centers

The second major focus of this dissertation is improving the instrumentation that enables these high resolution observations. In particular, we focus on the OSIRIS (OH Suppressing InfraRed Imaging Spectrograph; Larkin et al. 2006) near-infrared (NIR) integral-field spectrograph (IFS) behind the Adaptive Optics (AO) system at the W. M. Keck Observatory. OSIRIS uses a lenslet array to split the field of view into smaller segments; each patch of light passes through the dispersion grating to produce an independent spectrum ($R \sim 3600$). The resulting data cube provides two-dimensional coverage of a field of view, with a full spectrum recorded for each spatial pixel (spaxel). OSIRIS is behind the AO system and can achieve near-diffraction-limited observations. It's been highly productive over the course of its lifetime, producing the majority of the laser-guide-star AO

extragalactic papers on Keck. The instrument achieved first light in 2005 and, due to the complexity of the output data, was delivered with a fully functioning data reduction pipeline (DRP), the first for an instrument on Keck. However, other than routine maintenance, the DRP hasn't been significantly updated since commissioning. Recent hardware upgrades haven't produced the expected improvement in data quality in the reduced data cubes, and initial testing showed that the likely cause was the DRP.

1.3 Overview of this dissertation

In chapter 2, we present new observations of Arp 220 using narrowband imaging with the Hubble Space Telescope's Wide Field Camera 3 to obtain high spatial resolution optical emission line maps of the system. We report on the discovery of an off-nuclear bubble structure seen in ionized gas and, using energetics arguments, link it to both the high level of activity in the nucleus and to the large-scale galactic outflow.

In chapter 3, we present new NIR observations of M31's nuclear star cluster using the OSIRIS IFS on the Keck telescope, which we use to map the two-dimensional kinematics of the old stellar nuclear eccentric disk with high spatial resolution. We fit models to the data and calculate a precession rate of the disk in order to test star formation theories for the formation of the YNC.

In chapter 4, we report on our efforts to improve the DRP of the OSIRIS instrument. We first characterize the existing DRP and then discuss improvements we have made or that may be possible in the future. We also discuss implications for future IFSs.

In chaper 5, we summarize our results and discuss future directions.

References

Arribas, S., Colina, L., & Clements, D. 2001, ApJ, 560, 160

Baan, W. A. & Haschick, A. D. 1995, ApJ, 454, 745

Bacon, R., Emsellem, E., Combes, F., Copin, Y., Monnet, G., & Martin, P. 2001, A&A, 371, 409

Barnes, J. E. & Hernquist, L. 1996, ApJ, 471, 115

Bender, R., Kormendy, J., Bower, G., Green, R., Thomas, J., Danks, A. C., Gull, T., Hutchings, J. B., Joseph, C. L., Kaiser, M. E., Lauer, T. R., Nelson, C. H., Richstone, D., Weistrop, D., & Woodgate, B. 2005, ApJ, 631, 280

Farrah, D., Afonso, J., Efstathiou, A., Rowan-Robinson, M., Fox, M., & Clements, D. 2003, MNRAS, 343, 585

Georgiev, I. Y., Böker, T., Leigh, N., Lützgendorf, N., & Neumayer, N. 2016, MNRAS, 457, 2122

Heckman, T. M., Armus, L., & Miley, G. K. 1987, AJ, 93, 276

Kormendy, J. & Bender, R. 1999, ApJ, 522, 772

Larkin, J., Barczys, M., Krabbe, A., Adkins, S., Aliado, T., Amico, P., Brims, G., Campbell, R., Canfield, J., Gasaway, T., Honey, A., Iserlohe, C., Johnson, C., Kress, E., LaFreniere, D., Lyke, J., Magnone, K., Magnone, N., McElwain, M., Moon, J., Quirrenbach, A.,

Skulason, G., Song, I., Spencer, M., Weiss, J., & Wright, S. 2006, in Proc. SPIE, Vol. 6269, Society of Photo-Optical Instrumentation Engineers (SPIE) Conference Series, 62691A

Lauer, T. R., Faber, S. M., Groth, E. J., Shaya, E. J., Campbell, B., Code, A., Currie, D. G., Baum, W. A., Ewald, S. P., Hester, J. J., Holtzman, J. A., Kristian, J., Light, R. M., Ligynds, C. R., O'Neil, Jr., E. J., & Westphal, J. A. 1993, AJ, 106, 1436

McConnell, N. J. & Ma, C.-P. 2013, ApJ, 764, 184

Menezes, R. B., Steiner, J. E., & Ricci, T. V. 2013, ApJ, 762, L29

Mihos, J. C. & Hernquist, L. 1996, ApJ, 464, 641

Nieten, C., Neininger, N., Guélin, M., Ungerechts, H., Lucas, R., Berkhuijsen, E. M., Beck, R., & Wielebinski, R. 2006, A&A, 453, 459

Paggi, A., Fabbiano, G., Risaliti, G., Wang, J., & Elvis, M. 2013, ArXiv e-prints

Sanders, D. B., Soifer, B. T., Elias, J. H., Madore, B. F., Matthews, K., Neugebauer, G., & Scoville, N. Z. 1988, ApJ, 325, 74

Scoville, N. Z., Yun, M. S., & Bryant, P. M. 1997, ApJ, 484, 702

Sofue, Y. & Yoshida, S. 1993, ApJ, 417, L63

Soifer, B. T., Sanders, D. B., Madore, B. F., Neugebauer, G., Danielson, G. E., Elias, J. H., Lonsdale, C. J., & Rice, W. L. 1987, ApJ, 320, 238

Statler, T. S., King, I. R., Crane, P., & Jedrzejewski, R. I. 1999, AJ, 117, 894

Chapter 2

HST/WFC3 Observations of an Off-Nuclear Superbubble in Arp 220

Note: This chapter originally appeared as Lockhart et al. (2015), with co-authors Lisa J. Kewley, Jessica R. Lu, Mark G. Allen, David Rupke, Daniela Calzetti, Richard I. Davies, Michael A. Dopita, Hauke Engel, Timothy M. Heckman, Claus Leitherer, and David B. Sanders.

Abstract

We present a high spatial resolution optical and infrared study of the circumnuclear region in Arp 220, a late-stage galaxy merger. Narrowband imaging using HST/WFC3 has resolved the previously observed peak in Hα+[NII] emission into a bubble-shaped feature. This feature measures 1.6" in diameter, or 600 pc, and is only 1" northwest of the western nucleus. The bubble is aligned with the western nucleus and the large-scale outflow axis seen in X-rays. We explore several possibilities for the bubble origin, including a jet or outflow from a hidden active galactic nucleus (AGN), outflows from high levels of star formation within the few hundred pc nuclear gas disk, or an ultraluminous X-ray source. An obscured AGN or high levels of star formation within the inner $\sim$100 pc of the nuclei are favored based on the alignment of the bubble and energetics arguments.

2.1 INTRODUCTION

Galaxy mergers are integral to understanding galaxy evolution. Simulations suggest that major mergers cause large-scale tidal gas inflows, which may fuel nuclear starbursts and active galactic nucleus (AGN) activity (Barnes & Hernquist 1996; Mihos & Hernquist 1996). In later stages, mergers may host young, obscured AGN, which, simulations predict, are gradually uncovered as AGN feedback and high levels of circumnuclear star formation expel the surrounding gas (Barnes & Hernquist 1996; Mihos & Hernquist 1996; Di Matteo et al. 2005; Hopkins et al. 2005; Hopkins & Hernquist 2006). This nuclear activity can, in turn, fuel large-scale galactic outflows (Heckman 2003; Veilleux et al. 2005), which have been observed in many merging systems (Heckman et al. 1990, 2000; Martin 2005; Rupke et al. 2002, 2005a,b,c; Martin 2006; Rich et al. 2010; Rupke & Veilleux 2011, 2013b).

Large-scale outflows in the outer parts of galaxies have been extensively studied. However, the advent of high spatial resolution observations has prompted more recent studies to probe the launch sites, propagation, and escape of these outflows (Rupke & Veilleux 2013a; Emonts et al. 2014; Sakamoto et al. 2014). When observed with sufficient spatial resolution, an outflow still within a galaxy often has complex superbubble or filamentary structure (Veilleux et al. 1994; Forbes et al. 2000; Cecil et al. 2001; Kenney & Yale 2002), created as warmer, high-velocity material ejected from a galaxy's nuclear region interacts with the cooler interstellar medium (ISM). However, these well-shaped structures have thus far not been observed in the turbulent, clumpy ISM of a late-stage merger. In addition, while both the timescale and impact of AGN feedback into the host system have been calculated theoretically (Hopkins et al. 2005; Hopkins & Elvis 2010), both are still observationally uncertain. Investigating an individual late-stage merging system that exhibits both an outflow and a possible obscured AGN may provide clues to this process.

Arp 220 is the closest ultraluminous infrared galaxy (ULIRG, $L_{IR} > 10^{12}$ $L_{\odot}$, Sanders et al. 1988; Soifer et al. 1987). The system has long been recognized as a late-stage merger,

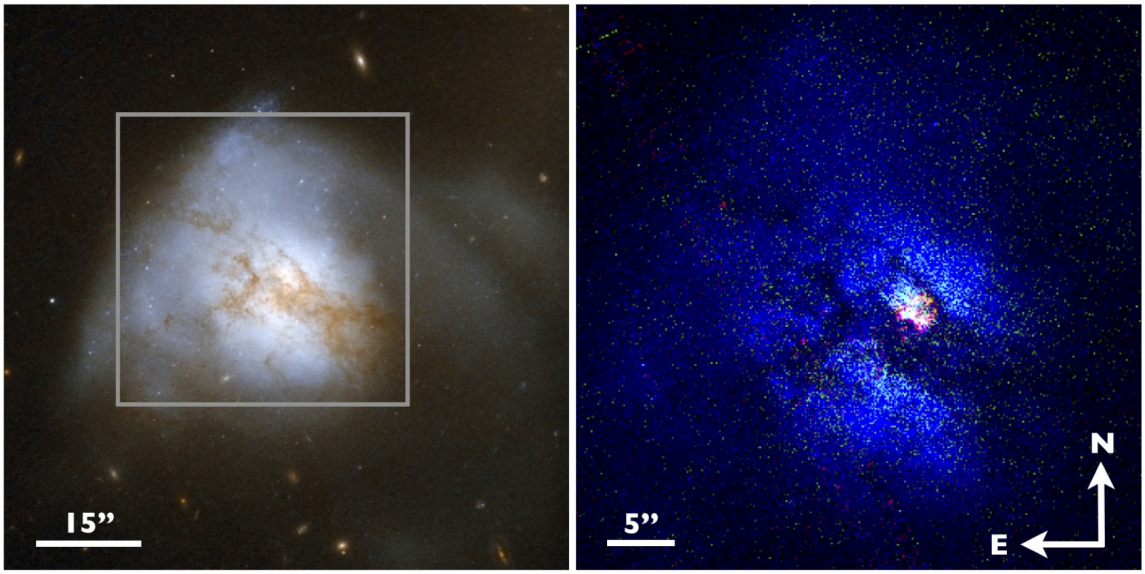

Figure 2.1 *Left: HST* ACS image of Arp 220 as first presented in Wilson et al. (2006), rotated to adjust for the 77° position angle. The blue image is taken with the F435W filter and the red with the F814W filter (green in a linear combination of the red and blue filters). The gray box indicates the FOV of the zoomed right panel. *Right:* Our new data taken with *HST* WFC3. Blue is the F467M blue continuum image, green is [OIII], or the FQ508N image with the blue continuum subtracted, and red is Hα+[NII], or the F665N image with the red continuum subtracted. North is up, east is left.

as evidenced by extended tidal tails visible in the optical (Arp 1966; Surace et al. 2000), infrared (Joseph & Wright 1985), and in HI (Hibbard et al. 2000), as shown in figure 2.1. It also hosts a large–scale outflow that extends far from the galaxy. Arp 220 has a molecular gas mass of $\sim 10^{10}$ $M_\odot$ (Scoville et al. 1997) and a total star formation rate, calculated using the far-infrared luminosity, of 240 ± 30 $M_\odot$ yr^{-1} (Farrah et al. 2003). Most of the molecular gas and star formation are concentrated within a central few hundred pc nuclear gas disk, which also hosts a double nucleus. A possible AGN has been suggested (Paggi et al. 2013) but is still debated. At a distance of 77 Mpc, its close proximity offers a unique laboratory to investigate the interaction of its outflow with the ISM at small spatial scales, and to determine how energy propagates out of the interior of such a system. A more detailed background on the structure of Arp 220 is presented below.

Heckman et al. (1987) observed large-scale (10 kpc) bipolar lobes extending from the galaxy via narrowband Hα imaging, which they interpret as a superwind. Further spectroscopic study revealed these lobes to be superwind-driven bipolar bubbles (Heckman et al. 1990). This superwind is also observed in soft X-ray emission (McDowell et al. 2003).

In addition to the large-scale wind, smaller-scale gas dynamics have been investigated in more recent optical IFU studies. Colina et al. (2004) found large-scale plumes and lobes, up to 8 kpc in length and aligned with the superwind, which are consistent with high-velocity shocks expanding in a neutral medium. Arribas et al. (2001) studied the inner region of the system within 2 kpc of the nuclei and found three gas components. One component is coupled to the central molecular gas disk. The other two components are associated with a biconal outflow or superwind.

This outflow, whether star formation- or AGN-driven, almost certainly originates within the nuclear region of the galaxy. At the center of Arp 220, two dust-enshrouded nuclei, separated by 0.98" (368 pc), are visible in the IR (Scoville et al. 1998), sub-mm (Scoville et al. 1997; Downes & Solomon 1998; Sakamoto et al. 1999; Scoville et al. 2014), and radio (Baan & Haschick 1995). Sakamoto et al. (1999) resolved the large circumnuclear gas mass in a detailed CO study, and found that each nucleus is embedded in its own gas disk, each

roughly 100 pc in radius, and these disks are counterrotating with respect to each other and inclined such that their near sides are to the south. The position angle (P.A.) of each of these small disks is 52° and 263° for the eastern and western nuclei, respectively, while that of the larger circumnuclear disk is 25°. Scoville et al. (2014) calculated the interstellar medium (ISM) masses of each nuclear gas disk, finding a mass of 1.9 (4.2) $\times 10^9$ $M_\odot$ around the eastern (western) nucleus, concentrated within a radius 69 (65) pc of the nucleus. These small gas disks are surrounded by a larger gas disk $\sim$1 kpc in radius, which rotates around the dynamical center of the system (Sakamoto et al. 1999). Mundell et al. (2001) used observations of HI in the circumnuclear gas disks and comparison with simulations to estimate that the merger started about 700 Myr ago, with the second, most recent starburst starting in the western nuclear gas disk more recently than 10–100 Myr ago.

Within the inner 50 pc of each nucleus, the average molecular gas density is $\sim 10^5$ cm^{-3} (Scoville et al. 2014), comparable to the conditions in a dense star-forming core inside a giant molecular cloud. Indeed, Arp 220 is undergoing very high rates of star formation. Smith et al. (1998) estimate the circumnuclear star formation rate at 50–800 $M_\odot$ yr^{-1} using the radio supernovae rate, while Farrah et al. (2003) use the far-infrared luminosity to estimate a global star formation rate of 240$\pm$30 $M_\odot$ yr^{-1}.

Outside of the heavily extincted region near the nuclei, star formation activity was observed with *HST* ACS. Wilson et al. (2006) found two populations of massive star clusters: young (<10 Myr) massive clusters within 2.3 kpc of the nuclei and intermediate age ($\sim$100 Myr) clusters beyond this radius.

In this paper, we investigate the connection between the nuclear energy sources and the large-scale outflow. We use HST/WFC3 with narrowband filters to create the first high spatial resolution optical emission line maps of Arp 220. We present maps of [OIII], Hβ, and Hα+[NII] to resolve gas motions in Arp 220. We discover a bubble feature in Hα+[NII] (section 2.3) and discuss its origins in section 3.6.

Throughout this work, we assume a distance of 77 Mpc, which gives 1"=375 pc.

2.2 OBSERVATIONS

2.2.1 HST

The optical imaging data of Arp 220 used in this work are new observations obtained with HST Wide Field Camera 3 (WFC3-UVIS) on 2012 September 22 (GO-12552, PI: Lisa Kewley). We selected filters whose bandpasses each cover one or more of several strong optical emission lines commonly used for calculating gas-phase metallicity and shock excitation: Hβ (filter FQ492N); [OIII]$\lambda\lambda$ 4959, 5007 (rest) (FQ508N); Hα + [NII]$\lambda\lambda$ 6548, 6583 (F665N); and [SII]$\lambda\lambda$ 6717, 6731 (F680N). Blue (F467M) and red (F621M) continuum exposures were also taken to allow calculation of the line flux across the extent of the system. Figure 2.2 shows the filter bandpasses superimposed over the SDSS 7 spectrum of Arp 220. The filter and exposure data are summarized in Table 4.1 along with the continuum bandpass used with each emission line image and the 1σ RMS errors (discussed further in sections 2.2.1 and 2.2.1) With a pixel size of 0.0396", the field of view (FOV) of WFC3-UVIS is 164" $\times$ 176" as measured on the image. The FQ, or quad, filters, each occupy one-quarter of the FOV, so the FOV for these filters is approximately 82" $\times$ 88".

Data reduction was performed using the STScI pipeline, which utilizes "On-The-Fly Reprocessing" (OTFR). This processes the raw data files using the best calibration files and software available at the time of retrieval from the archive and performs basic bias and dark subtraction and flat fielding. It also flags bad pixels and performs initial cosmic ray removal. The data were all retrieved from the archive in late 2012.

The reduced dithered exposures were combined using AstroDrizzle (Avila et al. 2012). AstroDrizzle, the successor to MultiDrizzle, provides distortion corrections and combines multiple images using a technique which allows for image subsampling. Sky subtraction was performed using the mode of the image, in order to not bias the sky value by the extended nebulosity of the galaxy. Charge transfer efficiency (CTE) trails caused by inefficient electron shuffling during readout were evident on the initial combined images. Due to the high counts involved, they were especially problematic in the pixels along which cosmic

Table 2.1 HST WFC3-UVIS Exposures

Filter	Bandpass Central λ (Å)	Bandpass Width (Å)	Line	Exposures	Continuum Filter	Continuum Scale[a]	Flux Error 1σ[b] (erg s^{-1} cm^{-2} Å^{-1} arcsec^{-2})
FQ492N	4933	114	Hβ	2×1090 s, 6×920 s	F467M	0.42	3.9×10^{-18}
FQ508N	5091	131	[OIII] 4959, 5007	2×1050 s, 6×920 s	F467M	0.46	3.8×10^{-18}
F665N	6656	131	Hα + [NII] 6548, 6583	2×200 s	F621M	0.16	1.4×10^{-17}
F680N	6877	371	[SII][c] 6717, 6731	2×525 s	F621M	0.66	7.7×10^{-18}
F467M	4683	201	blue continuum	2×775 s	...	...	...
F621M	6219	609	red continuum	2×155 s	...	...	...

[a]Scaling factor of the continuum used for continuum subtraction.
[b]Flux errors are estimated based on the dispersion of the sky background in each image, as measured on a section of sky away from the galaxy.
[c]Not used for analysis due to shallowness of image; see Appendix

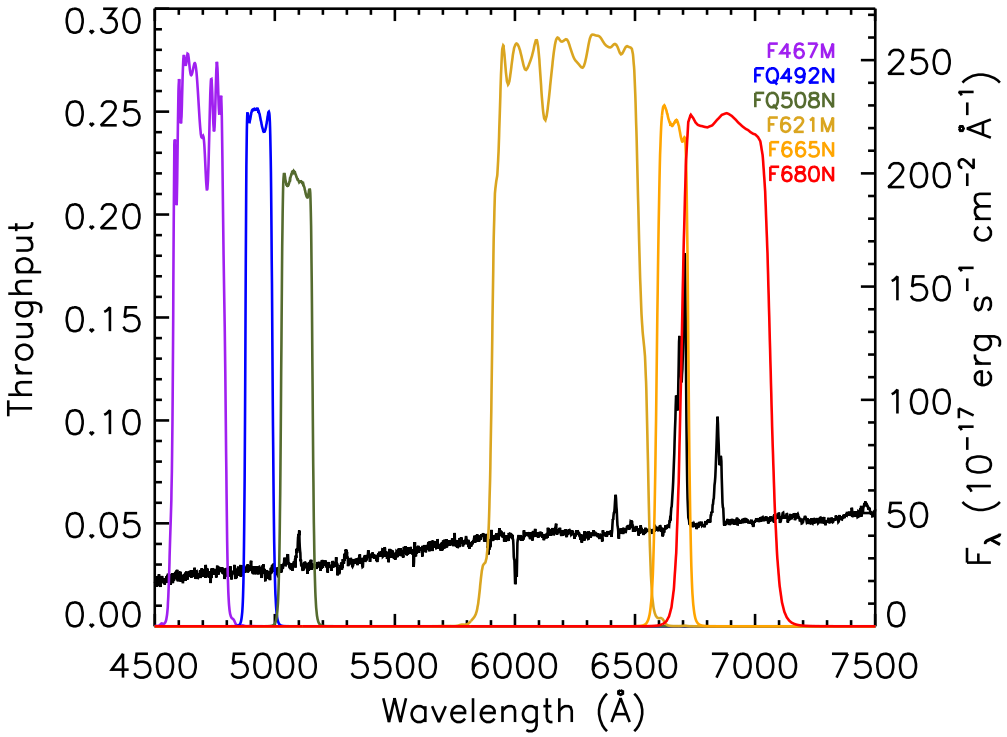

Figure 2.2 SDSS 7 spectrum of Arp 220 with the WFC3-UVIS filter bandpasses overlaid. The left axis shows the throughput of each WFC3 filter (colors are as shown in the legend) while the right axis shows the flux of the SDSS spectrum (in black).

ray hits were shuffled. The charge in the first smeared pixel amounted to roughly 1% of the initial high pixel value and dropped off rapidly as the charge was further shuffled along the detector. However, the CTE trail left by each cosmic ray was up to 20 pixels long for the strongest cosmic rays. These pixels were masked in AstroDrizzle, as the data were downloaded and reduced before the CTE correction software from STScI became available. All other AstroDrizzle parameters were set to the default values. The final combined images were registered to a common reference frame using the AstroDrizzle tasks `tweakreg` and `tweakback` and redrizzled onto the same pixel grid, to allow for image combination.

The FQ492N and FQ508N filters, covering Hβ and [OIII], had a sufficient number of exposures to allow for cosmic ray removal (see table 4.1). The other filters (F467M, F621M, F665N, F680N) had two dithered exposures each; the cosmic ray cleaning provided by AstroDrizzle for these was not robust, especially in the gap between the two detector chips. The final combined images for these filters were further cleaned of cosmic rays using a Laplacian edge detection algorithm, which identifies cosmic rays based on the sharpness of their edges (van Dokkum 2001). This method, which removes only the positive noise spikes, can alter the noise distribution of the image. The resulting noise distribution may be asymmetric and skewed towards negative values, which can be problematic for low signal-to-noise ratio (S/N) regions. We examined the cleaned images and found that only the F665N image is affected. Because we focus on the high S/N regions in this filter, this does not affect our results.

The bandpass of one of the continuum images, through filter F621M, contains [OI]λ 6300Å, a strong emission line in shock-excited gas. The strength of this line varies with metallicity and excitation source and thus could contaminate calculations of emission line ratios. The contribution of the flux of this line to the total flux in the continuum image was estimated using the Sloan Digital Sky Survey (SDSS) spectrum of Arp 220. The SDSS fiber covers the inner 3" of the galaxy, or roughly 1 kpc. The ratio of flux in the emission line to flux in the continuum contained in the bandpass was roughly 1%, or less than the

average error in the images. Thus, the contribution of the line to the continuum image was taken to be negligible and no correction to the continuum image was made.

The data were binned in square bins 3 pixels wide to increase the S/N. At the redshift of 0.018126±0.000023 (de Vaucouleurs et al. 1991), the WFC3 pixel scale of 0.0396"/pixel corresponds to 15 pc. Extragalactic giant HII regions range from 50 to 300 pc in diameter (Oey et al. 2003). The binned resolution elements measure 45 pc across and thus allow full sampling of all but the smallest HII regions while still allowing recovery of low signal.

Continuum Subtraction

One of the most sensitive calibration tasks is subtraction of the stellar continuum from the emission line images. Small changes in the factor used to scale the continuum before subtracting it from the emission line image propagate into a change in the flux of the final emission line image. This can have a large effect on the emission line flux and ratio maps.

We determined the optimal scale factor between the continuum image and the emission line image using the "skewness transition method" (Hong et al. 2014). This method uses the symmetry of the flux distribution within an aperture to identify the ideal scaling factor that neither under nor over subtracts the continuum. It accounts for spatially dependent luminosity changes, but not spatially dependent color changes. The location of the aperture used to calculate the scaling factor influences the derived value, and allows us to estimate an error on the scaling factor. The error on the scaling factor can be taken as 0.05 for each filter.

We verified the accuracy of this method via physical arguments. For a star cluster with zero extinction, and assuming Case B recombination, the ratio of Hα to Hβ is 2.86. However, Arp 220 has high levels of patchy extinction and a high and varying ratio of [NII] to Hα, so we would not expect this ratio to hold across most of this system. We are able to check the ratio between the two images using a star cluster with significant Hα+[NII] and Hβ emission, and a measured E(B-V) of 0 (Wilson et al. 2006, their cluster 62). We assumed that the ratio of [NII] to Hα is roughly that for an HII region ($\sim$0.3, Kewley et al.

2006a) and adjusted the scaling factor for the continuum subtraction from the Hβ image until we achieve a ratio equal to the Balmer decrement. With this method, we calculate a new scaling factor of 0.49±0.02. This scaling factor is generally consistent with that obtained through the skewness transition method (0.42±0.05), and so we adopt the scaling factors from the skewness transition method. Our scaling factors are given in table 4.1.

Error estimation

Flux errors are estimated based on the standard deviation of the background in each image. The dispersion varies slightly across the field, so to obtain a representative value this was measured in a region centered within 2" of the detected emission line flux in each filter, but not overlapping it. We show the 1σ errors in Table 4.1. We adopt a S/N cutoff of 4σ in all emission line images. However, the F680N image was too shallow and we were unable to recover [SII] flux above the 4σ limit (see Appendix). We thus drop this image from further analysis.

2.2.2 Other data

H_2 data

Near-infrared (H and K band) integral field spectroscopy (IFS) data were taken 2007 March 7 and April 18–21 with SINFONI, a NIR integral field spectrometer on the Very Large Telescope (VLT) (Eisenhauer et al. 2003). The curvature-based adaptive optics system was operated in laser guide star mode, though without tip-tilt correction as no suitable tip-tilt star was available. This gave a nearly symmetric Gaussian point spread function of 0.30" × 0.31". The 0.05"×0.10" plate scale was used, giving a FOV of 3.2"×3.2". Further details on the observations, data reduction, and line fitting are given in Engel et al. (2011).

NICMOS

Near-infrared imaging using HST/NICMOS was obtained from the HST archives. The F160W filter on camera NIC2 was used to image Arp 220 in the H-band on 10 January

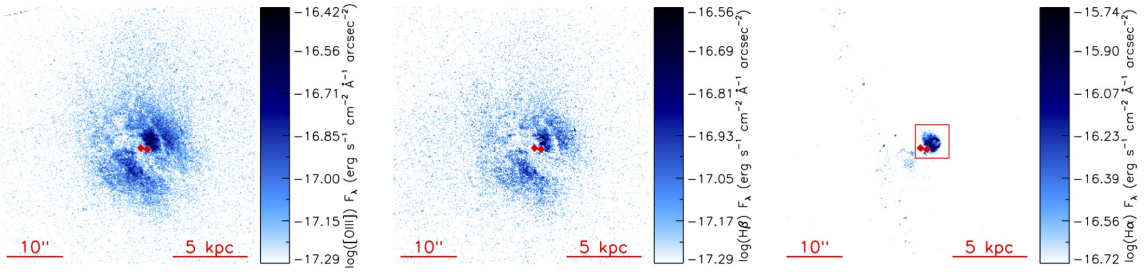

Figure 2.3 Maps of the log([OIII]) (left), log(Hβ) (middle), and log(Hα+[NII]) (right) emission across the galaxy, rotated to account for a 77° P.A. so that north is up and east is left. The locations of the eastern and western nuclei, as determined in the near IR by Scoville et al. (1998) and precessed to J2000.0, are shown as red diamonds. A box, showing the size of the zoomed figure 2.4, is shown on the right panel. A 4σ S/N cut has been applied.

2004 (proposal 9726, PI: R. Maiolino) for a total exposure time of 600 s (Cresci et al. 2007). The F222M filter (K band) on NIC2 was used to image the system on 4 April 1997 for a total exposure time of 1024 s (Scoville et al. 1998, proposal 7116, PI: N. Scoville). The pixel scale on the NIC2 camera is 0.076" while the FOV is 19.2".

2.2.3 Registration

There are no stars suitable for image registration in the field of view (FOV). Instead, bright super star clusters from Wilson et al. (2006) were used to align the WFC3 and NICMOS datasets. Three bright, well-separated clusters were used, allowing a correction for both shift and rotation between the images. The absolute astrometric registration was set by the coordinates of the western nuclei given by Scoville et al. (1998), precessed to J2000.0.

The SINFONI data have a smaller FOV, limited to the circumnuclear region. The optical super star clusters (SSCs) previously used for alignment were out of this FOV. Instead, the IFU data were aligned directly with the NICMOS F222M image using the nuclei and another bright infrared source.

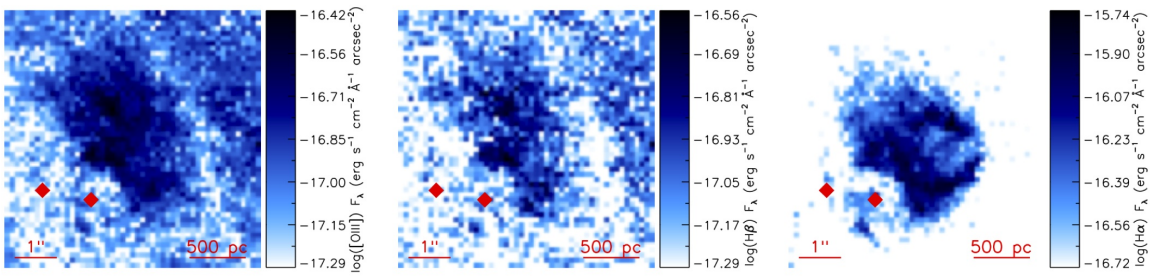

Figure 2.4 Map of the log([OIII]) (left), log(Hβ) (middle), and log(Hα+[NII]) (right) emission near the nuclear region, zoomed in on a central 6" × 6" region. As in the full map, a 4σ S/N cut has been applied, the locations of the eastern and western nuclei are shown as red diamonds, and the maps have been rotated so that north is up and east is left.

2.3 MORPHOLOGY

2.3.1 Optical emission line structure

We present emission line maps of [OIII], Hβ, and Hα+[NII] in figure 2.3. Each image is 45" × 45". A 4σ S/N cut has been applied, and the logarithm of the emission is displayed in order to show the full range of emission. The maps have been rotated to account for a 77° P.A., so that north is up and east is left. The NIR locations of the double nuclei (Scoville et al. 1998) are shown as red diamonds. Some residual cosmic rays are visible in the chip gap of the Hα+[NII] (right) panel figure 2.3, as detailed in section 3.2.

The imaging reveals widespread [OIII] and Hβ emission across the central disk, roughly 8 kpc in diameter. Faint tidal tails are visible to the northeast. A dust lane runs from the northeast to the southwest, obscuring the double nuclei of the system, which are only visible in the X-ray, IR, and radio. Though visible across the main disk of the system, the [OIII] and Hβ emission is concentrated near the optical center, which is roughly 1.5" offset to the northwest from the western nucleus. The Hα+[NII] emission is much more tightly concentrated near the optical center. We also present emission line maps zoomed into the nuclear region in figure 2.4.

The most striking feature in the emission line maps is a ring- or bubble-shaped structure, seen in Hα+[NII] emission (figure 2.4, right panel). It is unclear whether the feature is due

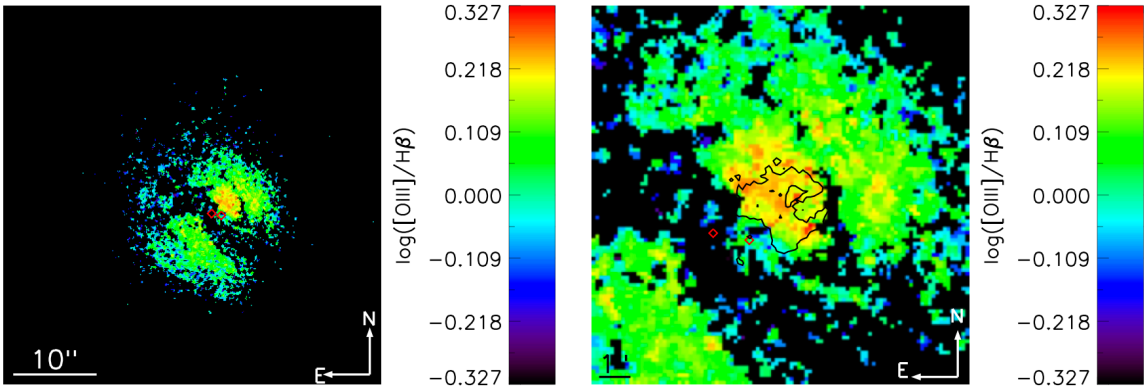

Figure 2.5 Median smoothed maps (kernel=3) of log([OIII]/Hβ). Red diamonds show the positions of the nuclei, identified in the NIR and given in Scoville et al. (1998). *Left:* Full view of system. *Right:* Same as left, but zoomed into the optical center of the system. In addition, contours showing the bubble feature, in Hα+[NII] emission, are shown in black. North is up, east is left in both panels.

to strong emission in [NII], Hα, or both. Strong Hα emission indicates high rates of star formation, while high [NII] emission generally indicates the presence of shocked gas (see Kewley et al. (2006a)). The ring measures 1.6" in diameter, or 600 pc at the distance of Arp 220, with a P.A. of 316° as measured from the western nucleus to the bubble center. There appears to be a faint smaller ring, inside the larger one, on the side closest to the nuclei. This is the first time the Hα and [NII] peaks reported in Arribas et al. (2001, their figure 1, approximately corresponding to their fibers 110–114) have been resolved into a bubble morphology. This bubble feature and its environment are discussed further in section 2.3.3.

2.3.2 Emission line ratios

The ratios of strong optical emission lines are commonly used as a diagnostic to determine the excitation mechanism of ionized gas (Baldwin et al. 1981; Kewley et al. 2001; Kauffmann et al. 2003; Kewley et al. 2006b): photoionization by massive stars, excitation via shocks, or ionization from an AGN. The most widely used diagnostics require the ratio of both [OIII] to Hβ and either [NII], [SII], or [OI]λ 6300Å to Hα.

In figure 2.5, we present maps of log([OIII]/Hβ), which were created from the left and center panels of figure 2.3. A S/N cut of 4σ was first applied to each individual emission line map and the resulting ratio map was smoothed using a median filter (kernel=3) in order to emphasize larger-scale features. The right panel of figure 2.5 is the same, but cropped to more closely show the region around the bubble feature. Hα+[NII] contours are overlaid in black on the right panel, to show the location of the bubble feature.

Some structure is visible in the smoothed maps, and is more readily apparent in the normalized histograms of log([OIII]/Hβ) shown in figure 2.6. Values for the entire system are shown in blue, while values within just the Hα+[NII] ring feature are shown in red. Binned regions are considered part of the ring feature if they fall within 1" of the center of the ring. The mean log([OIII]/Hβ) for the entire system is 0.05$\pm$0.11, or 0.22$\pm$0.07 for the bubble region (shown in blue and red, respectively, above the histograms). The log([OIII]/Hβ) values in the ring feature appear to be slightly higher than in the system as a whole, though the difference is not significant at the 1σ level.

The value of log([OIII]/Hβ) will be used in conjunction with literature values of log([NII]/Hα) to analyze the gas excitation mechanism in section 2.4.2.

2.3.3 The bubble in a multi-wavelength context

In this section, we present the first high spatial resolution multi-wavelength maps of Arp 220 combining optical, NIR, and X-ray images. A 3-color image, shown in figure 2.7, was made using the optical continuum (HST/WFC3 F621M) image, Hα+[NII] emission image, and the H-band continuum (NICMOS F160W) image. In this image, the blue shows the optical stellar continuum, subject to extinction from dust in the system, especially in the circumnuclear region; the green shows the sum of the Hα and [NII] emission lines, which can be excited by recent star formation, shocked gas, or AGN excitation; and the red shows a combination of the near-IR continuum, which is less affected by dust extinction.

The X-ray structure seen on $\sim$10 kpc scales, which traces the hot gas outflow, appears to be roughly aligned with the P.A. of the bubble feature with respect to the western nucleus

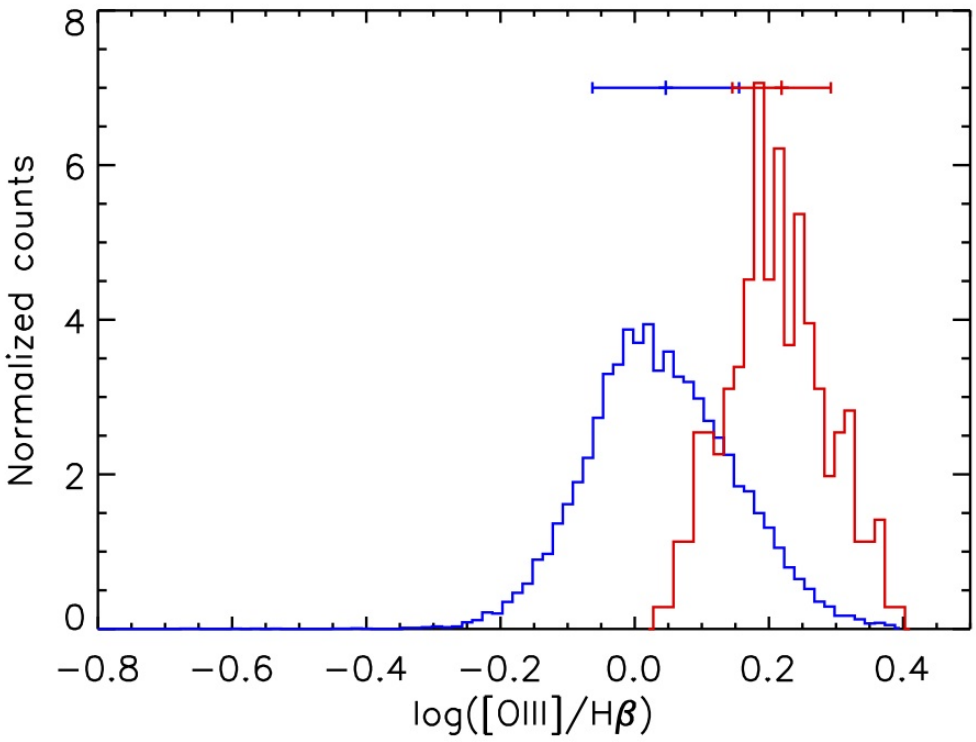

Figure 2.6 Normalized histograms of log([OIII]/Hβ values of the map of Arp 220, so that the area under each histogram is 1. The histogram in blue shows all log([OIII]/Hβ) values across the system (N=18676), while the histogram in red shows only the values within the Hα+[NII] bubble feature region (N=236). The mean and standard deviation of each histogram are shown at top.

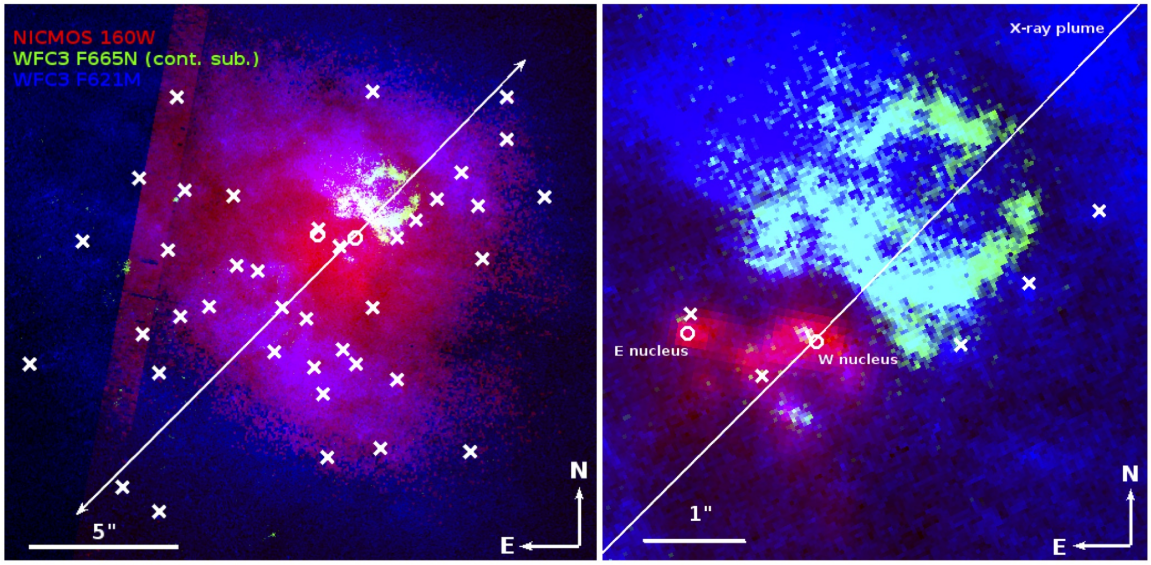

Figure 2.7 3 color image of Arp 220. The blue image shows the optical continuum (HST/WFC3 F621M), the green shows Hα+[NII] (continuum-subtracted HST/WFC3 F665N), and the red shows the H-band infrared continuum (HST/NICMOS F160W). The major axis of the soft X-ray structure (white vector) and locations of the super star clusters (SSCs, white crosses) are indicated. The left panel shows the main disk of the system. The scaling of the red image is adjusted to emphasize the faint emission; the chip gap is visible down the left side of the image. The right image shows the nuclear region, including the double nuclei and the Hα+[NII] bubble feature. The peaks in the infrared mark the positions of the two nuclei, and are shown as white circles. The scaling of the red image has been adjusted to show the structure of the strong emission near the nuclei.

(figure 2.7). Heckman et al. (1996, figure 2) reports a P.A. of 315° for the northwestern plume, while McDowell et al. (2003, figure 1) report a P.A. of 331° for the same feature. However, the structure is wide and faint enough that determining an exact P.A. is difficult. In addition, Heckman et al. (1996) report a large-scale X-ray structure with a P.A. of 285°, which is inconsistent with the P.A. of the bubble feature. In figure 2.7, we show the mid-scale X-ray structure as reported by Heckman et al. (1996). The binned pixel size in the X-ray data (1.5") is too large to resolve whether the outflow is coming from one of the two nuclei or the ∼1 kpc nuclear gas disk. Higher spatial resolution observations reveal a hard X-ray source roughly aligned with the western nucleus (Clements et al. 2002, source X-1). Therefore, we proceed with the assumption that the X-ray outflows originate in the western nucleus.

The southeastern side of the bubble appears to curve around the western nucleus. This curve is echoed by the NIR emission surrounding the western nucleus, which likely traces the circumnuclear disk (Sakamoto et al. 1999). While little optical emission is seen near the nuclei, due to high dust extinction, there are peaks in the optical emission lines (Hα+[NII] and [OIII]) roughly coincident with the NIR nuclei. As the images were registered based on the coordinates of SSCs throughout the galaxy, not the nuclei, this alignment is remarkable.

A gap in the ring feature is evident on the side away from the nuclei, which could be due to either high extinction or an actual gap in emission. If the gap is caused by extinction, and the obscuring material contains hot dust, we would expect to see more NIR emission coincident with the gap. The NIR emission does not peak in this area, indicating that this hole in emission is not due to extinction from material containing hot dust. In addition, the mid-scale northwestern X-ray plume is aligned with this gap, suggesting that a stream of hot X-ray emitting gas is clearing a hole in the optical emission line gas, disrupting the process that formed these lines. This hot gas extends for 10–15 kpc on each side of the nucleus (McDowell et al. 2003).

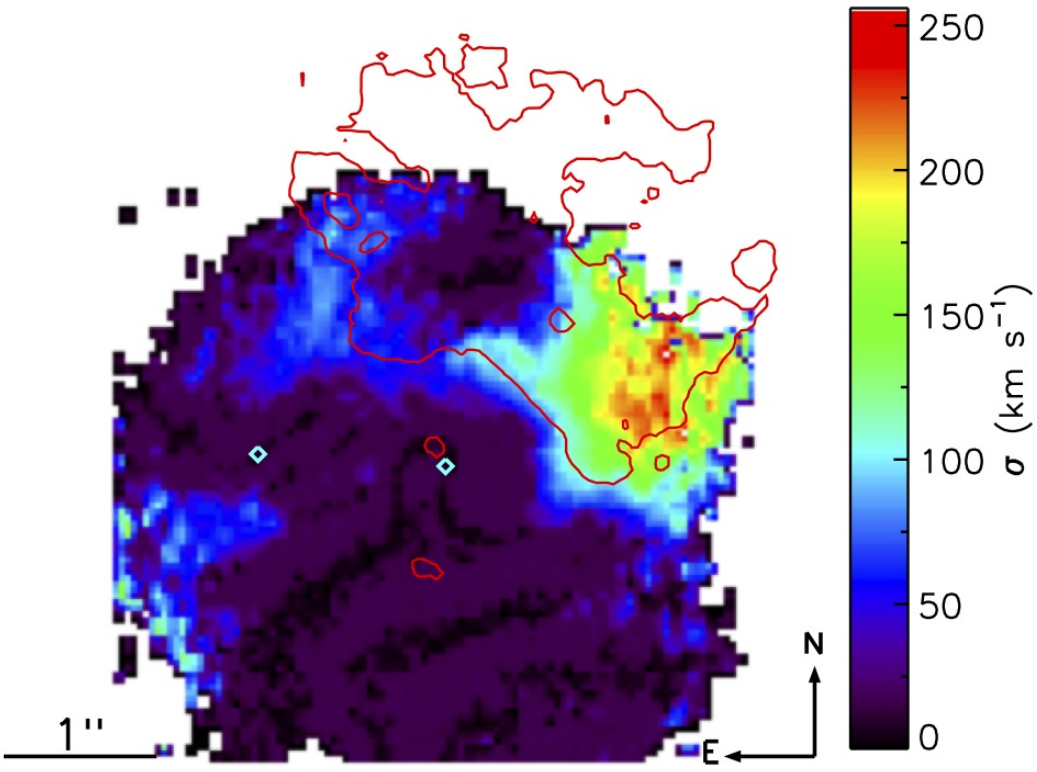

Figure 2.8 NIR velocity dispersion, calculated from the H_2 1-0 S(1) line and corrected for instrumental broadening. Contours show the 7σ Hα+[NII] flux, smoothed for display purposes. The nuclei are marked as cyan diamonds. North is up and east is left.

No SSCs appear to be coincident with the bubble feature. Figure 2.7 shows the locations of the optical and infrared selected SSCs as white crosses (Wilson et al. 2006; Scoville et al. 1998). We discuss this further in section 3.6.

2.3.4 Kinematics from the NIR

Engel et al. (2011) studied the NIR kinematics of the circumnuclear region (r$\sim$1.5", centered on the western nucleus) using the H_2 1-0 S(1) line. The velocity structure presented there shows a clear rotational signature, with the rotational axis roughly in the NW/SE direction. The NIR velocity dispersion map is shown in figure 2.8, with the optical Hα+[NII] flux contours overlaid. This map differs slightly from that presented by Engel et al. (2011) in

that the instrumental broadening has been corrected for here; thus, the dispersion values are slightly lower than those presented earlier. The velocity dispersion of the H_2 is enhanced near the bubble, and reaches a maximum of 250 km s^{-1} at the base of the western arm. The velocity map shows no evidence for a systemic velocity shift at this location, though the rotational axis is not perfectly aligned with the region of enhanced velocity dispersion. This may indicate that the higher velocity dispersion is linked with the bubble feature. If we assume an outflow is launched from a source at the center of the bubble and that the outflow velocity is equal to the peak of the dispersion, then the age of the bubble is $\sim$2.3 Myr. If the powering source is in the nucleus, a kinematic age cannot easily be determined. The current kinematic maps do not cover the bubble's full spatial extent. Additional data are necessary to characterize the dynamics of the region.

2.3.5 Bubble energetics

We estimate the mass and energy in the bubble using $L_{H\alpha}$, and assuming Case B recombination and T=10^4 K (Osterbrock 1989). Using the continuum-subtracted Hα+[NII] image, we find a total integrated flux in the bubble region of 2.6×10^{-14} erg s^{-1} cm^{-2}. With the Hα to Hα+[NII] ratio from the bubble region of the Arribas et al. (2001) IFS study ($\frac{H\alpha}{H\alpha+[NII]}$=0.37), we calculate an ionized gas mass of 2.5×10^7 $M_\odot$ n_e^{-1}.

The Hα flux used here has not yet been corrected for extinction. We can derive the extinction in the bubble region via the Balmer decrement, by taking the ratio of the Hα to Hβ maps and comparing this value to 2.86, the theoretical ratio under Case B recombination. This calculation is very sensitive to the continuum subtraction for Hβ (see section 2.2.1), but we can derive a range of acceptable extinction values based on the error in the continuum subtraction scaling factor. The mean continuum scaling factor for Hβ, 0.42, gives E(B-V)=0.11, though a range in E(B-V) of 0.00–0.48 is also consistent. Given the mean extinction, we derive a dereddened ionized gas mass of M_{ion}=3.2×10^7 $M_\odot$ n_e^{-1}, with a range of 2.5–7.8×10^7 $M_\odot$ n_e^{-1}. We adopt the mass derived from the mean value of the Hβ continuum scaling factor in the following discussion.

The [SII] doublet ratio 6317Å/6331Å can be used to constrain the electron density of the ionized gas. The MPA-JHU SDSS DR7 data product catalog[1] gives a ratio of 1.46, which places n_e in the lower density limit (Osterbrock 1989), or less than $\sim 10^2$ cm^{-3}. Previous work on the ionized bubble in NGC 3079 (Veilleux et al. 1994; Cecil et al. 2001) constrained n_e in that system to 5–100 cm^{-3}. Rupke & Veilleux (2013b) adopt n_e=10 cm^{-3} for their analysis of the ionized winds in a sample of ULIRGs, consistent with the NGC 3079 limits. We adopt n_e=10 cm^{-3} here to facilitate comparison with the literature. Assuming the upper limit of n_e=10 cm^{-3} gives $M_{ion}=3.2\times10^6$ $M_\odot$. Rupke & Veilleux (2013b, Table 6) find ionized gas masses in their sample of ULIRG winds in the range $10^{6.93-8.07}$ $M_\odot$, so the Arp 220 bubble mass is similar to these other ULIRG outflows.

We estimate the kinetic energy in an expanding shell by assuming that the observed velocity dispersion in H_2 represents the shell velocity, or v_{shell}=250 km s^{-1}. We find a kinetic energy of 2.0×10^{54} erg. Given a dynamical age of 2.3 Myr (section 2.3.4) and assuming constant energy injection, we calculate an energy injection rate from the ionized gas mass of 2.8×10^{40} erg s^{-1}.

We are only observing the ionized gas and the neutral gas may be a substantial fraction of the total gas mass in the bubble feature. To include a correction for the neutral hydrogen, we used the measurements of Mundell et al. (2001), who measured hydrogen absorption against the continuum in 1.4 GHz observations. The structure they identify as spur T is coincident with the bubble feature, though they are unable to measure significant H absorption in this region. They place an upper limit of $N_H < 1.3\times10^{20}$ T_s(K) cm^{-2}. With their assumption that T_s = 100 K, that gives an upper limit of $N_H < 1.3\times10^{22}$ cm^{-2}, and an upper limit on the total neutral hydrogen mass in the bubble region of 1.2×10^8 $M_\odot$. Using the same velocity assumptions as for the ionized gas, the upper limit of kinetic energy in the neutral gas is 3.8×10^{55} erg, and the upper limit on the energy injection rate is 5.3×10^{41} erg s^{-1}.

[1] http://www.mpa-garching.mpg.de/SDSS/DR7/

The total neutral+ionized mass in the bubble feature is thus M$<1.2\times10^8$ M$_\odot$, the total kinetic energy is KE$<4.0\times10^{55}$ erg, and the energy injection rate is dE/dt$\sim5.6\times10^{41}$ erg s^{-1}. We compare these rates to possible sources in the following section.

2.4 ORIGIN OF THE BUBBLE

Given the bubble's position and morphology, there are two possible points of origin. First, it could be the product of a jet or outflow originating in one of the two nuclei or the molecular disk immediately surrounding them. Alternatively, the bubble could originate from a source at its center. Either a massive star cluster or a microquasar (i.e. an ultraluminous X-ray source, ULX) could drive a traditional expanding superbubble. Given that the nuclei are deeply embedded in dense gas and are more distant, the energies necessary to drive an outflow from the nuclear disk versus from the bubble's center are very different. We lay out the possibilities in sections 2.4.1 and 2.4.2, and discuss and compare them further in section 2.4.3.

2.4.1 Nuclear origins

The first possibility is that the bubble is being driven from a nucleus or the circumnuclear region, either from an AGN(s) or from a strong nuclear starburst.

Jet or outflow from an AGN(s)

The observed morphology of the bubble feature matches that produced in some AGN jet simulations. Sutherland & Bicknell (2007) modeled the interaction of a light supersonic jet with the inhomogeneous and turbulently supported ISM in an early-type galaxy. Their simulated ISM followed a lognormal single-point density distribution and a power-law density structure, with an average jet/ISM number density ratio of $\sim10^{-2}$. The jet had a kinetic luminosity of $\sim10^{43}$ erg s^{-1}, and radiative cooling was implemented via the MAPPINGS photoionization and shock code (Sutherland & Dopita 1993).

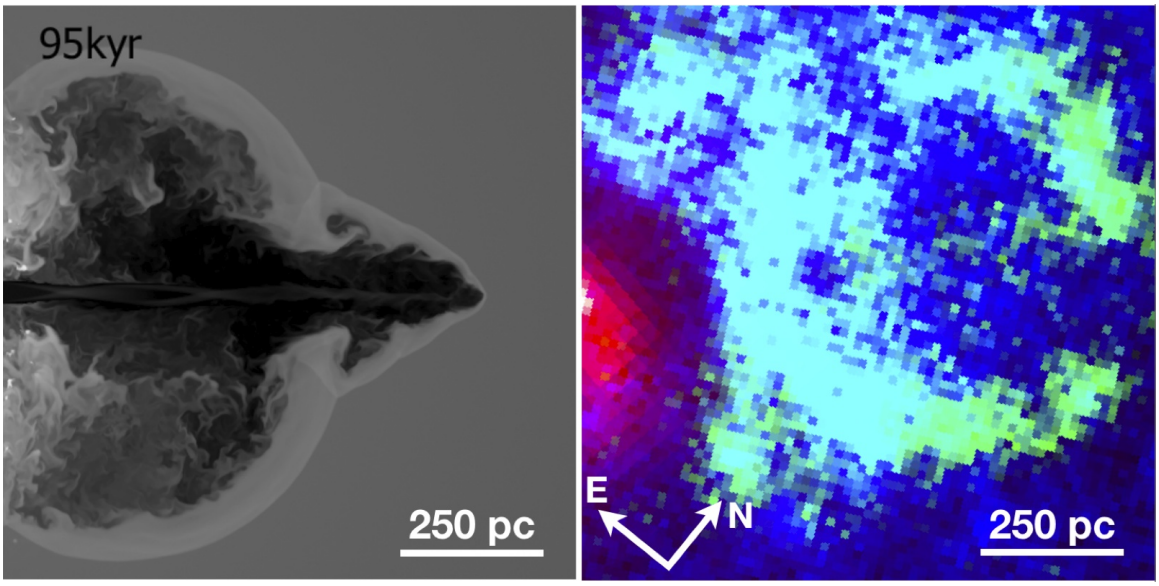

Figure 2.9 *Left:* Last panel of figure 2 from Sutherland & Bicknell (2007), reproduced here with permission. These simulations model the interaction of a supersonic jet with an inhomogenous ISM. The figure shows the 95 kyr time-step of the mid-plane density slices of the simulation, with darker colors representing less dense material. The panel is 1 kpc on a side. *Right:* 3-color image of the bubble feature, as in the right panel of figure 2.7, rotated and zoomed for comparison with the simulation. The western nucleus is centered on the left side of the panel and the opening in the bubble is centered on the right side of the panel. This panel is also 1 kpc on a side.

The evolution of the interaction goes through several stages, including the development of a shocked bubble as the jet interacts with the ISM followed by a breakthrough of the jet through the outer boundary of the bubble. The simulation mid-plane density slices post-breakout (their figure 2, and reproduced here, in figure 2.9) resemble the Arp 220 bubble. However, because this is a generic jet/ISM simulation, this is an idealized comparison; in particular, the ISM of Arp 220 is likely to be denser than that assumed here. Nonetheless, the morphological similarities suggest the possible presence of an AGN and its associated outflow.

The proximity of the nuclei to each other (360 pc) suggests that they should be subject to strong gravitational interactions, but clear observational evidence of an AGN has been sparse. Previous X-ray studies (Rieke 1988; Dermer et al. 1997; Iwasawa 1999; Iwasawa et al. 2001; Clements et al. 2002) ruled out a bright hard X-ray source in the nucleus, which indicates that any AGN must be highly obscured, with a lower limit on the nuclear column density of 10^{25} cm^{-2}. However, evidence for at least one highly obscured AGN in Arp 220 has been mounting in recent years. A maser (Aalto et al. 2009) and a rotating massive molecular disk (Downes & Eckart 2007) have been found, and Contini (2013) find evidence of an AGN in their modeling of the nuclear optical and infrared spectra. Paggi et al. (2013) find strong Fe-Kα line emission in the vicinity of the two nuclei, concentrated most strongly on the western nucleus. From their broadband X-ray data, they estimate lower limits on the AGN bolometric luminosities of 5.2×10^{43} erg s^{-1} (western nucleus) and 2×10^{42} erg s^{-1} (eastern nucleus). New ALMA observations (Wilson et al. 2014) show a luminosity surface density in excess of 10^{14} L$_\odot$ kpc^{-2} at the western nucleus, sufficiently bright to require the presence of a hot starburst, a Compton thick AGN, or both.

As shown in section 2.3.5, the kinetic energy input needed to form the bubble is dE/dt=5.6×10^{41} erg s^{-1} (upper limit, ionized+neutral medium). Taking this as a ratio with respect to the bolometric luminosity of the suspected AGN in the western nucleus gives an energy deposition rate of dE/dt / L_{AGN} = 1.1%, which is an order of magnitude higher than other observed (Rupke & Veilleux 2013b) or modeled AGN energy feedback

rates (Hopkins & Elvis 2010). However, these models are dependent on the fraction of gas in the hot ISM and are uncertain enough to encompass our observed value.

The evidence for an obscured AGN driving the bubble is favorable but not absolute. The morphological similarities to models and the energetics lend support to the theory that this bubble is formed by the interaction of a jet or outflow from an AGN with the galaxy's ISM. This is further supported by the large-scale X-ray structure of the galaxy, which is remarkably well aligned with not just the bubble feature, but also the gap in the side of the bubble away from the nuclei (figure 2.7). However, the western nucleus (the most likely AGN host) has a gas accretion disk that is misaligned with the supposed direction of the jet and bubble. This is not definitive evidence against an AGN outflow, because the observed gas disk has a scale of 100 pc and any inner accretion disk may have a different orientation. Additionally, the outflow velocities in this system are on the low end for typical AGN (Rupke et al. 2005a; Tremonti et al. 2007), but may be consistent with velocities from low-luminosity AGN (Christopoulou et al. 1997; Kewley et al. 2006b; Hicks et al. 2013). We view an AGN jet or outflow as a plausible hypothesis for this bubble's origin.

Collimated outflow from a nuclear starburst

The prevailing explanation for the large-scale superwind structure as seen in X-rays is a massive starburst concentrated near the nuclei (Heckman et al. 1996). Smith et al. (1998) used VLBI continuum imaging to resolve a strong, compact OH maser near the western nucleus into a number of radio supernovae within a 75 $\times$ 150 pc region. Using the lifetime of these objects, they estimate a nuclear star formation rate of 50–800 $M_\odot$ yr^{-1}. Such high levels of star formation in the confines of the nuclear gas disk could potentially drive a starburst wind. If the starburst wind is able to break through the gas disk, the dense gas in the disk will further direct the outflow along the maximum pressure gradient.

In section 2.3.5, we showed that the kinetic energy input needed to form the bubble is dE/dt=5.6×10^{41} erg s^{-1} (upper limit, ionized+neutral medium). If we assume a SFR of 240 $M_\odot$ yr^{-1} (equal to the global SFR and well within the nuclear SFR range), we

can compare the energy in the wind to the mechanical luminosity in the nuclear starburst. Following Rupke & Veilleux (2013b), we calculate the mechanical luminosity in a continuous starburst using Starburst99 models from Leitherer et al. (1999). We apply a correction for a Salpeter IMF, with a lower mass cut at 0.1 $M_{\odot}$. Thus, the energy deposition rate is dE/dt / dE/dt_{SB99} = 0.8% (upper limit). This is in line with that observed in other starburst-dominated ULIRGs (3%–13%, Rupke & Veilleux 2013b). It is thus also possible that the bubble feature is driven by the strong nuclear starburst.

2.4.2 Off-nuclear origins

The bubble may originate from a source at its center rather than from the nucleus. It could be the product of a massive star cluster, or of a microquasar or ULX object.

Massive star cluster

Structures morphologically similar to the Arp 220 bubble feature, known as superbubbles, are believed to be formed by supernovae winds from a massive star cluster pushing out into the surrounding ISM (Cash et al. 1980). The Arp 220 bubble feature demonstrates some evidence consistent with a classical superbubble, but lacks evidence of a sufficiently massive star cluster driving the outflow.

The Arp 220 bubble shows evidence of shock excitation, which is consistent with a supernovae-driven outflow from a massive young cluster. Such outflows shock as they encounter the surrounding ISM and produce an increasing ratio of [NII] to Hα emission at a fixed value of log([OIII]/Hβ) (Baldwin et al. 1981; Kewley et al. 2001, 2006b). The value of log([OIII]/Hβ) is fairly constant across the center of the galaxy at 0.22±0.07 (see section 2.3.2, 0.05±0.11 for the galaxy as a whole). The value of log([NII]/Hα) at the maximum starburst line, or the value at which shock heating is thought to begin to dominate (Kewley et al. 2001), is -0.16±0.04 for this value of log([OIII]/Hβ) (though there are metallicity effects; see, e.g., Dopita et al. 2000; Denicoló et al. 2002; Kewley &

Dopita 2002; Kewley et al. 2006b). Though we cannot separate the [NII] and Hα emission to calculate a ratio with our data, Arribas et al. (2001) show optical IFU spectroscopy data taken with the INTEGRAL instrument on the William Herschel telescope. Their data are lower spatial resolution (fiber diameter$\sim$0.9", R$\sim$2000) and they identify three gas components via spectral line profile decomposition. Spatially, our bubble feature is associated with their component B. They find an average value of log([NII]/Hα) of 0.48$\pm$0.17 for this component. This is consistent with shocked gas in a shell surrounding a massive star cluster that is driving the outflow.

Although our feature resembles typical massive star cluster superbubbles, no massive star clusters are visible in the center of the bubble (figure 2.7). Examination of both the optical continuum image (WFC3-UVIS F621M) and the H-band image (NICMOS F160W) reveals that the flux interior to the ring feature is high enough that a 10^6 $M_\odot$ cluster would be hidden by the background. To determine this limit, we measured the flux of other 10^6 $M_\odot$ clusters outside the bubble as identified by Wilson et al. (2006, , clusters 2, 3, 4, 5, 11, and 12). The mean flux for a 10^6 $M_\odot$ cluster is 3.52$\pm$1.50 $\times 10^{-18}$ ergs cm^{-2} s^{-1} Å^{-1} for WFC3 F621M and 1.77$\pm$0.86 $\times 10^{-18}$ ergs cm^{-2} s^{-1} Å^{-1} for NICMOS F160W, using an aperture of radius 0.17".

Analysis of the energetics provides additional evidence against an outflow driven by a massive young cluster at the bubble center. The mechanical luminosity produced by a 10^6 $M_\odot$ cluster ($\sim 10^{40}$ erg s^{-1} Leitherer et al. 1999) is a factor of $\sim$100 below the energy injection rate ($\sim 10^{42}$ erg s^{-1}) we derived for the bubble. Thus, while we cannot rule out the existence of an undiscovered cluster smaller than 10^6 $M_\odot$, it is unlikely that it is the origin of the bubble feature.

ULX bubble

Ultraluminous X-ray sources (ULX) are compact X-ray sources whose luminosities exceed the Eddington luminosity of an isotropically-emitting stellar-mass object. By definition, they are located away from the nucleus of their host galaxy. The central excitation source

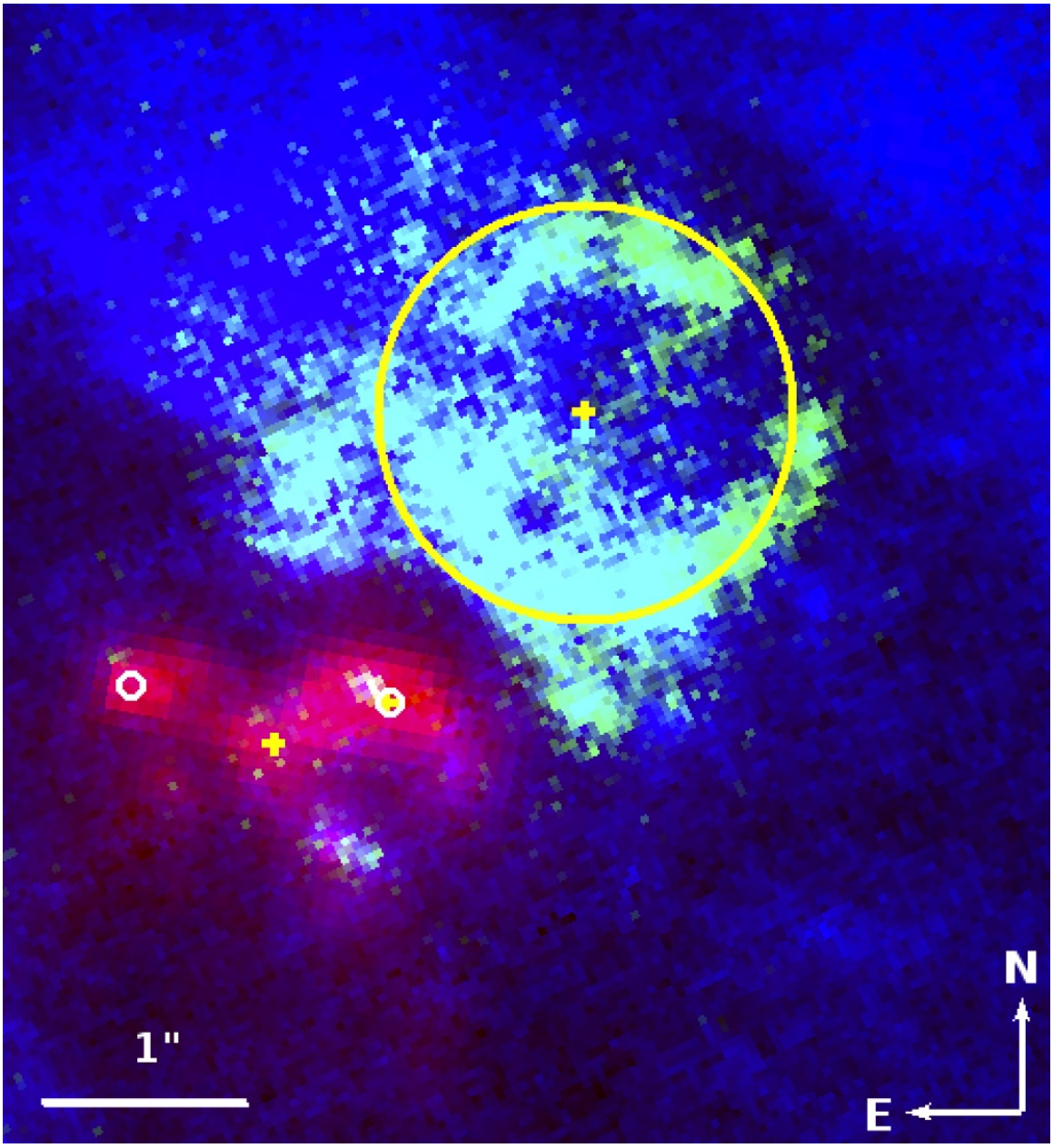

Figure 2.10 3-color image of the central bubble. Background is the same as figure 2.7, right panel. Chandra-identified X-ray sources, from Clements et al. (2002), are marked as yellow crosses, and the two NIR nuclei (Scoville et al. 1998, see section 2.2.3) are marked as white circles. From east to west, the three sources shown are their X-4, X-1 (nuclear), and X-3 (X-2 is out of the field of view). The X-ray source coordinates have been shifted so as to align their X-1 nuclear source with the western NIR nucleus; thus the western nucleus marker is obscured. X-1 and X-4 are both unresolved hard X-ray peaks, while X-3 is the peak of extended soft X-ray emission (extent of 2", shown as the yellow circle).

is still unknown, though their observed variability has been used to hypothesize these as accreting stellar- or intermediate-mass black holes (Colbert & Mushotzky 1999; Kubota et al. 2001). They can exhibit either soft or hard X-ray spectra, and an individual ULX can transition between the two spectral modes (Kubota et al. 2001), presumably due to variability in accretion onto the central source. Many of these objects in the local universe (within 10 Mpc) are associated with large ionized nebulae up to several hundred pc in diameter (Pakull & Mirioni 2002; Cseh et al. 2012; Dopita et al. 2012). These nebulae often show bright Hα bubbles, with the X-ray source either within the bubble or on one edge. Optically, they are generally associated with strong narrow-line He II λ4686Å emission. This high-ionization line is not readily created by normal O-stars, though broad He II lines are observed in Wolf-Rayet stars.

The bubble feature in Arp 220 resembles these ULX bubbles. Its physical extent, 600 pc in diameter, is roughly the same size as the known ULX bubbles. It's also coincident with a bright ($L_{0.3-10.0keV} \sim 10^{39}$ ergs s^{-1}) soft X-ray peak observed by Chandra (Clements et al. 2002, their X-3) (figure 2.10). However, while the X-ray sources associated with the local ULX bubbles are generally compact, Arp 220-X-3 appears to be extended, or embedded in the same extended emission that surrounds the nuclei. Clements et al. (2002) report an extent of 2", shown as the yellow circle in figure 2.10. No data exist on possible variability of this source, or of narrow-line He II emission. Finally, given the alignment of the bubble feature with the large-scale X-ray outflow, it is unlikely that the bubble feature has an origin unrelated to this structure. The large-scale outflow is bipolar and thus likely nuclear in origin. Further study is needed to explore whether this X-ray source is indeed a ULX with an affiliated nebula, or whether the X-ray emission is from hot gas filling the bubble created via one of the mechanisms described above.

2.4.3 Bubble origins, summarized

We have explored four possibilities for the origin of the bubble: an outflow from an obscured AGN, an outflow from high levels of star formation within the nuclear gas disk, a traditional

superbubble surrounding an undiscovered star cluster at the bubble's center, or a ULX bubble.

Given the alignment of the nuclei, bubble feature, and large-scale (biconal) outflow structure, as well as energetics arguments, it is less likely that the feature is caused by an off-nuclear source unrelated to the outflow. While a chance alignment of a ULX superbubble is possible, and warrants further study, it is more likely that an outflow or jet from the nuclear region is driving both the bubble and the outflow.

Out of the two nuclear origin scenarios, we cannot distinguish between an AGN jet or outflow or a starburst outflow. The low luminosity of the suspected AGN in the western nucleus ($\sim 10^{43}$ erg s^{-1}) and the high levels of star formation within the inner nuclear gas disks around both nuclei would each provide a similar rate of energy injection, either of which would be sufficient to drive the bubble feature. It is also possible that both mechanisms are contributing to the outflow driving the bubble.

2.5 CONCLUSIONS

We have resolved the near-nuclear Hα+[NII] emission peak into a bubble feature using HST/WFC3 narrowband photometry. Our new multi-wavelength imaging maps connect this feature to both the nuclear molecular gas disk and large-scale outflows. NIR IFS data show an increase in velocity dispersion at the base of the bubble, while the optical IFS data show that the emission in this region is dominated by shock excitation. This strongly indicates that the bubble is formed by an interaction of a jet or outflow, originating in or near the nucleus, with the surrounding ISM. This outflow shocks as it propagates into the surrounding galaxy and is connected spatially with the large-scale outflow that extends for multiple kpc from the galaxy. We discuss four possibilities of the origin of the bubble and find it most plausible that the bubble originates within the inner $\sim$100 pc around the nuclei. Either an obscured AGN or the observed high level of nuclear star formation could power the observed feature. Further work is needed to differentiate between these two possibilities.

Acknowledgements

Some of the data presented in this paper were obtained from the Mikulski Archive for Space Telescopes (MAST). STScI is operated by the Association of Universities for Research in Astronomy, Inc., under NASA contract NAS5-26555. Support for MAST for non-HST data is provided by the NASA Office of Space Science via grant NNX13AC07G and by other grants and contracts. KEL would also like to acknowledge the SWOOP writing retreat and its participants for useful feedback.

Appendix

Narrowband imaging of [SII]$\lambda\lambda$ 6717, 6731Å, in conjunction with similar imaging of Hα, has been used previously on dwarf galaxies (Calzetti et al. 2004) to separate photoionized from non-photoionized gas, and hence to evaluate photoionized gas oxygen abundances and non-photoionized gas distributions. One of the primary motivations for obtaining the Arp 220 HST dataset presented in this paper was to apply this same technique on a late-stage merger. Unfortunately, the [SII] emission line flux could not be recovered from the F680N filter, due to both complicating factors specific to the combination of the redshift of Arp 220 and this filter, and to the shallowness of the image. In this Appendix, we describe the reduction process for this filter and suggest ways to improve the process.

The F680N filter, which contains the [SII] lines, is also contaminated by some of the Hα+[NII] line complex, which falls on the blue cutoff of the F680N bandpass (figure 2.2). Because the bandpass cutoff falls in the middle of the intruding line complex, we cannot simply subtract the flux-calibrated Hα+[NII] image from the [SII] image. Instead, we must estimate the percentage of the contaminating lines that fall in the bandpass. We convolved the SDSS spectrum with the theoretical throughputs of the F665N and the F680N filters obtained from the `synphot` PyRAF[2] package to calculate the contribution of the flux of

[2]STSDAS and PyRAF are products of the Space Telescope Science Institute, which is operated by AURA for NASA.

these lines. Roughly half the flux in the Hα+[NII] line complex in the SDSS spectrum falls in the F680N bandpass, though the exact contribution depends on the width and velocity of the lines, metallicity, and gas excitation mechanism. This will likely vary across the face of the galaxy, and introduces additional uncertainties.

Changes in the line of sight velocity may shift the Hα+[NII] lines in or out of the F680N bandpass, altering the scaling factor used to remove the flux contributed by these lines. This error was estimated by red and blue shifting the SDSS spectrum by 500 km s^{-1} along the line of sight. At the velocity extremes, the flux contribution from the Hα+[NII] lines complex ranges from 35% to 80% of the flux in these lines. The additional error in flux is included in the 1σ errors on the [SII] image in table 4.1.

However, subtracting 50% of the Hα+[NII] flux from the continuum-subtracted [SII] image produced oversubtracted images with negative flux values near the center of the galaxy, clear artifacts of the Hα+[NII] subtraction. This is likely due to high extinction in the central regions. We explored several avenues for improving continuum subtraction in this filter, all of which were ultimately unsuccessful at producing robust detections of [SII]. This is likely due to the intrinsic faintness of the [SII] lines, which are only 10% of the flux in Hα+[NII] on average, and the short exposure time in the F680N filter.

To make use of the [SII] data, we would require a longer exposure time in the F680N filter to allow us to probe the fainter average [SII] emission. Alternatively, separate high spatial resolution map of both [NII] and Hα flux and velocity structure would allow us to more robustly correct the [SII] image for the [NII] contamination, and hence recover more [SII] flux. Without either of these, the current [SII] data are inadequate for our purposes. Future projects that attempt this type of analysis should be especially careful to obtain deep images of the fainter emission lines.

References

Aalto, S., Wilner, D., Spaans, M., Wiedner, M. C., Sakamoto, K., Black, J. H., & Caldas, M. 2009, A&A, 493, 481

Arp, H. 1966, ApJS, 14, 1

Arribas, S., Colina, L., & Clements, D. 2001, ApJ, 560, 160

Avila, R. J., Hack, W. J., & STScI AstroDrizzle Team. 2012, in American Astronomical Society Meeting Abstracts, Vol. 220, American Astronomical Society Meeting Abstracts #220, #135.13

Baan, W. A. & Haschick, A. D. 1995, ApJ, 454, 745

Baldwin, J. A., Phillips, M. M., & Terlevich, R. 1981, PASP, 93, 5

Barnes, J. E. & Hernquist, L. 1996, ApJ, 471, 115

Calzetti, D., Harris, J., Gallagher, III, J. S., Smith, D. A., Conselice, C. J., Homeier, N., & Kewley, L. 2004, AJ, 127, 1405

Cash, W., Charles, P., Bowyer, S., Walter, F., Garmire, G., & Riegler, G. 1980, ApJ, 238, L71

Cecil, G., Bland-Hawthorn, J., Veilleux, S., & Filippenko, A. V. 2001, ApJ, 555, 338

Christopoulou, P. E., Holloway, A. J., Steffen, W., Mundell, C. G., Thean, A. H. C., Goudis, C. D., Meaburn, J., & Pedlar, A. 1997, MNRAS, 284, 385

Clements, D. L., McDowell, J. C., Shaked, S., Baker, A. C., Borne, K., Colina, L., Lamb, S. A., & Mundell, C. 2002, ApJ, 581, 974

Colbert, E. J. M. & Mushotzky, R. F. 1999, ApJ, 519, 89

Colina, L., Arribas, S., & Clements, D. 2004, ApJ, 602, 181

Contini, M. 2013, MNRAS, 429, 242

Cresci, G., Mannucci, F., Della Valle, M., & Maiolino, R. 2007, A&A, 462, 927

Cseh, D., Corbel, S., Kaaret, P., Lang, C., Grisé, F., Paragi, Z., Tzioumis, A., Tudose, V., & Feng, H. 2012, ApJ, 749, 17

de Vaucouleurs, G., de Vaucouleurs, A., Corwin, Jr., H. G., Buta, R. J., Paturel, G., & Fouqué, P. 1991, Third Reference Catalogue of Bright Galaxies. Volume I: Explanations and references. Volume II: Data for galaxies between 0^h and 12^h. Volume III: Data for galaxies between 12^h and 24^h. (Springer)

Denicoló, G., Terlevich, R., & Terlevich, E. 2002, MNRAS, 330, 69

Dermer, C. D., Bland-Hawthorn, J., Chiang, J., & McNaron-Brown, K. 1997, ApJ, 484, L121

Di Matteo, T., Springel, V., & Hernquist, L. 2005, Nature, 433, 604

Dopita, M. A., Kewley, L. J., Heisler, C. A., & Sutherland, R. S. 2000, ApJ, 542, 224

Dopita, M. A., Payne, J. L., Filipović, M. D., & Pannuti, T. G. 2012, MNRAS, 427, 956

Downes, D. & Eckart, A. 2007, A&A, 468, L57

Downes, D. & Solomon, P. M. 1998, ApJ, 507, 615

Eisenhauer, F., Abuter, R., Bickert, K., Biancat-Marchet, F., Bonnet, H., Brynnel, J., Conzelmann, R. D., Delabre, B., Donaldson, R., Farinato, J., Fedrigo, E., Genzel, R., Hubin, N. N., Iserlohe, C., Kasper, M. E., Kissler-Patig, M., Monnet, G. J., Roehrle,

C., Schreiber, J., Stroebele, S., Tecza, M., Thatte, N. A., & Weisz, H. 2003, in Society of Photo-Optical Instrumentation Engineers (SPIE) Conference Series, Vol. 4841, Instrument Design and Performance for Optical/Infrared Ground-based Telescopes, ed. M. Iye & A. F. M. Moorwood, 1548–1561

Emonts, B. H. C., Piqueras-López, J., Colina, L., Arribas, S., Villar-Martín, M., Pereira-Santaella, M., Garcia-Burillo, S., & Alonso-Herrero, A. 2014, A&A, 572, A40

Engel, H., Davies, R. I., Genzel, R., Tacconi, L. J., Sturm, E., & Downes, D. 2011, ApJ, 729, 58

Farrah, D., Afonso, J., Efstathiou, A., Rowan-Robinson, M., Fox, M., & Clements, D. 2003, MNRAS, 343, 585

Forbes, D. A., Polehampton, E., Stevens, I. R., Brodie, J. P., & Ward, M. J. 2000, MNRAS, 312, 689

Heckman, T. M. 2003, in Revista Mexicana de Astronomia y Astrofisica Conference Series, Vol. 17, Revista Mexicana de Astronomia y Astrofisica Conference Series, ed. V. Avila-Reese, C. Firmani, C. S. Frenk, & C. Allen, 47–55

Heckman, T. M., Armus, L., & Miley, G. K. 1987, AJ, 93, 276

—. 1990, ApJS, 74, 833

Heckman, T. M., Dahlem, M., Eales, S. A., Fabbiano, G., & Weaver, K. 1996, ApJ, 457, 616

Heckman, T. M., Lehnert, M. D., Strickland, D. K., & Armus, L. 2000, ApJS, 129, 493

Hibbard, J. E., Vacca, W. D., & Yun, M. S. 2000, AJ, 119, 1130

Hicks, E. K. S., Davies, R. I., Maciejewski, W., Emsellem, E., Malkan, M. A., Dumas, G., Müller-Sánchez, F., & Rivers, A. 2013, ApJ, 768, 107

Hong, S., Calzetti, D., & Dickinson, M. 2014, PASP, 126, 79

Hopkins, P. F. & Elvis, M. 2010, MNRAS, 401, 7

Hopkins, P. F. & Hernquist, L. 2006, ApJS, 166, 1

Hopkins, P. F., Hernquist, L., Cox, T. J., Di Matteo, T., Martini, P., Robertson, B., & Springel, V. 2005, ApJ, 630, 705

Iwasawa, K. 1999, MNRAS, 302, 96

Iwasawa, K., Matt, G., Guainazzi, M., & Fabian, A. C. 2001, MNRAS, 326, 894

Joseph, R. D. & Wright, G. S. 1985, MNRAS, 214, 87

Kauffmann, G., Heckman, T. M., Tremonti, C., Brinchmann, J., Charlot, S., White, S. D. M., Ridgway, S. E., Brinkmann, J., Fukugita, M., Hall, P. B., Ivezić, Ž., Richards, G. T., & Schneider, D. P. 2003, MNRAS, 346, 1055

Kenney, J. D. P. & Yale, E. E. 2002, ApJ, 567, 865

Kewley, L. J. & Dopita, M. A. 2002, ApJS, 142, 35

Kewley, L. J., Dopita, M. A., Sutherland, R. S., Heisler, C. A., & Trevena, J. 2001, ApJ, 556, 121

Kewley, L. J., Geller, M. J., & Barton, E. J. 2006a, AJ, 131, 2004

Kewley, L. J., Groves, B., Kauffmann, G., & Heckman, T. 2006b, MNRAS, 372, 961

Kubota, A., Mizuno, T., Makishima, K., Fukazawa, Y., Kotoku, J., Ohnishi, T., & Tashiro, M. 2001, ApJ, 547, L119

Leitherer, C., Schaerer, D., Goldader, J. D., González Delgado, R. M., Robert, C., Kune, D. F., de Mello, D. F., Devost, D., & Heckman, T. M. 1999, ApJS, 123, 3

Lockhart, K. E., Kewley, L. J., Lu, J. R., Allen, M. G., Rupke, D., Calzetti, D., Davies, R. I., Dopita, M. A., Engel, H., Heckman, T. M., Leitherer, C., & Sanders, D. B. 2015, ApJ, 810, 149

Martin, C. L. 2005, ApJ, 621, 227

—. 2006, ApJ, 647, 222

McDowell, J. C., Clements, D. L., Lamb, S. A., Shaked, S., Hearn, N. C., Colina, L., Mundell, C., Borne, K., Baker, A. C., & Arribas, S. 2003, ApJ, 591, 154

Mihos, J. C. & Hernquist, L. 1996, ApJ, 464, 641

Mundell, C. G., Ferruit, P., & Pedlar, A. 2001, ApJ, 560, 168

Oey, M. S., Parker, J. S., Mikles, V. J., & Zhang, X. 2003, AJ, 126, 2317

Osterbrock, D. E. 1989, Astrophysics of gaseous nebulae and active galactic nuclei (University Science Books)

Paggi, A., Fabbiano, G., Risaliti, G., Wang, J., & Elvis, M. 2013, ArXiv e-prints

Pakull, M. W. & Mirioni, L. 2002, ArXiv Astrophysics e-prints

Rich, J. A., Dopita, M. A., Kewley, L. J., & Rupke, D. S. N. 2010, ApJ, 721, 505

Rieke, G. H. 1988, ApJ, 331, L5

Rupke, D. S., Veilleux, S., & Sanders, D. B. 2002, ApJ, 570, 588

—. 2005a, ApJ, 632, 751

—. 2005b, ApJS, 160, 87

—. 2005c, ApJS, 160, 115

Rupke, D. S. N. & Veilleux, S. 2011, ApJ, 729, L27

—. 2013a, ApJ, 775, L15

—. 2013b, ApJ, 768, 75

Sakamoto, K., Aalto, S., Combes, F., Evans, A., & Peck, A. 2014, ApJ, 797, 90

Sakamoto, K., Scoville, N. Z., Yun, M. S., Crosas, M., Genzel, R., & Tacconi, L. J. 1999, ApJ, 514, 68

Sanders, D. B., Soifer, B. T., Elias, J. H., Madore, B. F., Matthews, K., Neugebauer, G., & Scoville, N. Z. 1988, ApJ, 325, 74

Scoville, N., Sheth, K., Walter, F., Manohar, S., Zschaechner, L., Yun, M., Koda, J., Sanders, D., Murchikova, L., Thompson, T., Robertson, B., Genzel, R., Hernquist, L., Tacconi, L., Brown, R., Narayanan, D., Hayward, C. C., Barnes, J., Kartaltepe, J., Davies, R., van der Werf, P., & Fomalont, E. 2014, ArXiv e-prints

Scoville, N. Z., Evans, A. S., Dinshaw, N., Thompson, R., Rieke, M., Schneider, G., Low, F. J., Hines, D., Stobie, B., Becklin, E., & Epps, H. 1998, ApJ, 492, L107

Scoville, N. Z., Yun, M. S., & Bryant, P. M. 1997, ApJ, 484, 702

Smith, H. E., Lonsdale, C. J., Lonsdale, C. J., & Diamond, P. J. 1998, ApJ, 493, L17

Soifer, B. T., Sanders, D. B., Madore, B. F., Neugebauer, G., Danielson, G. E., Elias, J. H., Lonsdale, C. J., & Rice, W. L. 1987, ApJ, 320, 238

Surace, J. A., Sanders, D. B., & Evans, A. S. 2000, ApJ, 529, 170

Sutherland, R. S. & Bicknell, G. V. 2007, ApJS, 173, 37

Sutherland, R. S. & Dopita, M. A. 1993, ApJS, 88, 253

Tremonti, C. A., Moustakas, J., & Diamond-Stanic, A. M. 2007, ApJ, 663, L77

van Dokkum, P. G. 2001, PASP, 113, 1420

Veilleux, S., Cecil, G., & Bland-Hawthorn, J. 2005, ARA&A, 43, 769

Veilleux, S., Cecil, G., Bland-Hawthorn, J., Tully, R. B., Filippenko, A. V., & Sargent, W. L. W. 1994, ApJ, 433, 48

Wilson, C. D., Harris, W. E., Longden, R., & Scoville, N. Z. 2006, ApJ, 641, 763

Wilson, C. D., Rangwala, N., Glenn, J., Maloney, P. R., Spinoglio, L., & Pereira-Santaella, M. 2014, ArXiv e-prints

Chapter 3

A Slowly Precessing Disk in the Nucleus of M31 as the Feeding Mechanism for a Central Starburst

Note: This chapter will be submitted for publication by the end of the summer, with co-authors J. R. Lu, H. V. Peiris, R. M. Rich, A. Bouchez, and A. M. Ghez.

Abstract

We present a kinematic study of the nuclear stellar disk in M31 at infrared wavelengths using high spatial resolution integral field spectroscopy. The spatial resolution achieved, FWHM = $0\farcs12$ (0.45 pc at the distance of M31), has only previously been obtained or bested in spectroscopic studies by space-based long-slit observations. Using adaptive optics-corrected integral field spectroscopy from the facility instrument OSIRIS at the W. M. Keck Observatory, we map the line-of-sight kinematics over the entire old stellar eccentric disk orbiting the supermassive black hole (SMBH) at a distance of $r < 4$ pc. The peak velocity dispersion is 381±55 km s^{-1}, offset by $0\farcs13 \pm 0\farcs033$ from the SMBH, consistent with previous high-resolution long-slit observations. There is a lack of NIR emission at the position of the SMBH and young nuclear cluster, suggesting a spatial separation between the young and old stellar populations within the nucleus. We compare the observed kinematics with dynamical models from Peiris & Tremaine (2003). The best-fit disk orientation to the NIR flux is $[\theta_l,\ \theta_i,\ \theta_a] = [-32.8^\circ\pm3.5^\circ,\ 44.1^\circ\pm1.8^\circ,\ -14.5^\circ\pm14.6^\circ]$, which is tilted with respect to both the larger-scale galactic disk and the best-fit orientation derived from

optical observations. The precession rate of the old disk is 0.0±3.4 km s^{-1} pc^{-1}, lower than the majority of previous observations. This slow precession rate suggests that stellar winds from the disk will collide and shock, driving rapid gas inflows and fueling an episodic central starburst as suggested in Chang et al. (2007).

3.1 INTRODUCTION

Many galaxies harbor not only supermassive black holes (SMBH), but also young stellar populations in the central few parsecs. The origin of these young stars is unusual given that extreme tidal forces near the SMBH will shear typical molecular clouds apart before they can collapse to form stars (e.g., Sanders 1992; Morris 1993). A young or intermediate age stellar population has been detected in nearly all nuclear star clusters found in nearby galaxies (Allen et al. 1990; Rossa et al. 2006; Seth et al. 2006; Paumard et al. 2006), including in the nuclear star cluster of M31 (d=785 pc, $M_\bullet \sim 10^8$ $M_\odot$ McConnachie et al. 2005; Bender et al. 2005). The SMBH in M31 is surrounded by a young (< 200 Myr) nuclear cluster designated P3, which is visible in the ultraviolet (UV), has a total mass of $\sim 10^4$ $M_\odot$, is confined to the central 0.″1 (0.4 pc), and is orbiting in a disk coplanar with the rest of the nuclear star cluster (e.g., Lauer et al. 1998; Bender et al. 2005; Lauer et al. 2012). The abundance of young stars around nearby SMBHs suggests that whatever physical mechanism deposits or forms stars in this region may be important in many galactic nuclei.

One explanation for the existence of young stars near a SMBH is *in situ* star formation in a massive self-gravitating gas disk around the SMBH, such as has been postulated for the Milky Way from kinematic studies of its young stellar population (Levin & Beloborodov 2003; Lu et al. 2009; Yelda et al. 2014). Such a disk would be sufficiently dense to overcome the strong tidal forces and fragment to form stars, as has been suggested in the context of active galactic nuclei (AGN) accretion disks (e.g., Kolykhalov & Syunyaev 1980; Goodman 2003). Unlike the Milky Way, which hosts $\geq 10^4$ $M_\odot$ of cold gas and dust in the inner 5 pc (Genzel et al. 1985), M31 is relatively gas-poor in the central few kpc (Sofue & Yoshida

1993; Nieten et al. 2006) and the origin of the gas that formed the young nuclear star cluster is not yet known.

In M31, there is an eccentric disk of old stars extending a few parsecs from the central SMBH (Tremaine 1995) that has been postulated to both be the source of the molecular gas and the means for ushering that gas into the central parsec where the young stars are observed (Chang et al. 2007). The mass loss from the red giants and asymptotic giant branch stars in this disk is high enough to drive a new *in situ* star formation event every 500 Myr, if there are crossing orbits in the eccentric disk of old stars. The crossing orbits would lead to gas collisions, shocks, and inflows on timescales shorter than typical viscous times. The presence of such crossing orbits depends critically on a low precession speed ($\lesssim$10 km s^{-1} pc^{-1}) for the eccentric disk of old stars.

The structure and kinematics of the eccentric nuclear disk have been studied at multiple wavelengths. Optical high-spatial-resolution observations with the *Hubble Space Telescope* (HST) (Lauer et al. 1993, 1998) reveal the structure of the eccentric disk: a brighter stellar concentration, P1, at apoapse, and a fainter concentration, P2, at periapse. The old stellar disk surrounds the young nuclear cluster, P3, and extends roughly 1″ (4 pc) from the SMBH (Fig. 3.1). The red color of the disk suggests an older stellar population, assumed to be roughly the age of the surrounding bulge, or >4 Gyr (Olsen et al. 2006; Saglia et al. 2010). Current dynamical models (Peiris & Tremaine 2003) suggest the orientation of the eccentric disk is inclined ∼20° to the larger-scale galactic disk. CO observations with the HEterodyne Receiver Array (HERA) on the IRAM 30m telescope show that a dusty 0.7 kpc ring is also misaligned with the larger-scale galactic disk, with a position angle (PA) of −66° versus 37° for the larger disk (Melchior & Combes 2013), which is not aligned with the eccentric nuclear disk. Recent dynamical models of the eccentric nuclear disk also show that it is thick ($h/r \sim 0.4$, Peiris & Tremaine 2003), and that the razor-thin models (Sambhus & Sridhar 2000; Jacobs & Sellwood 2001; Salow & Statler 2001; Sambhus & Sridhar 2002; Salow & Statler 2004) cannot properly fit the observations.

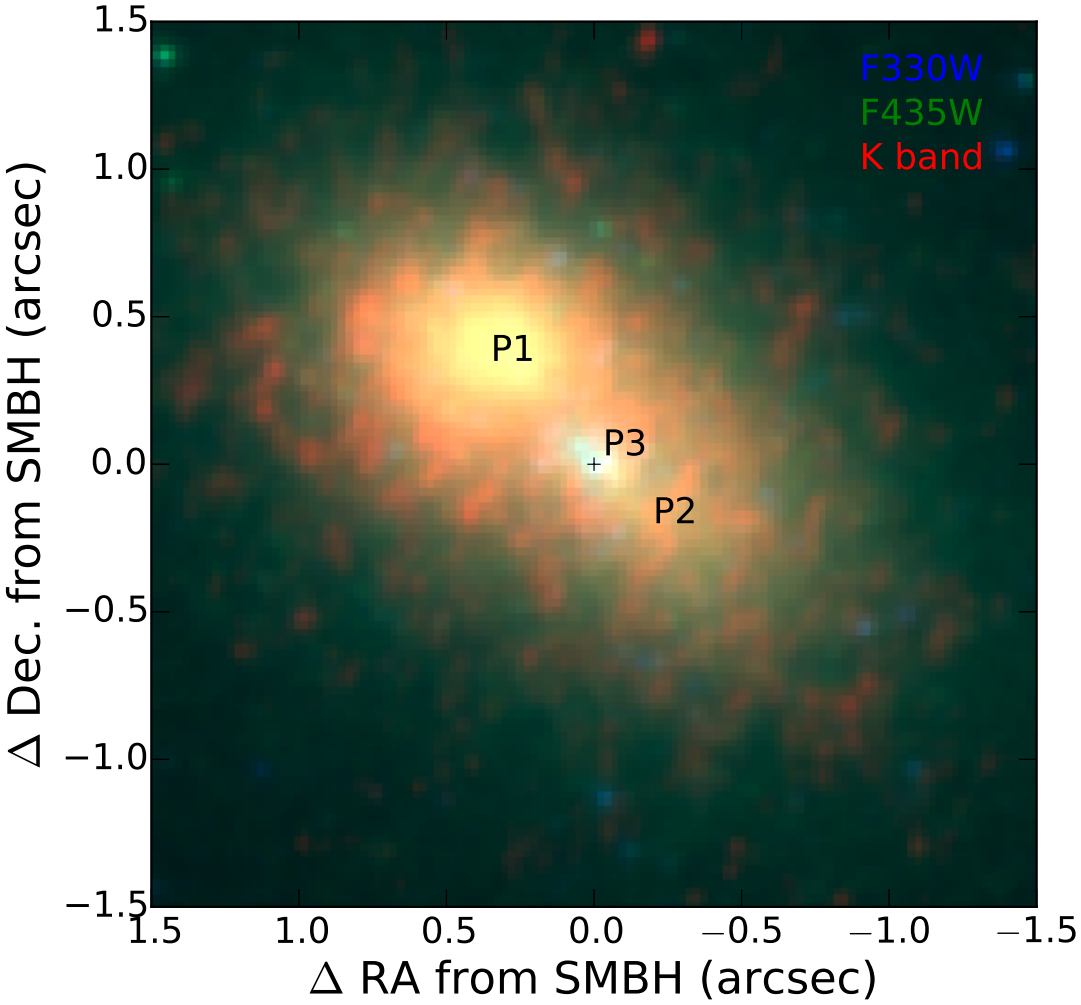

Figure 3.1 Three-color image of the nucleus with components labeled. The eccentric disk is demarcated by P1 at apoapse and P2 at periapse and contains old stars. The young nuclear cluster, P3, is centered on the SMBH and is prominent at blue wavelengths. $1''$ is $\sim$4 pc at M31's distance of 785 pc.

A wide range of conflicting precession values, Ω_P, have been measured for the eccentric disk, from 3 km s^{-1} pc^{-1} to over 30 km s^{-1} pc^{-1} (Sambhus & Sridhar 2000; Bacon et al. 2001; Jacobs & Sellwood 2001; Salow & Statler 2001; Sambhus & Sridhar 2002; Salow & Statler 2004). Thus the origin of the gas that formed P3 remains unresolved. The existence of the eccentric disk also poses another puzzle: realistic models that explain its existence are difficult to compute. Simulations suggest that gas inflows can drive large-scale gas instabilities which can set up long-lived nuclear eccentric disks (Hopkins & Quataert 2010), or that a pair of counter-rotating massive star clusters can decompose into an eccentric disk (Kazandjian & Touma 2013). Either method predicts that the resulting structure will be slowly precessing (Ω_P = 1–5 km s^{-1} pc^{-1}). However, the issue is by no means settled observationally or theoretically.

Complete modeling of the eccentric disk, including a precise measurement of the precession rate, has been limited by the fact that many spectroscopic studies of the eccentric disk have used long-slit spectroscopy, often in combination with imaging (Kormendy & Bender 1999; Statler et al. 1999; Bender et al. 2005). While several of these long-slit studies have been at high spatial resolution ($\lesssim 0\farcs1$), they have been limited by lack of coverage of the field of view. Several integral-field spectroscopy studies have been conducted (Bacon et al. 2001; Menezes et al. 2013), but the limited spatial resolution ($\sim 0\farcs4$) likely contributes to some of the scatter in the precession rate measurements. In addition, all spectroscopic studies of the eccentric disk to date have been conducted in the optical, though the eccentric disk is brighter in the near-infrared (NIR). With the advent of laser guide star adaptive optics (LGS AO) feeding integral−field unit (IFU) spectrographs, high spatial resolution 2D kinematics can now be obtained and used to test precessing eccentric disk models and hypotheses for the formation of the young nuclear star cluster in M31.

We discuss the observations in §3.2, including new ground-based NIR data in §3.2.1, the data reduction and analysis in §3.3, and results from the data in §3.4. The results from the analysis are compared to models in §3.5 and discussed in §3.6. We summarize our conclusions in §3.7.

3.2 OBSERVATIONS

New high-spatial resolution observations of the nucleus of M31 (α = 00 42 44.3, δ = +41 16 09, J2000) were obtained in the infrared with the adaptive optics system at the W. M. Keck Observatory. Archival optical HST imaging was obtained to place the new NIR observations in context. While HST provides high-resolution imaging in the optical, the only means of obtaining high spatial resolution integral field spectroscopy is using ground-based adaptive optics (AO) in the IR. Details of the AO-assisted infrared imaging and integral field spectroscopy are described in §3.2.1. Optical imaging with HST is described in §3.2.2.

3.2.1 Ground-based observations

Infrared observations of the nucleus of M31 were obtained with the LGS AO system on the W. M. Keck II 10 m telescope (van Dam et al. 2006; Wizinowich et al. 2006). The laser was positioned on the nucleus to correct high-order atmospheric aberrations. Low-order aberrations were corrected using two different tip-tilt stars during different observing runs. During good seeing, a close and faint globular cluster was used for tip-tilt correction; it is located 35″ to the southwest from the nucleus with R=16.2 at 00 42 42.203 +41 15 46.01 (J2000). A second globular cluster, NB95, with R=14.9 and located 53″ southeast from the nucleus at 00 42 47.973 +41 15 37.07, was used as the tip-tilt reference when seeing was poor or variable or if clouds were present (Battistini et al. 1993; Galleti et al. 2007). These tip-tilt stars are located in a region of M31 with high surface brightness and a strong gradient in the unresolved galaxy light. Thus, in order to properly background-subtract the tip-tilt wave front sensor, the sky background was measured at a manually-selected sky position such that the light from M31's bulge had comparable intensity to that of the tip-tilt star positions.

Table 3.1 Keck/OSIRIS Data

Night	No. of frames	Position
2008 Oct 21	13	center
2010 Aug 15	18	center
2010 Aug 28[a]	22	edges
2010 Aug 29	23	edges

[a]Night removed from analysis due to poor spatial resolution

Keck/OSIRIS

Spectroscopic measurements of the M31 nucleus were made using OSIRIS (Larkin et al. 2006), an integral field unit spectrograph, on 2008 October 21 (PI: M. Rich), 2010 August 15 (PI: J. Lu), and 2010 August 28–29 (PI: A. Ghez, Table 3.1). The individual OSIRIS data cubes cover $0\farcs8 \times 3\farcs2$ and were oriented at a PA of 56° along the major axis of the eccentric stellar disk. The field was sampled with a pixel scale of $0\farcs05$ pix^{-1} and each spatial pixel (spaxel) provides an independent spectrum across the K-broadband filter (Kbb: $\lambda = 2.18\ \mu\mathrm{m}, \Delta\lambda = 0.4\ \mu\mathrm{m}$) with an average spectral resolution of $R \sim$3600. A total of 76 individual exposures were taken with t_{exp} = 900 s in a 3×1 mosaic pattern. Observations taken the night of 2010 August 28 were subject to poor weather; the spatial resolution of these frames was generally poor (see § 3.3.2) and thus these frames were removed from the analysis, leaving 54 total exposures. Observations on two of the remaining three nights were centered on the field, while the northwest and southeast pointings of the mosaic were observed for one night. Total integration time on the center of the field consists of ∼35 exposures (9 hours) while the edges of the field of view (FOV) were observed in 5–20 exposures (1.25–5 hours; see Fig. 3.2, bottom panel).

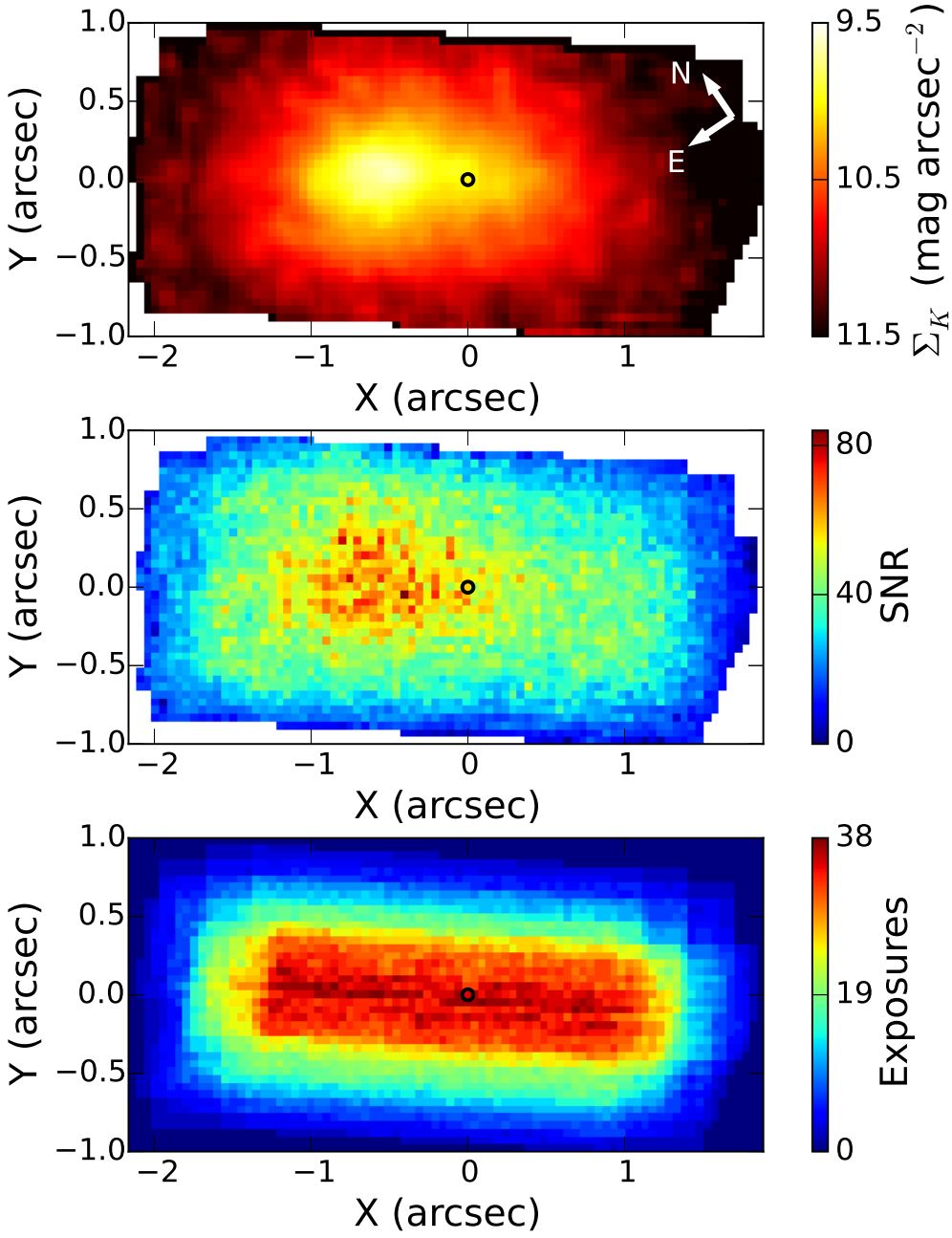

Figure 3.2 Data quality maps of the OSIRIS mosaic, using data from 2008 Oct 21, 2010 Aug 15, and 2010 Aug 29. *Top:* Mosaic of all OSIRIS frames from these three nights, collapsed along the wavelength direction. *Center:* Signal-to-noise ratio map calculated using a line-free portion of the continuum. *Bottom:* Number of exposures combined at each spaxel in the mosaic.

Keck/NIRC2

New supporting NIR imaging of the M31 nucleus was obtained with NIRC2, the facility NIR camera on Keck. On 2005 July 29, a total of 8 images were taken in the K-prime (K')-band filter ($\lambda = 2.12\ \mu\mathrm{m}, \Delta\lambda = 0.35\ \mu\mathrm{m}$) with 30 s exposure times (PI: K. Matthews).

On 2009 September 10, the nucleus was imaged with NIRC2 using the J ($\lambda = 1.25\ \mu\mathrm{m}, \Delta\lambda = 0.16\ \mu\mathrm{m}$) and H ($\lambda = 1.63\ \mu\mathrm{m}, \Delta\lambda = 0.30\ \mu\mathrm{m}$) filters. Exposure times were 120 s and 60 s, respectively. A total of 15 frames were combined for the final J image, and 14 frames were used for the H image (PI: A. Ghez).

The J, H, and K' images described above were all taken using the narrow camera, which provides a pixel scale of $0\farcs01$ pix^{-1}. Wide camera images, with a pixel scale of $0\farcs04$ pix^{-1}, were obtained from the Keck Observatory Archive from observations taken on 2007 October 19 during engineering time with NIRC2 using the K' filter. One exposure was used, with 5 coadds of 1 s integration time each, for a total exposure time of 5 s.

3.2.2 HST

Supporting archival imaging of the nucleus from HST was also used. Optical images of the M31 nucleus were obtained with HST and downloaded from the Hubble Legacy Archive. The nucleus was imaged on 2006 June 15–16 using the Advanced Camera for Surveys (ACS) High Resolution Channel (HRC) with the F330W and F435W filters (PI: T. Lauer, Lauer et al. 2012). Total exposure time with the F330W filter was 8120 s over 12 exposures, while the total exposure time with the F435W filter was 2384 s over 8 exposures.

The nucleus was imaged on 1994 Oct 02 using the Wide Field and Planetary Camera 2 (WFPC2) with the F555W, F814W, and F1042M filters (PI: M. Rich, Rich et al. 1996). Total exposure time for the F555W filter was 1680 s over 6 exposures, for the F814W filter was 1280 s over 5 exposures, and for the F1042M filter was 5000 s over 10 exposures.

3.3 ANALYSIS

3.3.1 OSIRIS data reduction

The OSIRIS spectroscopic data were reduced using the OSIRIS reduction pipeline[1] (Krabbe et al. 2004) to subtract a dark frame, correct bad pixels and cosmic rays, perform the data cube assembly and wavelength calibration, and remove the background sky and telluric OH emission. The pipeline version utilized for the reduction was v3.2. The pipeline includes internal logic to account for the hardware changes that have occurred since the data were taken and uses the modules appropriate for the date of observations.

For each data cube, the telluric absorption spectrum was modeled and removed using a combination of empirical and theoretical telluric absorption spectra. The empirical telluric spectrum was created using two standard stars with different spectral types as described in Hanson et al. (1996). A hot, early-type A0V star was observed (HD 209932). This star has a featureless black body spectrum in the $K-$band, except for a wide Brγ absorption feature at 2.166 μm. A solar-type star was also observed (HD 218633) and divided by a solar spectrum constructed from NSO data by ESO and convolved to match the OSIRIS spectral resolution (Livingston & Wallace 1991; Maiolino et al. 1996) to obtain a telluric spectrum. The solar-type telluric standard was used to replace the region around Brγ, from 2.151 μm to 2.181 μm, in the A0V spectrum. The corrected A0V spectrum was then divided by a 9500 K blackbody to obtain the final empirical telluric absorption spectrum.

However, changing atmospheric conditions throughout each night and a variable spectral resolution across the OSIRIS FOV led to large residuals when correcting for telluric absorption using the empirical telluric spectrum, which was observed at only a single detector location. This was specifically an issue where blue-shifted stellar CO bandheads in the M31 spectra overlap with the large telluric residuals. To better model the changing telluric line depths, we created model telluric spectra with the `molecfit` package (Smette et al. 2015; Kausch et al. 2015), which generates synthetic telluric absorption spectra. Given

[1] github.com/Keck-DataReductionPipelines/OsirisDRP

an atmospheric profile for a given night and observatory location, `molecfit` uses a radiative transfer code to obtain absorption line depths and fits the output directly to the telluric features in a science spectrum. Before using `molecfit`, the OSIRIS M31 science frames were first mosaicked by night and by pointing, roughly corresponding with first and second half-nights, to better capture temporal telluric variations. A subset of 3×3 spaxels was extracted from a region of each mosaic where the stellar absorption lines did not overlap with the telluric lines. The median of these spectra was taken to create a single typical spectrum per half-night, and `molecfit` was run on each of these representative spectra to obtain the telluric absorption line depths. However, these model spectra could not be used directly in the telluric correction, as OSIRIS introduces a shape to the continuum that is not fit well by the `molecfit` modeling. The resulting `molecfit` line depths were combined with the continuum from the empirical telluric spectrum to produce a final telluric absorption spectrum, which was used to telluric-correct the M31 data.

The final mosaic was assembled by calculating shifts between frames using cross-correlations between each OSIRIS frame and the NIRC2 $K-$band image, rebinned to the OSIRIS spatial scale. Frames within a single dithered set (typically 4–9 frames) were first mosaicked together, as the offsets between these frames are given by the input dithers. Each of these mosaics was then cross-correlated with the NIRC2 image to obtain its relative shift. The frames were then combined using a mean clipping method. The final OSIRIS data set consists of one fully combined data cube and three subset cubes, each containing 1/3 of the data, used for determining uncertainties.

3.3.2 Flux errors and data quality

The formal errors output by the pipeline include real spatial and spectral variations caused by removed OH sky lines, telluric absorption, interpixel sensitivity, and cosmic rays. However, the overall error is too large by nearly an order of magnitude relative to empirical error estimates, determined via the standard error on the mean of three subset cubes at each spaxel and spectral channel. As the magnitude of the flux errors impacts the errors on

the kinematic measurements (§3.3.6), the errors need to be properly scaled. To combine the error variation captured by the formal pipeline errors with the more accurate magnitude of the empirical errors, we scale the pipeline errors by the ratio of the median of the two error arrays at every spaxel. We adopt these scaled flux errors for the remainder of the analysis.

The OSIRIS image quality was estimated by first collapsing the cube along the spectral direction. Then the OSIRIS image was compared to the NIRC2 image by convolving the NIRC2 image with an iteratively determined kernel that reduced the difference between the NIRC2 and OSIRIS images. A Gaussian kernel was used to represent the diffraction-limited core. The amplitude was set to 1 and not allowed to vary, while the width of the core Gaussian was allowed to vary. This gives an estimate of the spatial resolution of the OSIRIS images compared to the NIRC2 images. The resulting spatial resolution ranges between 50 and 350 mas FWHM for the individual exposures and the median spatial resolution across all frames is 260 mas. The majority of the lower quality frames are in the southeast pointing of the mosaic, due to worse observing conditions during the nights this pointing was observed. We experimented with removing various combinations of the lowest quality frames, striving to maintain even coverage across the FOV. Ultimately, all frames from 2010 August 28, the night with the worst weather, were removed, resulting in a median spatial resolution of 205 mas amongst the remaining frames and a resolution of 124±6 mas for the full combined mosaic (Fig. 3.3). We proceeded with the analysis using this clipped set.

3.3.3 Bulge subtraction

The old stellar population of the bulge is the dominant source of light at $5\farcs5 < r < 300''$ (Kormendy & Bender 1999, hereafter KB99) and is a source of foreground contamination in observations of the nuclear disk. In addition to being a source of excess surface brightness, the bulge's slow rotation and internal dispersion can distort the kinematic signature of the nuclear disk. Both the surface brightness and the kinematic contribution of the bulge must be removed before extracting the nuclear disk kinematics.

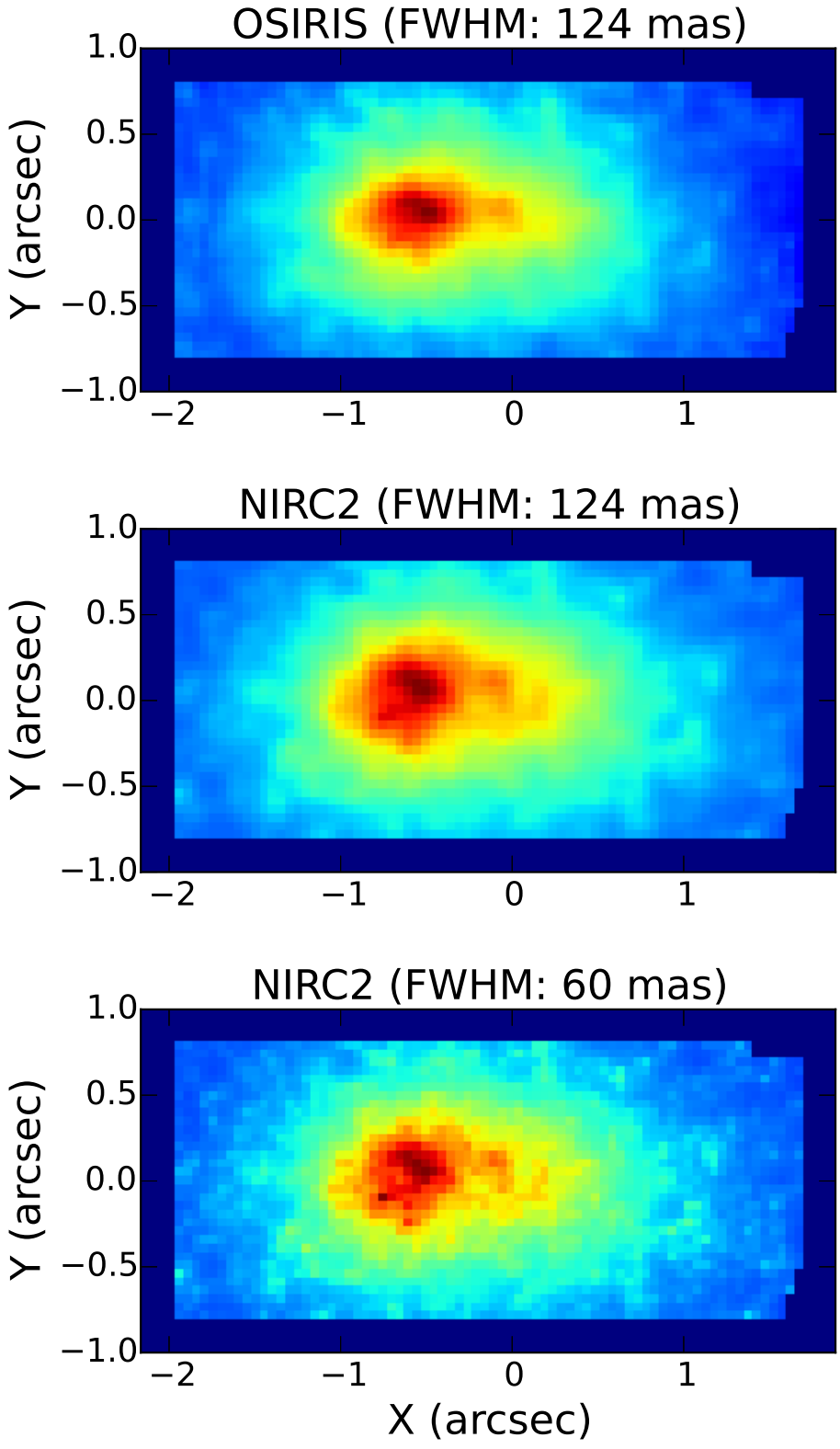

Figure 3.3 The spatial resolution of the combined OSIRIS mosaic was determined by comparing it with a high resolution $K-$band NIRC2 image convolved with a Gaussian. *Top:* OSIRIS data cube, collapsed in the wavelength direction. *Middle:* NIRC2 $K-$band image, convolved to the same spatial resolution as the OSIRIS cube. *Bottom:* Unconvolved NIRC2 image, binned to the same pixel scale as the OSIRIS data.

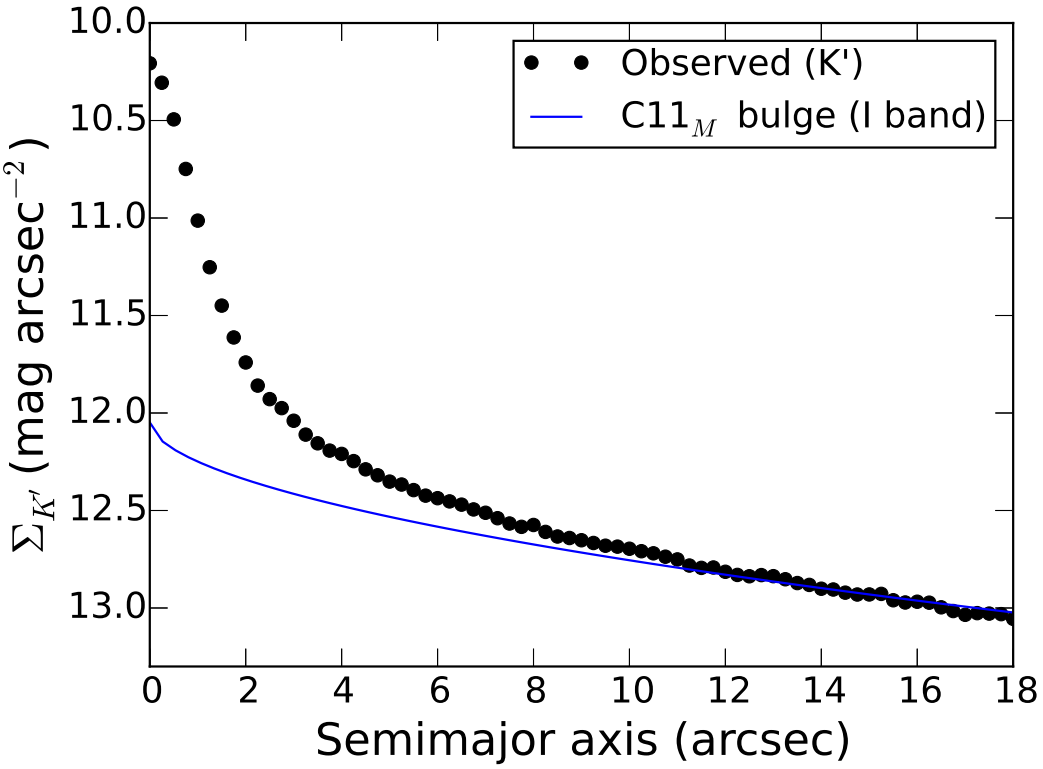

Figure 3.4 Profiles for the bulge surface brightness (Courteau et al. 2011) match measured $K-$band surface brightness profiles well beyond $11''$. The flux-calibrated $K-$band surface brightness profile is measured from the NIRC2 wide camera image and is calculated in elliptical apertures using the ellipticity given by Courteau et al. (2011). The bulge profile is given in Courteau et al. (2011, their model M); an additive offset has been applied to the bulge profile so it matches the flux level in the $K-$band at $15''$, necessary because of the flux difference between the two bandpasses.

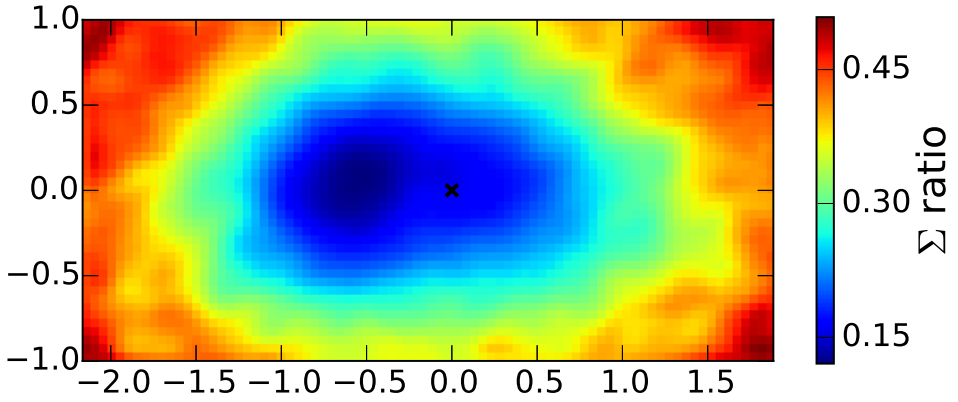

Figure 3.5 Ratio of the bulge luminosity to the total $K-$band luminosity within the nuclear region, derived using the $I-$band Sersic profile (model M) from Courteau et al. (2011) in comparison with the NIRC2 $K-$band image. The SMBH position is marked with the black cross, and the orientation is as in Fig. 3.2.

First, we determined the fraction of bulge light in each spaxel. Previous studies have found that both the optical and the NIR surface brightness profile of the bulge is well-fit by a Sersic profile (KB99, Courteau et al. 2011; Dorman et al. 2013) of index ∼2, half-light radius ∼1 kpc, and half-light surface brightness 17.55–17.85 mag arcsec^{-2} (optical $V-$band, λ = 555Å, and $I-$band, λ = 806Å) or 15.77 mag arcsec^{-2} ($L-$band, λ = 3.6μm). The $I-$band surface brightness profile from Courteau et al. (2011, model M) was adopted and scaled to match the NIRC2 $K-$band wide field image at a radius of 10″, or a distance at which the bulge dominates the surface brightness (Fig. 3.4). The one-dimensional Sersic profile was converted to a two-dimensional profile using the model M bulge ellipticity. We used the bulge PA of 6.6° from Dorman et al. (2013), as they fit the bulge profile with the same data set; the differences with their best fit parameters are negligible. Both the two-dimensional bulge profile and the NIRC2 image were smoothed to match the OSIRIS resolution and the two smoothed images were divided to obtain the ratio of bulge luminosity to total luminosity in the nucleus (Fig. 3.5).

Next, the intrinsic spectrum of the integrated bulge light was estimated using the pPXF package (Cappellari & Emsellem 2004), which fits a linear combination of stellar templates

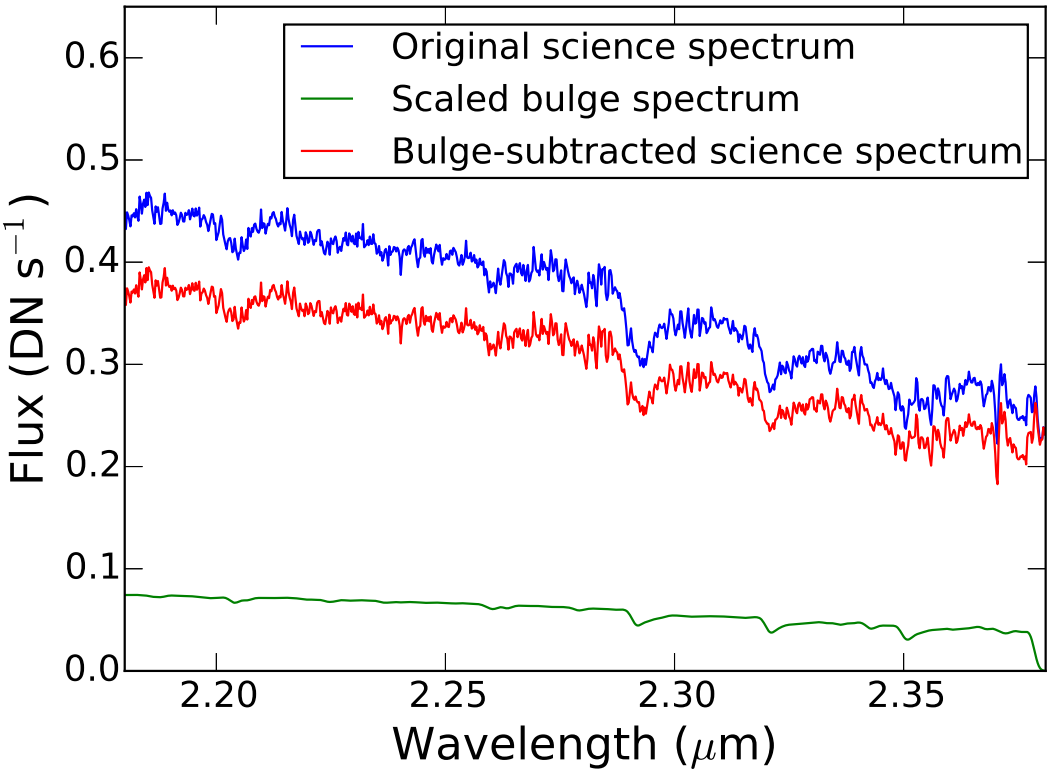

Figure 3.6 Example science spaxel, before and after bulge subtraction. The spaxel is taken from near the center of the cube and is shown before and after bulge subtraction. The bulge spectrum, convolved with the bulge LOSVD and scaled per the ratio given in Fig. 3.5 for the example spaxel, is also shown.

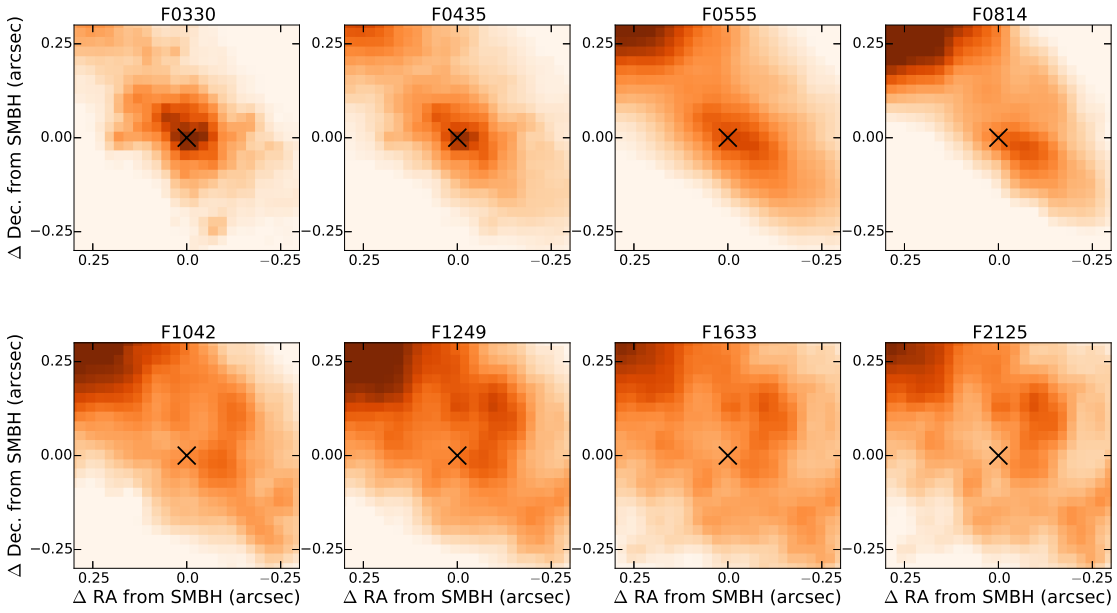

Figure 3.7 Multi-wavelength images show the changing stellar population from 330 nm (F0330) to 2.1 μm (F2125). The position of P3, assumed to be coincident with the SMBH, is marked with the black cross and is accurate to 0.033″ in the F2125 frame. The color scaling has been adjusted for each frame to emphasize the structure around the SMBH. North is up and East is left and the pixel scale is 0.025″ pixel^{-1}.

convolved with a line of sight velocity distribution (LOSVD, see § 3.3.6 for more details). The non-bulge-subtracted data cube was fit with pPXF and the edge of the FOV was assumed to be representative of the bulge. As no spaxels had a majority contribution from the bulge (Fig. 3.5), those spaxels in which the bulge surface brightness ratio is at least 0.42 were selected to be representative of the bulge. This ensures that enough spaxels, roughly 160, were obtained to derive a high-quality bulge template spectrum. The best-fit linearly-combined stellar templates were extracted from each of these bulge spaxels to use as the input stellar spectra and normalize them. The median of all bulge template spectra at each wavelength was taken to obtain a median stellar template for the bulge.

The median bulge spectrum was dominated by two stellar template spectra: a late-K giant and a late-K dwarf. The late-K giant is likely more representative of the actual bulge population, which is estimated to be roughly the age of the galaxy (Saglia et al. 2010).

However, the late-K dwarf star has stronger Na lines than that of the giant. The center of M31 is estimated to have enhanced metallicity compared to Milky Way (Saglia et al. 2010) and thus the inclusion of the dwarf stellar template in the fit may be compensating for this different abundance pattern. Alternatively, varying Na line strengths may represent variation in the initial mass function of the old stellar population (McConnell et al. 2015, and references therein).

Finally, the bulge spectrum was convolved with a Gaussian LOSVD with a fixed velocity of 340 km s^{-1}, at the systemic velocity of the galaxy, and a dispersion of 110 km s^{-1} at all points in the field. No bulge rotation was included since previous work by KB99 found that the bulge is rotating slowly at $2.65(r/1'')$ km s^{-1} and that including this rotation does not appreciably affect the bulge subtraction within the compact nuclear region. The final bulge spectrum was multiplied by the median flux in each spaxel and the appropriate surface brightness ratio to create a bulge cube. This cube was then subtracted from the observed spectral cube. An example spectrum, before and after bulge subtraction, along with the scaled bulge template spectrum is shown in Fig. 3.6.

There are systematic sources of error in the bulge subtraction that we do not fully explore but which should be kept in mind. The edges of the OSIRIS FOV are subject to much more bulge subtraction than the center (Fig. 3.5). Subtracting so much flux ends up amplifying the noisiness of the bulge-subtracted spectrum. This noise is not purely Poissonian, but also includes noise from imperfectly-corrected sky and telluric features, which introduce larger systematic errors into the spectra at the edge of the FOV. In addition, the bulge is typically modeled as a Sersic profile, which is sharply peaked at the origin. However, Bacon et al. (2001) also fit the bulge using a Multi-Gaussian Expansion (MGE), which models the bulge surface brightness as the sum of three Gaussians. Their MGE bulge profile is much shallower in the inner few arcsec, with a difference of a few tenths of a magnitude at the origin from the equivalent Sersic profile. Alternative bulge subtraction methods may subtract more or less flux than does our method, which may impact the kinematics derived from the bulge-subtracted spectra.

Table 3.2 SMBH alignment

Telescope	Instrument	Filter	$N^a_{sources}$	Error ($''$)
HST	ACS	F330W	...	...
HST	ACS	F435W	16	0.0093
HST	WFPC2	F555W	26	0.013
HST	WFPC2	F814W	16	0.018
HST	WFPC2	F1042M	19	0.016
Keck	NIRC2	$J-$band	19	0.015
Keck	NIRC2	$H-$band	18	0.0065
Keck	NIRC2	$K'-$band	18	0.0063

[a]Number of sources used to align the given frame with the next bluer frame

3.3.4 Position of the supermassive black hole

We identified the position of the SMBH in our OSIRIS and NIRC2 data using the position of P3, the very compact ($r \sim 0\farcs06$, Lauer et al. 1998) young nuclear cluster that contains the SMBH (Bender et al. 2005). Unlike the old stellar population, which is bright in the NIR, P3 is NIR-dark and thus effectively invisible in our OSIRIS and NIRC2 data. However, P3 is bright in the UV; we adopted as the SMBH position the location of source 11, or the brightest UV source in the Lauer et al. (2012) analysis of HST/ACS F330W and F435W images. The NIR image cannot be directly aligned to the F330W image because there are no compact sources that are bright in both the blue and NIR filters that can be used to determine the transformation. Instead, we aligned images at successively longer wavelengths using an evolving set of compact, bright sources to fit the translation, scale, and rotation (Table 3.2), aligning adjacent-bandpass frames using only the sources common to both frames (see Appendix 3.8). At least 16 bright compact sources are used for aligning each pair of frames. After alignment, each frame was transformed into the reference frame, F330W. The error on each frame's alignment was taken as the residual error, converted to arcseconds. The total error in alignment from F330W to the NIRC2 $K-$band image is $0\farcs033$, which is smaller than the $0\farcs05$ spaxels in the OSIRIS data. The OSIRIS data cube

was aligned to the NIRC2 $K-$band image by cross-correlating the OSIRIS cube, collapsed in the wavelength direction, with the final registered NIRC2 $K-$band image.

Figure 3.7 shows the region within $0\farcs3$ of P3 in each of the eight wavelength images after alignment. The pixel scaling was adjusted in each frame to match that of the F330W image. The SMBH coordinates were taken from the background-subtracted, subsampled F435W image (Lauer et al. 2012, private communication) and converted to the aligned $K'-$band image coordinates. The SMBH position is marked with the black cross in each panel in Fig. 3.7.

3.3.5 Spatial binning

Fitting the precession rate of the disk requires a very high signal-to-noise ratio (SNR). The SNR of the data varies over the FOV and was calculated empirically. For each spaxel, we fit a straight line in a region of the spectrum dominated by the stellar continuum between 2.270 μm and 2.280 μm. After dividing by the fitted line, the SNR was estimated as the mean of the normalized flux divided by the standard deviation. The SNR map is shown in Fig. 3.2, center panel.

The data was spatially binned using a Voronoi tessellation algorithm (Cappellari & Copin 2003), that optimally sums spaxels until a target SNR is reached while enforcing a roundness criterion on the resulting bins to ensure the resulting bins are as compact as possible. Spaxels already at or above the target SNR remain unbinned. We used the SNR map thus generated to spatially bin the spaxels to a target SNR of 40. The resulting bins and their SNR are shown in Fig. 3.8. Spaxels near P1, P2, and the SMBH remained unbinned, while the fainter outer regions of the eccentric disk and the innermost bulge were optimally binned. Spectra in the binned spaxels were summed and their errors combined in quadrature. Spaxels with a very low initial SNR (<2) on the very edge were masked and discarded in the following analysis.

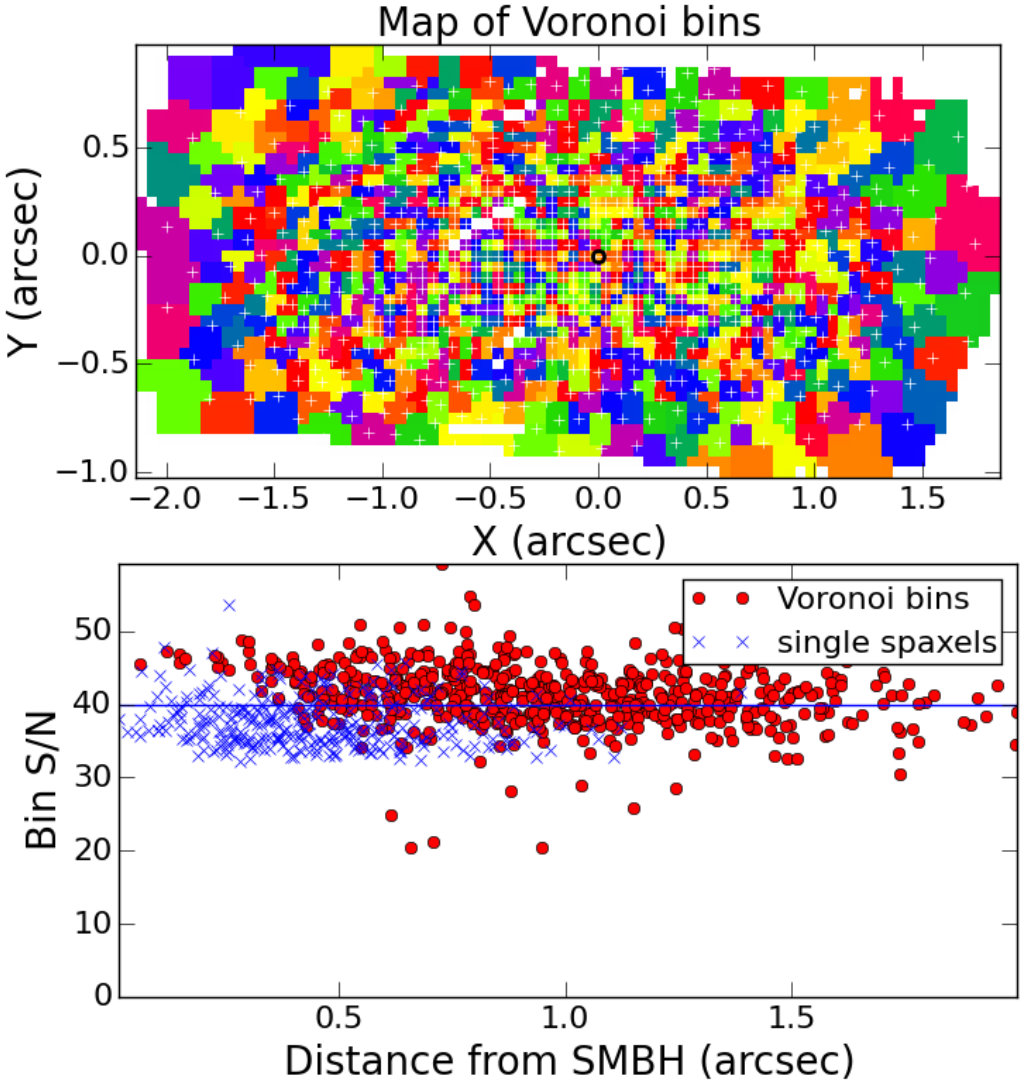

Figure 3.8 *Top:* Spatial bins determined via Voronoi tessellation (Cappellari & Copin 2003). Spaxels with an initially high SNR remain unbinned, while spaxels with a lower initial SNR are binned until their final combined SNR is roughly 40. The colors are randomized to emphasize bin boundaries. *Bottom:* The final SNR for each bin as a function of distance from the SMBH.

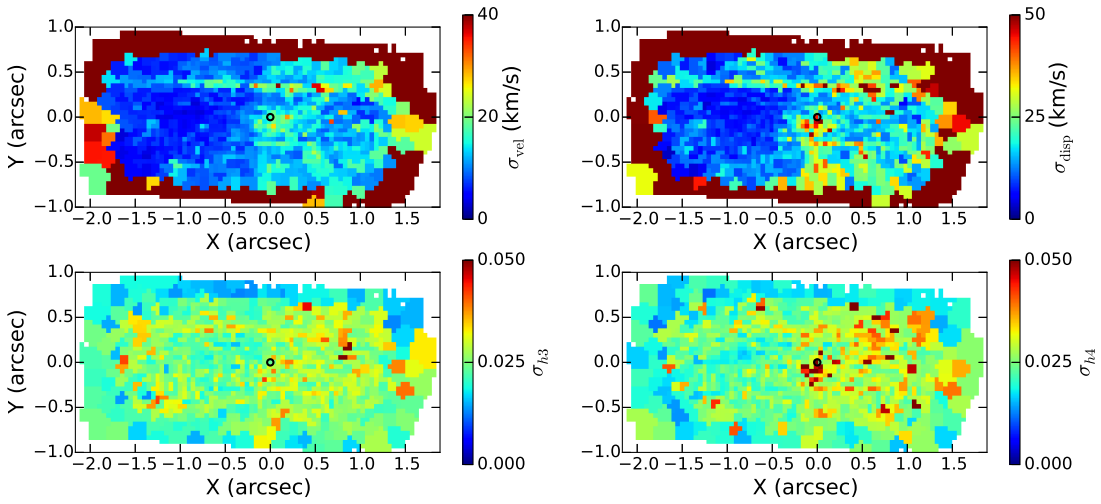

Figure 3.9 Monte Carlo error maps for the velocity (*top left*), dispersion (*top right*), $h3$ (*bottom left*), and $h4$ (*bottom right*). In all panels, the SMBH position is marked by the black circle.

3.3.6 Kinematic fitting

Kinematics were extracted using the penalized pixel fitting method (pPXF) described in Cappellari & Emsellem (2004). This method fits the observed spectrum with a linear combination of spectral templates, convolved by a line of sight velocity distribution (LOSVD), which we parameterized as a fourth-order Gauss-Hermite expansion of a Gaussian profile (Appendix A of van der Marel & Franx 1993). The moments of the best-fit LOSVD (including v, σ, and the higher order moments h_3 and h_4) and the weights of the spectral templates were returned. The Gemini GNIRS spectral template library (Winge et al. 2009), a library of evolved and main sequence late-type stars observed in the $K'-$band at $R \sim$5900, was used as inputs to pPXF. Only those templates observed in both the blue (2.15–2.33 μm) and the red (2.24–2.43 μm) modes were used, for a total of 23 template stars. The final template library covers G4–G5 II, F7–M0 III, K0 IV, and G3–K8 V stars. Independent fits were performed for each spaxel over the range 2.185–2.381 μm to obtain measurements of v, σ, h_3 and h_4.

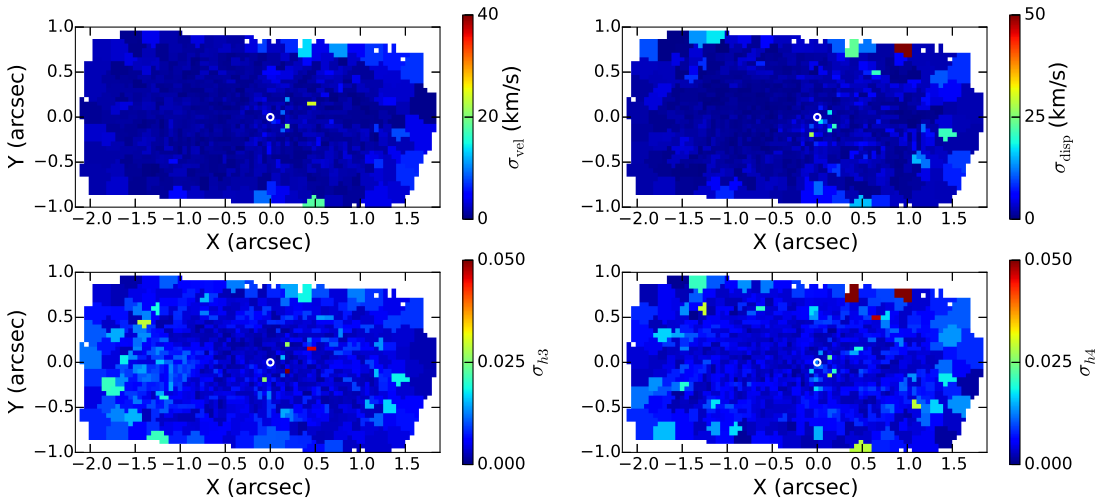

Figure 3.10 Jackknife error maps, to test for template mismatch to the data for the velocity (*top left*), dispersion (*top right*), $h3$ (*bottom left*), and $h4$ (*bottom right*). In all panels, the SMBH position is marked by the white circle.

Measurement errors on the LOSVD moments were assessed via a Monte Carlo (MC) analysis using 100 simulations. In each simulation, the input spectrum was randomly perturbed within the 1σ flux errors and the pPXF fits were recalculated. The uncertainty of each LOSVD moment (i.e., mean, σ, $h3$, $h4$) was taken as the standard error of the mean of the fitted moments from the MC trials. Error maps are shown in Fig. 3.9. The median errors are 11.3 km s^{-1} on v and 16.7 km s^{-1} on σ.

In addition to measurement errors, mismatch between the spectral templates and the intrinsic stellar population can provide a source of systematic error. The magnitude of this error was assessed via a jackknife analysis. One spectral template at a time was dropped from the library used in the fitting routine. pPXF fits were run for each of these 23 template library subsets, and the systematic errors from template mismatches were calculated as the standard error of the mean of the resulting outputs. Error maps are shown in Fig. 3.10, and the median errors are 1.3 km s^{-1} on v and 1.6 km s^{-1} on σ. These errors are nearly an order of magnitude lower than the measurement errors, and thus negligible compared to the observational error. We disregard this source of error in the remainder of the analysis.

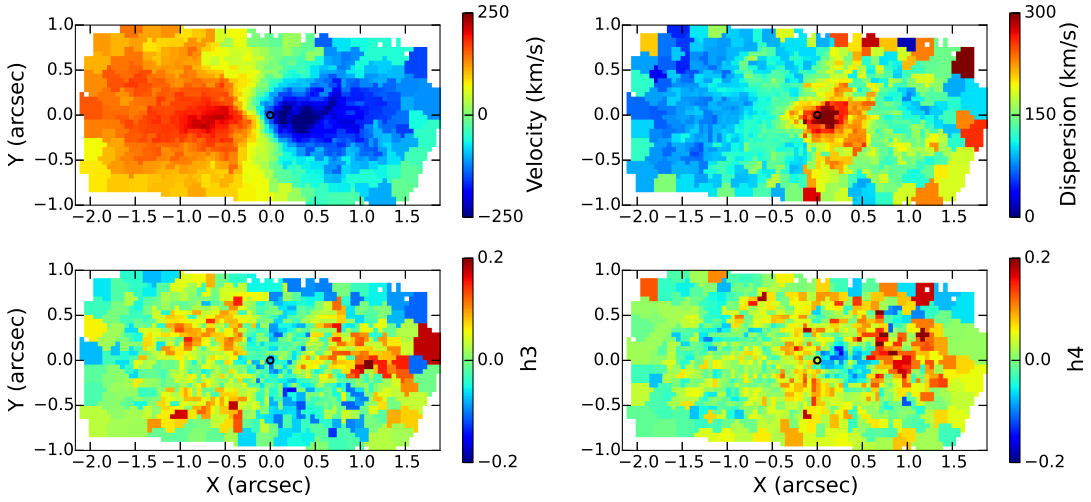

Figure 3.11 Kinematic maps, as calculated with pPXF (see text). In all panels, the SMBH position is marked by the black circle. *Top left:* Velocity map, shifted by the systemic velocity. *Top right:* Velocity dispersion. *Bottom left:* $h3$, or the first asymmetric higher-order moment of the LOSVD. *Bottom right:* $h4$, or the first symmetric higher-order moment of the LOSVD.

3.4 RESULTS

3.4.1 Kinematics of the eccentric disk

The results of the pPXF kinematic fitting are shown in Figs. 3.11 and 3.12. The velocity map shows a clear rotation signature but with a slight asymmetry in the morphology of the velocity peaks. In addition, the peak of the velocity is offset from the P1 peak flux (Fig. 3.13). There is also an asymmetry in the magnitude of the velocities on either side of the disk, with maxima of 222.9±6.6 km s^{-1} on the northeast side and −311.8±16.0 km s^{-1} on the southwest side. In addition, the zero of the velocity gradient does not coincide with the SMBH position, but is offset by 0.″15 towards P1, which is consistent with previous long-slit measurements (Bender et al. 2005).

The dispersion is peaked close to but not at the position of the SMBH as is shown in the zoomed kinematic maps in Fig. 3.12 and in the contour plot in Fig. 3.13. The dispersion reaches a maximum of 381.3±55 km s^{-1} at an offset in (x, y) of (+0.″09, −0.″1) from the

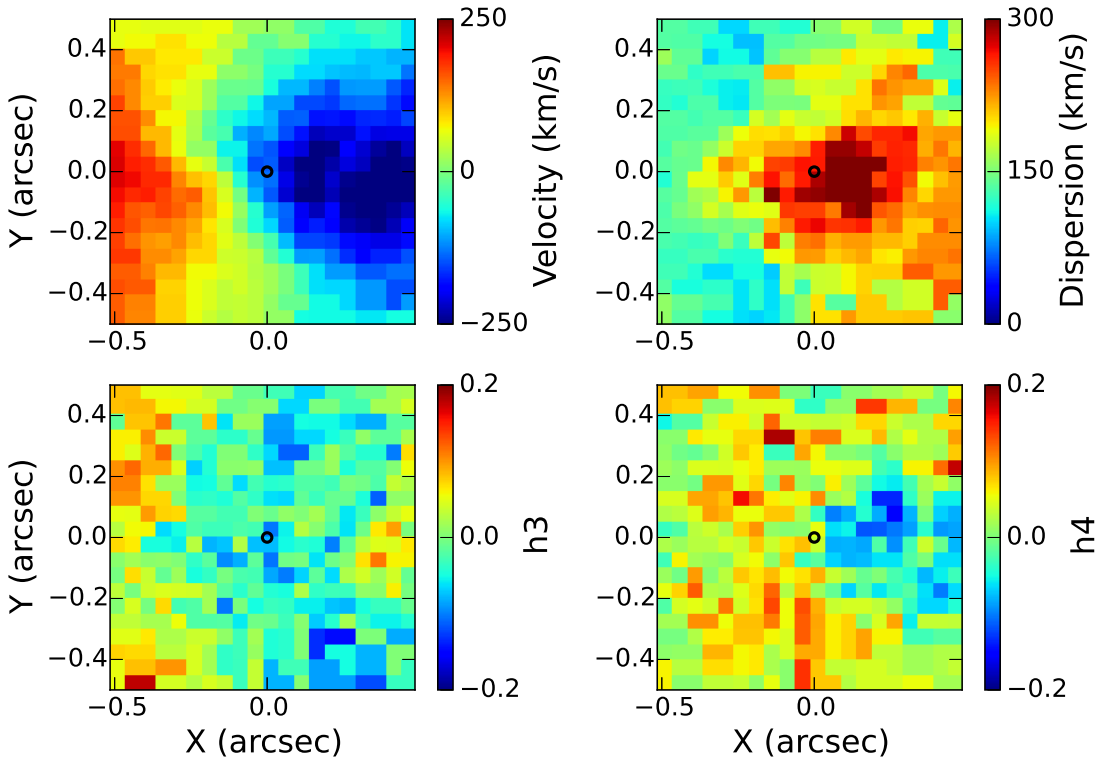

Figure 3.12 Kinematic maps from Fig. 3.11, zoomed in to the central arcsec around the SMBH (black circle). *Top left:* Velocity map, shifted by the systemic velocity. *Top right:* Velocity dispersion. *Bottom left:* $h3$ *Bottom right:* $h4$.

SMBH, or a distance of 0.″13 on the P2 side. The wider dispersion peak ($\sigma > 200$ km s^{-1}) is concentrated on the P2 side and extends towards P1.

Overall, the maps for the higher order moments $h3$ and $h4$ are quite noisy and trends are difficult to discern. There is a possible enhancement of $h4$ on the P1 side of the SMBH, but the results are not robust. We find that the significance of the $h3$ and $h4$ maps are particularly sensitive to the bulge subtraction.

3.4.2 Comparison to previous multi-wavelength imaging

Closer examination of Fig. 3.7 shows that there are clear differences in the structure of the stellar population at each wavelength; notably, P3 is bright and compact only in the F330W

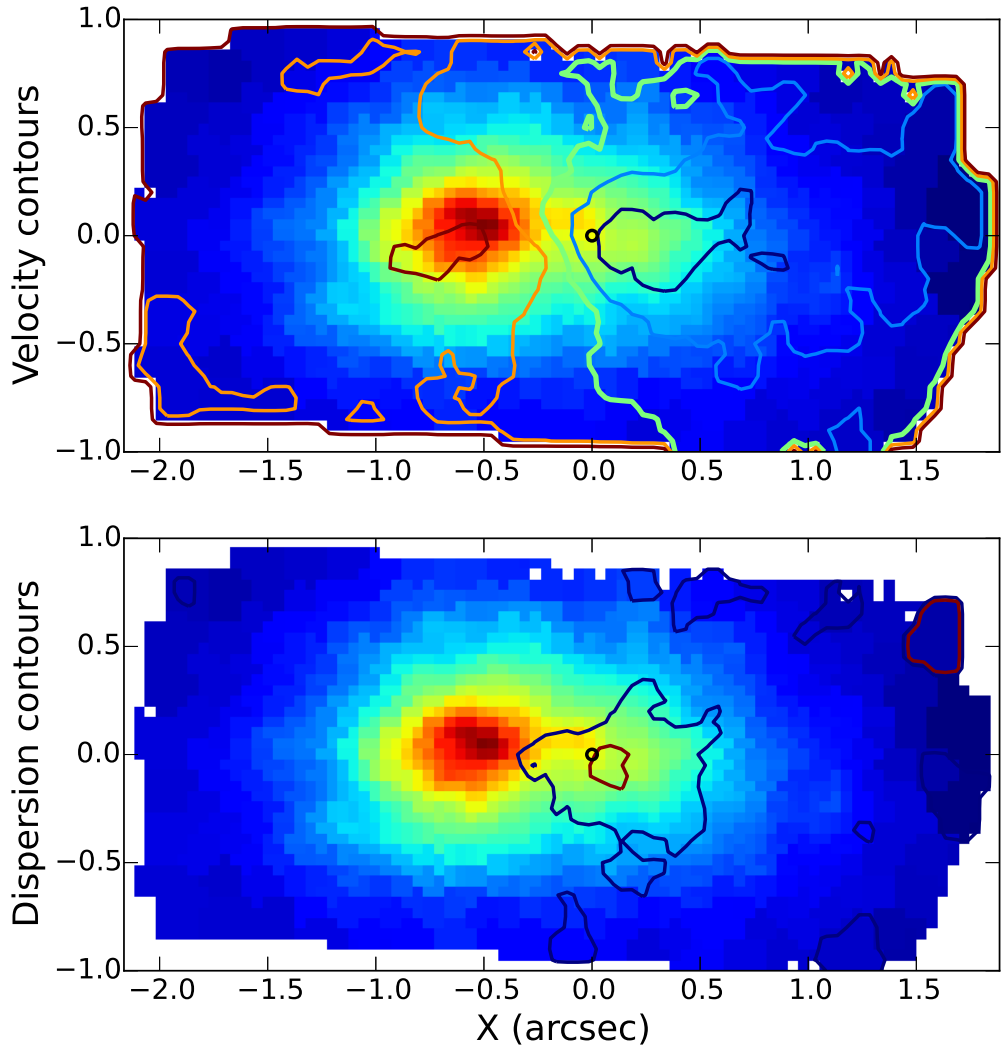

Figure 3.13 Kinematic contours overlaid on the OSIRIS cube, collapsed in the wavelength direction. In both, the contours have been slightly smoothed and the SMBH is marked with a black circle. *Top:* Velocity contours, in steps of 100 km s^{-1}, with the lowest contour at -200 km s^{-1} shown in dark blue. *Bottom:* Dispersion contours, in steps of 100 km s^{-1}, with the lowest contour at 200 km s^{-1} shown in dark blue.

and F435W frames and is dark in the NIR. Figure 3.14 shows the inner 0.″2 in the F330W, background-subtracted F435W (Lauer et al. 2012, private communication) and K' images, with the SMBH position marked. In contrast with the bluer images, there is little to no flux at the position of P3 and the SMBH in the NIR, indicating a separation of the young and old stellar populations in the nucleus.

A clearer comparison of the difference between the flux maps at two different wavelengths can be seen in Fig. 3.15. Lauer et al. (1998) observed the nuclear eccentric disk with HST/WFPC2 in three filters: F300W, F555W, and F814W. We show their F555W flux map in comparison with the OSIRIS flux map. There are clear structural differences visible between the two flux maps, particularly around the P1 peak. In addition, the morphology differences seen around the SMBH in Fig. 3.7 can been seen here: the secondary P2 peak is more northerly in the OSIRIS data than in the F555W image.

This structural difference can also be seen in one-dimensional cuts across each image (Fig. 3.16). A 1D cut has been taken across each frame in Fig. 3.7 at the PA of the HST/STIS long slit observations (see § 3.4.3) and passing through the SMBH. Each 1D cut has been flux calibrated according to the published instrumental zero-points. The nucleus is much brighter in the NIR than at UV or optical wavelengths, so offsets in magnitudes (shown in the figure legend) have been added to each cut to equalize them on the P1 side. The UV peak at the origin in the F330W and F435W frames is apparent. The optical bandpasses show an extended, shallower flux peak roughly coincident with the SMBH position and extending slightly to the southwest. However, the H and K' flux cuts do not show this shallower peak and instead are flat from the SMBH position to the cutoff at the southwest edge.

3.4.3 Comparison to previous spectroscopy

The nucleus of M31 has been well studied with both ground and space-based spectroscopic observations. Several recent studies are summarized in Table 3.3. In this section, we compare the OSIRIS kinematics with two high resolution data sets: HST/STIS long-

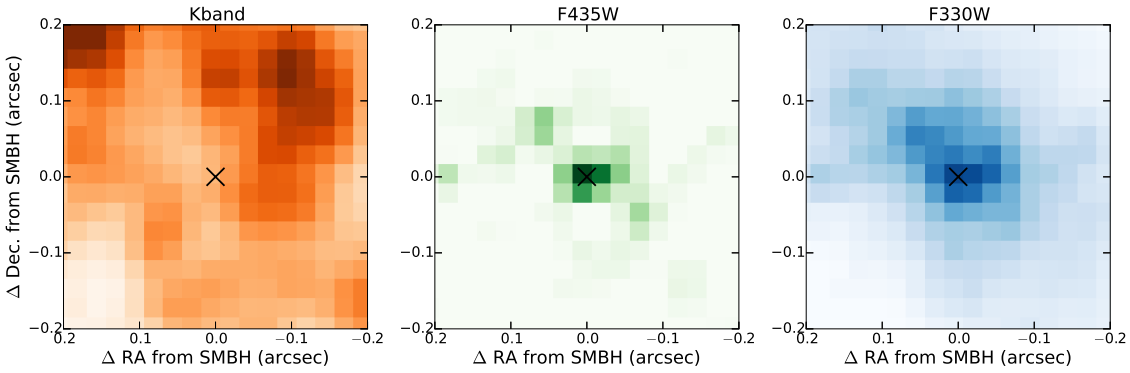

Figure 3.14 Position of the SMBH, taken as source 11 in HST/ACS F435W in Lauer et al. (2012) and calculated in the NIR by aligning with the UV data (see text). The SMBH is shown as the black cross in each panel. Note that P3, coincident with the SMBH and bright in the bluer bandpasses, is not seen above the detection limit in the $K-$band image. *Left:* NIRC2 $K-$band image, *center:* background-subtracted F435W image (Lauer, private communication), *right:* F330W image. All frames have been aligned and scaled to the F330W image ($0.025''$ pixel^{-1}).

slit observations reported in Bender et al. (2005, hereafter B05) and ground-based IFS observations reported in Bacon et al. (2001, hereafter B01).

Comparison with STIS

HST/STIS long-slit spectroscopy was obtained for the nucleus of M31 in July 1999; the full analysis was published in B05. Spectra were taken both in blue (2900–5700 Å) and red (8272–8845 Å, the Ca triplet) modes; we confine our discussion solely to the red mode. The

Table 3.3 Data Quality Comparison

Instrument	Filter	FWHM	Reference
HST FOC	$\sim B$	$\sim 0\farcs05$	Statler et al. (1999)
CFHT SIS	$\sim I$	$0\farcs63$	KB99
CFHT OASIS	$\sim I$	$0\farcs41$–$0\farcs5$	B01
HST STIS	$\sim I$	$0\farcs12$	B05
Keck OSIRIS	K	$0\farcs12$	this work

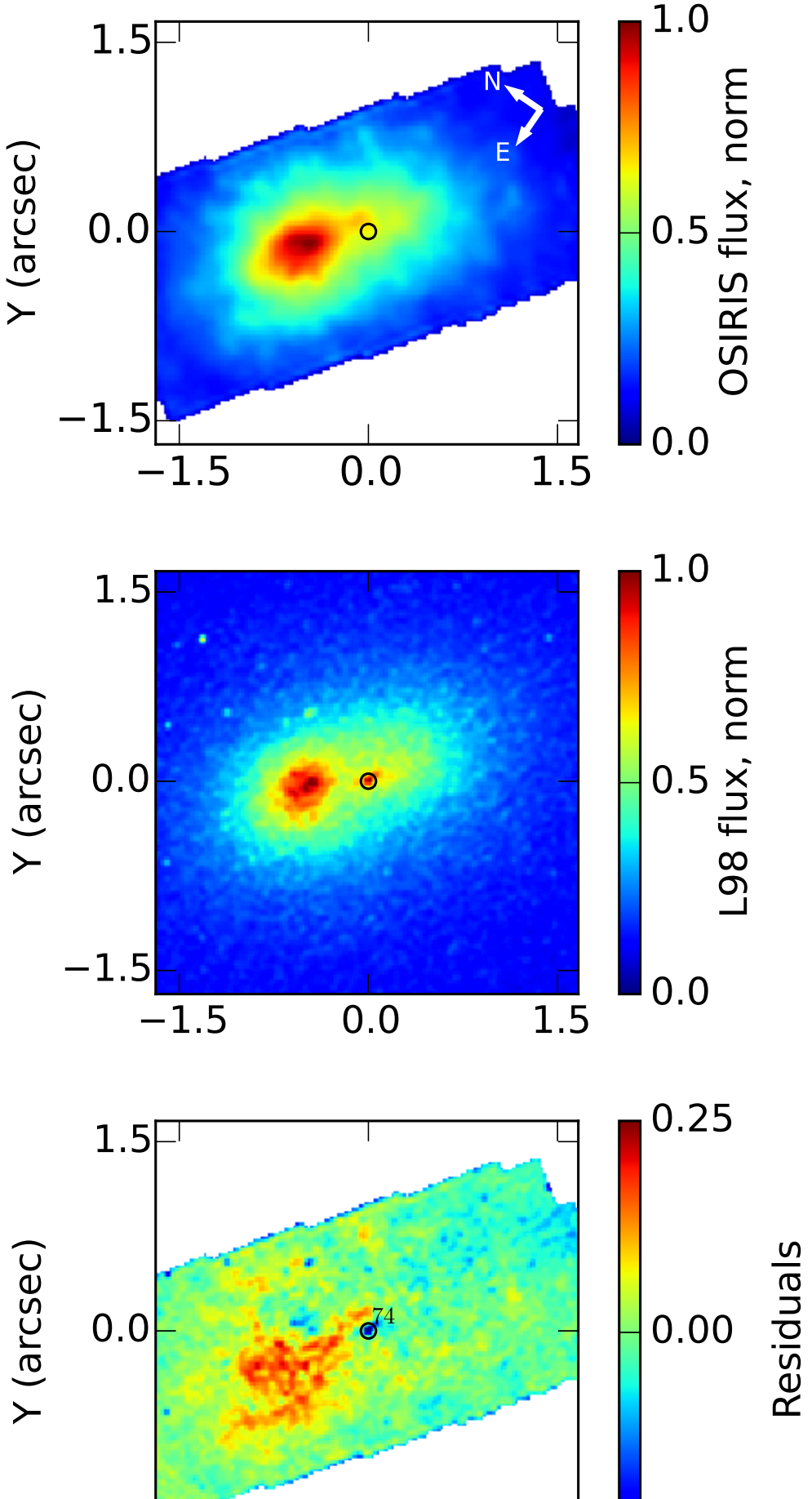
1.5
0.0
−1.5
−1.5
0.0
1.5
Y (arcsec)
N
E
1.0
0.5
0.0
OSIRIS flux, norm
L98 flux, norm
0.25
0.00
Residuals
74

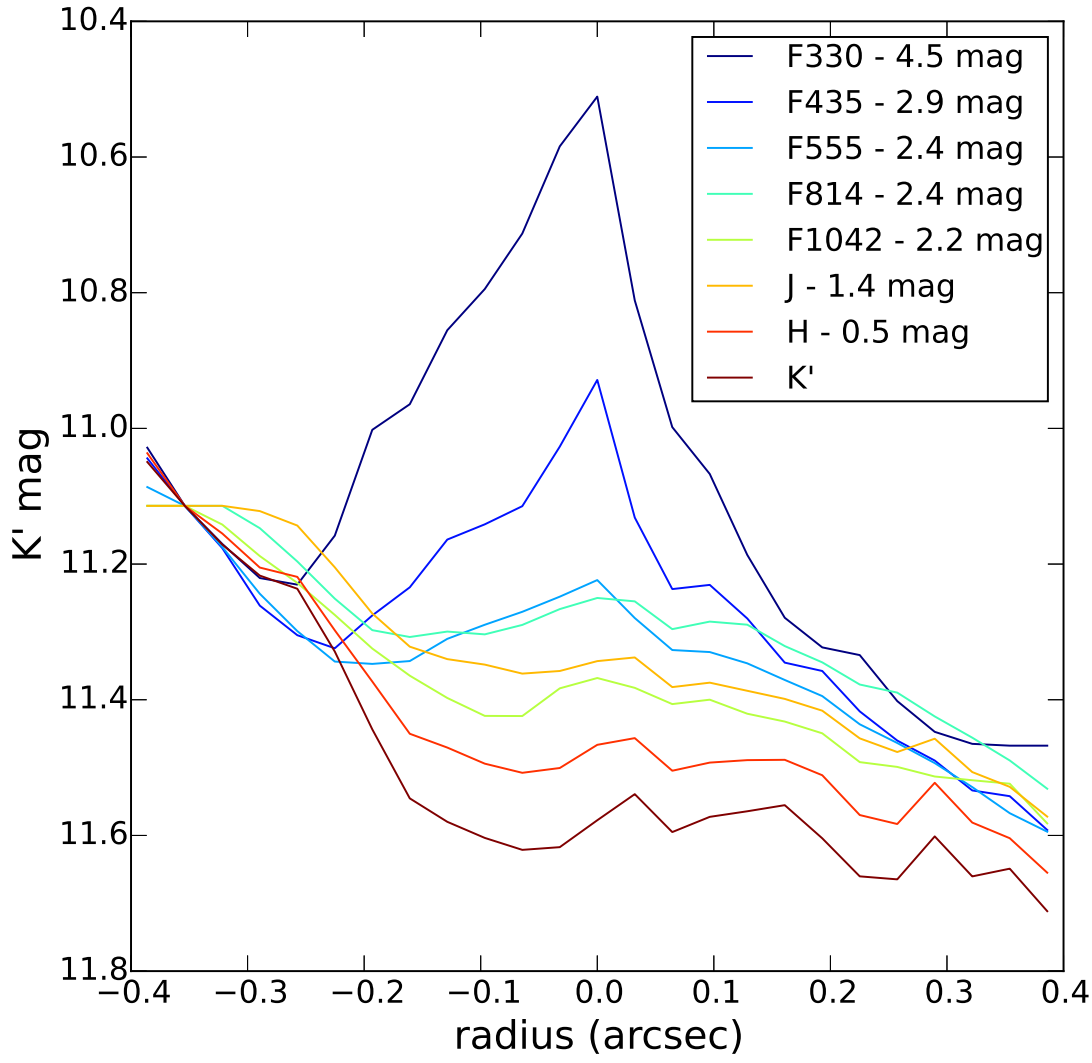

Figure 3.16 One-dimensional cut across each of the eight wavelength images, at a PA of 39° (e.g., the STIS slit PA, § 3.4.3). Offsets have been added to the cuts in each wavelength, except for the F2125 cut, the brightest wavelength. The offsets were chosen so the flux cuts aligned at roughly the position of P1. The additive magnitude offsets are indicated in the legend.

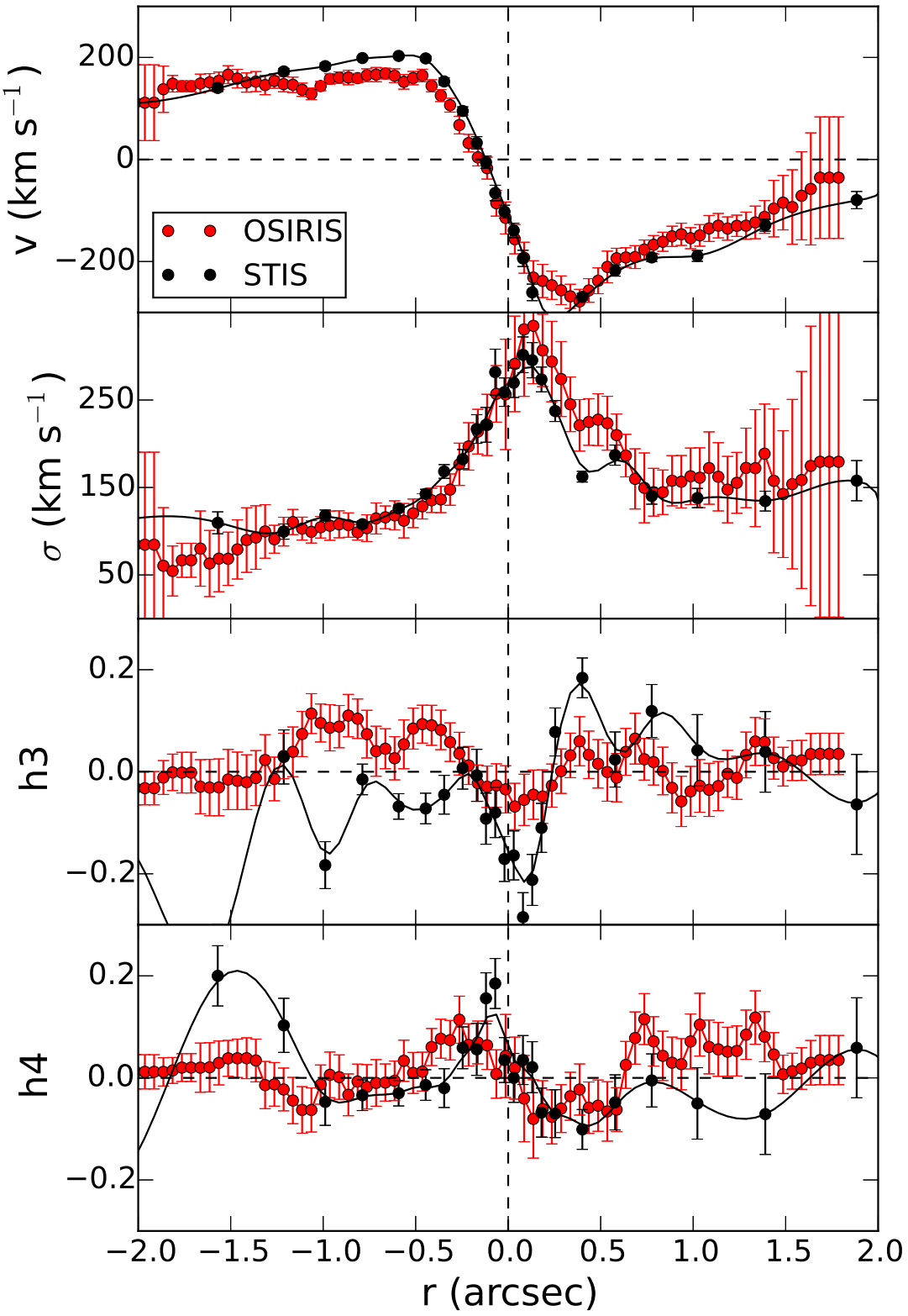

Figure 3.17 Comparison of OSIRIS and STIS kinematics. The STIS data were taken at a PA of 39° and are shown as black points. The STIS data have been smoothed along the slit by the OSIRIS PSF; the smoothed STIS data are shown as the solid black line. A 0.″1 width cut, to represent the STIS slit, has been taken across the OSIRIS kinematics at the STIS PA; those data, along with the Monte Carlo errors, are shown in red. All data have been bulge subtracted. The SMBH position is at 0.″0, and radius increases towards the southwest.

slit was oriented at a PA of 39°, along the major axis of the optical disk. The slit width was 0.″1 and the estimated resolution is FWHM = 0.″12.

We compare the kinematics reported in B05 with our OSIRIS kinematics in Fig. 3.17. In addition to the original STIS kinematics, we show the STIS kinematics smoothed along the slit by a Gaussian kernel derived using the OSIRIS PSF. The comparison to the OSIRIS kinematics was derived by taking a cut across the kinematic maps in Fig. 3.11 at the STIS PA. Each point along the STIS slit is represented by the mean of three OSIRIS spaxels orthogonal to the slit to match the STIS slit width, and the errors are taken as the Monte Carlo errors of the same spaxels, added in quadrature.

Though overall the kinematics reported by STIS and by OSIRIS are similar, there are several inconsistencies, particularly in the velocity and dispersion. Overall, while the velocity gradient from the OSIRIS data is well matched to that from STIS, the OSIRIS data show lower peak velocities on both the red- and blue-shifted sides of the nuclear disk than the STIS kinematics. In addition, the wings of the velocity profile from OSIRIS are lower than those from STIS, which may point to residuals arising from differences in the bulge subtraction methods. The peak dispersion values are the same, within the errors, but the OSIRIS dispersion peak is broader, with a possibility of a secondary dispersion peak at 0.″5, on the P2 side.

Comparison with OASIS

AO corrected integral field spectroscopy was obtained by the OASIS instrument on CFHT and first presented in B01. Two different mosaics of different spatial resolution were presented, with resolution ranging from 0.″41 to 0.″5. Similar to the STIS data, the chosen wavelength range was 8351–9147 Å to optimize observations of the Ca triplet. OASIS provides a $4'' \times 3''$ FOV.

We show the bulge-subtracted OASIS kinematics in Fig. 3.18. These kinematics were extracted along the OASIS kinematic major axis (PA = 56.4°) and were initially presented in B01 (their Fig. 10, solid line). We also show a cut across the OSIRIS kinematics at

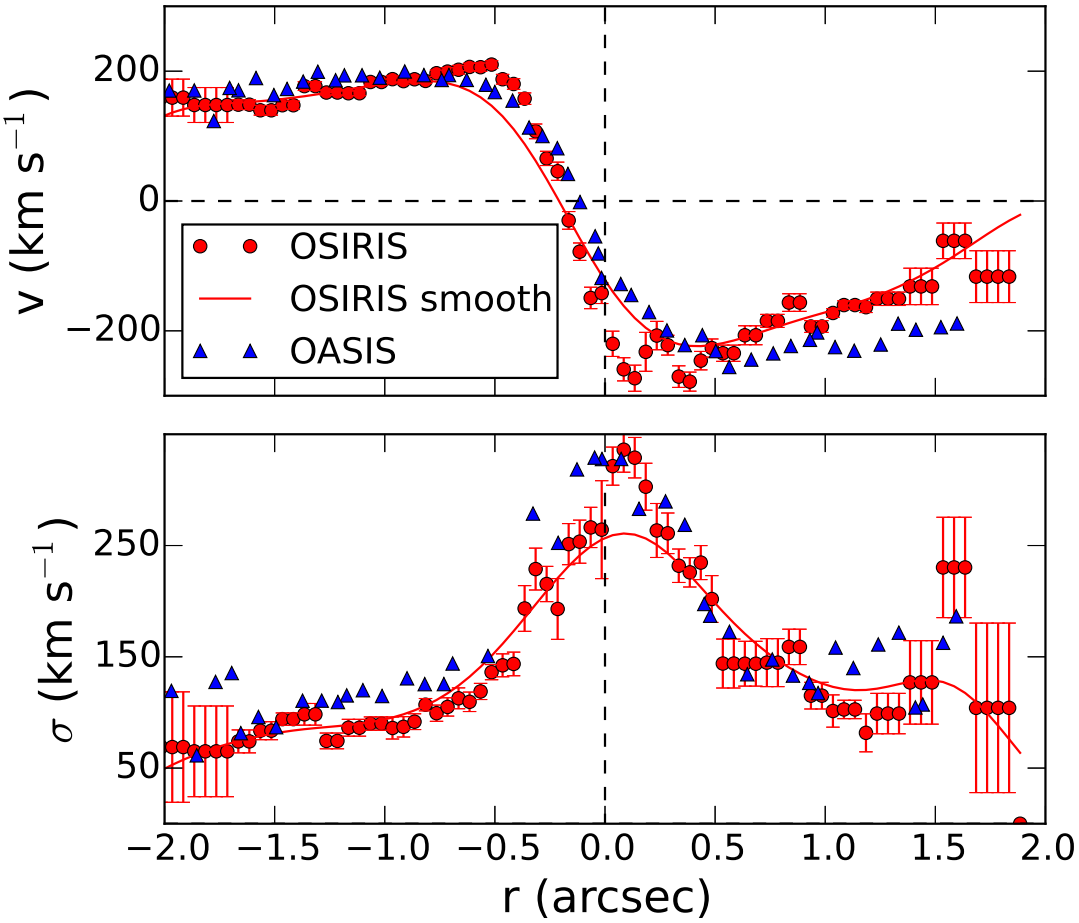

Figure 3.18 Comparison of OSIRIS and OASIS kinematics. The OASIS data, shown in blue and taken from their Fig. 10, are taken at a PA of 56.4°, which they identify as their kinematic major axis. The cut across the OSIRIS data, shown in red, is taken at the same PA, through our SMBH position and parallel to the long axis of the OSIRIS FOV. The red curve shows the OSIRIS kinematics smoothed to the OASIS resolution. All data have been bulge subtracted. Our SMBH position is at $0\farcs0$, and radius increases towards the southwest. The OASIS data have been shifted by $-0\farcs1$ to align the velocity gradients.

the same PA. The red points are the original OSIRIS kinematics and the red curve is the OSIRIS kinematics smoothed to the OASIS resolution. The B01 velocity and dispersion profiles have been shifted by $-0\farcs1$, to better align the velocity gradient with that of the OSIRIS data and to account for differing SMBH positions. Overall, the OASIS velocity profiles agrees well with the smoothed OSIRIS data, and is similar to the correspondence seen between the OASIS and STIS kinematics, as reported in B01 (their Fig. 13). However, the OASIS and OSIRIS kinematics are not quite aligned along the radial direction. This offset is potentially due to a difference in SMBH position between the OASIS and OSIRIS data; shifting the comparison cut in the OSIRIS data by up to $0\farcs1$ from our SMBH position bring the data into closer alignment along the radial direction, though the correspondence is still not perfect. Also, smoothing the OSIRIS kinematics to match the OASIS resolution brings the two velocity profiles into agreement, but the reported OASIS dispersion peak is higher than that seen in the smoothed OSIRIS data.

3.5 MODELS

We compare the OSIRIS data to the flux and kinematic models from Peiris & Tremaine (2003, hereafter PT03). These Keplerian models were originally fit to HST photometry and ground-based long-slit data (KB99) to determine the orientation of the eccentric disk with respect to the larger-scale galactic disk. In this work, we add rigid-body rotation to the models and determine the best-fit precession rate and orientation using the OSIRIS data. Details of the model fitting are described in §3.5.1 and results on the disk orientation and precession are presented in §3.5.2 and §**??**, respectively.

3.5.1 Model fitting

The original disk models consisted of $\sim 10^7$ particles in disk-plane coordinates, which were rotated to two different orientations as described in PT03: the *aligned* model, matched to the orientation of the large-scale galactic disk, and the *non-aligned* model, with orientation

parameters left free (Table 3.4, columns 2 and 3). The aligned models were a poor fit to both our data and that of PT03, thus we drop the aligned models from the discussion and focus on the nonaligned models. In order to fit the model to the OSIRIS data, the particles from the nonaligned model were first rotated to an orientation of our choosing as specified by three angles: the inclination of the disk with respect to the sky (θ_i), the angle of the ascending node in the sky plane (θ_l), and the angle from the ascending node to the periapse vector (θ_a). A solid body rotation was also introduced by adding a fixed rotation speed, Ω_p (in units of km s^{-1} pc^{-1}), to the disk-plane model velocities. A righthanded coordinate system was assumed, so positive precessions are counterclockwise. For a given set of model parameters, the particles were randomly perturbed in their sky-plane positions using a Gaussian kernel that matched the OSIRIS resolution in order to smooth out features at higher resolutions. The particles were then spatially binned using the tessellated pattern used for the data (§ 3.3.5) and the line-of-sight velocities were binned in increments of 5 km s^{-1}. The resulting model LOSVD was fit using the Gauss-Hermite expansion in the same manner as the observations.

In order to find the best-fit orientation and precession with our new data, a grid search was performed over Ω_p, θ_i, θ_l, and θ_a. First, a coarse grid of angles was centered on the original best-fit nonaligned values and spread over a range of $\pm 15^\circ$ with a step of 5° for each angle. Precession values in the course grid ranged from -30 to $+30$ km s^{-1} pc^{-1} in steps of 5 km s^{-1} pc^{-1}. Near the best-fit value, a finer grid was explored with steps of 1° or 1 km s^{-1} pc^{-1}.

The goodness of fit was tested by calculating the χ^2, or the sum of the squared residuals between the OSIRIS flux or kinematics and that of the model, weighted by the squared flux or MC errors. Only the flux, velocity, and dispersion moments were used in the fitting process, as the $h3$ and $h4$ measurements have lower S/N. For the flux, the OSIRIS data and model were first normalized by dividing by the sum of the flux in each image. Only the inner $1\farcs3$ was used for the calculation. The resulting χ^2_m for each moment, m, was divided by the number of spaxels (1746) within the inner region minus the number of free parameters

(4), to obtain a reduced $\tilde{\chi_m}^2$. The best fitting model across all moments was selected based on a weighted sum $\tilde{\chi}^2 = \sum_m \tilde{\chi}^2_m$ over the flux, velocity, and dispersion moments. The weights used were the minimum $\tilde{\chi}^2_m$ value for each moment, which is equivalent to error re-scaling, in order to prevent any one moment from dominating the fit. The errors on the best-fit parameters were estimated by performing a Monte Carlo analysis using 100 samples of the data. In each, the flux and kinematic maps were randomly perturbed using a normal distribution matched to the MC errors for the data and the $\tilde{\chi}^2$ values were recalculated for every model in the grid. Notably, all Monte Carlo samples yielded the same best-fit model as the original, non-perturbed data; however, the best-fit $\tilde{\chi}^2$ for each MC sample varied. To define a 68% (1σ) confidence interval, we adopted the standard deviation of the $\tilde{\chi}^2$ values from the fine grid models, or $\Delta\tilde{\chi}^2 = 0.07$.

Figure 3.25 maps the sum of the weighted, reduced χ^2 values for the full range of modeled parameters. Figure 3.26 shows the weighted, reduced χ^2 values as a function of each parameter, with the other parameters held constant at their best fit values. The best-fit $\tilde{\chi}^2_m$ for each moment and the combined $\tilde{\chi}^2$ is shown in Table 3.5.

3.5.2 Orientation

Our kinematics and residuals from the original nonaligned models of PT03 are shown in Figs. 3.19, 3.21, and 3.23. We note some discrepancies, particularly in the flux and velocity comparisons. (Following PT03, we note that comparisons between the data and models are only valid within the inner $1\farcs3$.) The flux residuals may be due to the difference in morphology of the stellar population at different wavelengths (§ 3.3.4), as the flux models were originally fit to imaging data taken by HST in filter F555W (originally reported in Lauer et al. 1998) and the kinematics were fit to Ca triplet long slit data from KB99.

The best-fit models and residuals are shown in Figs. 3.20, 3.22, and 3.24. The best-fit orientation is $[\theta_l, \theta_i, \theta_a] = [-32.8^\circ \pm 3.5^\circ, 44.1^\circ \pm 1.8^\circ, -14.5^\circ \pm 14.6^\circ]$. The 1σ errors are derived using the $\Delta\tilde{\chi}^2$ above. Overall, the fitting preferred smaller values of θ_i and larger values of θ_l and θ_a than that found in PT03 (see Table 3.4 for a comparison).

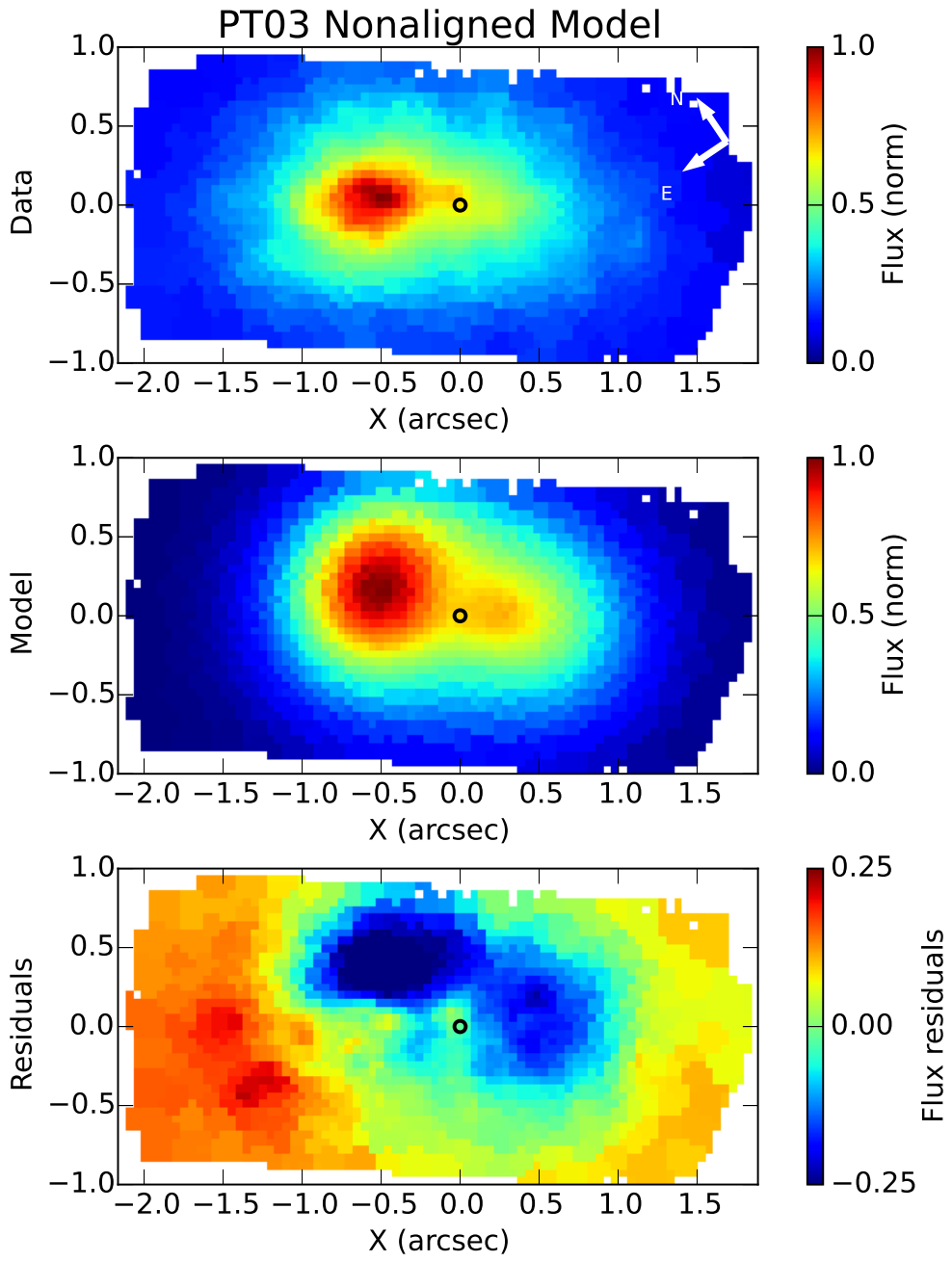

Figure 3.19 Comparison of data with nonaligned models from Peiris & Tremaine (2003). *Top:* Normalized flux in the collapsed OSIRIS data cube, *center:* number of stars per spatial bin (normalized, taken to be equivalent to the flux) in the nonaligned model, *bottom:* residuals, data minus model

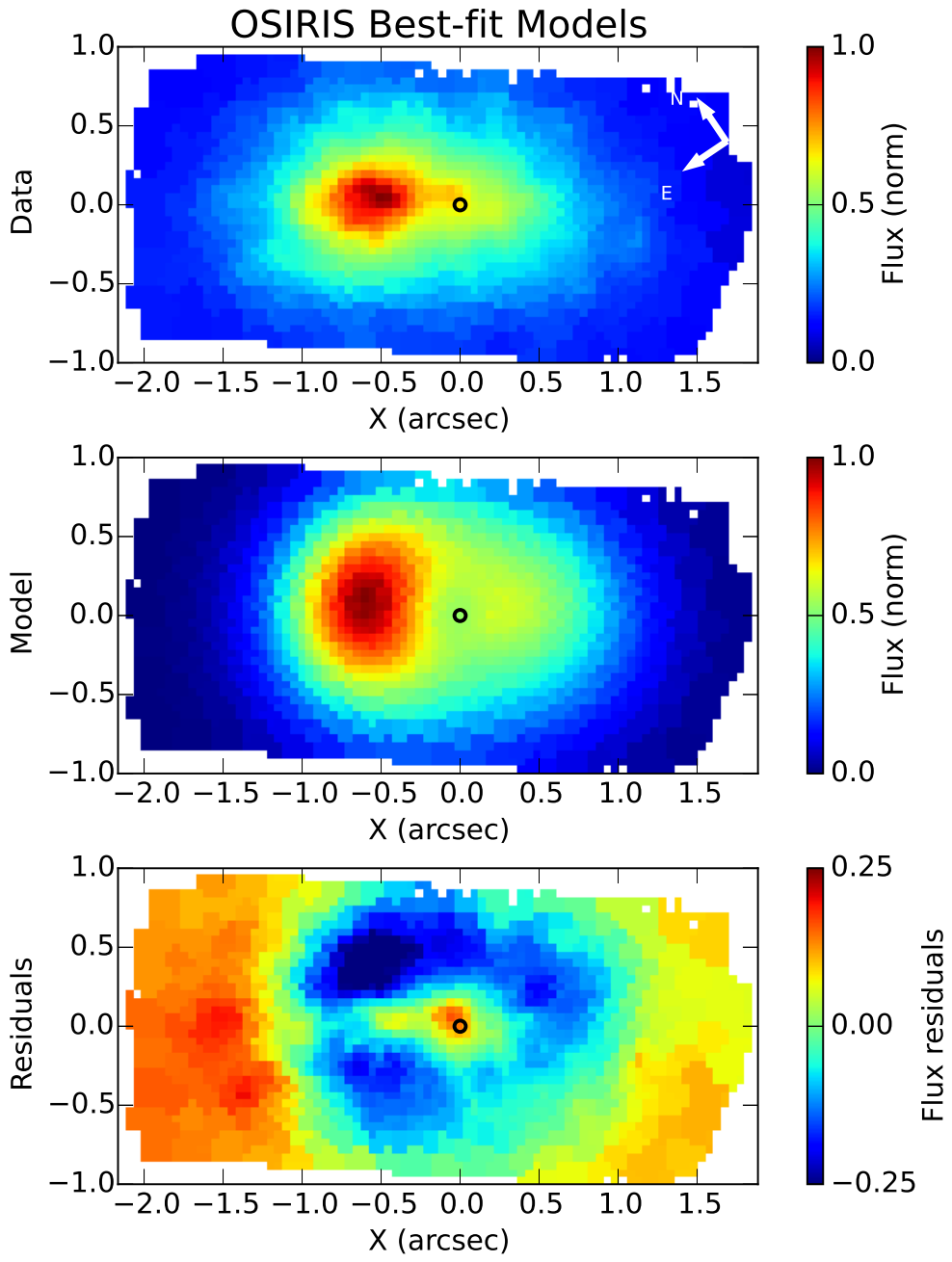

Figure 3.20 Comparison of data with best-fit models. Orientation angles and precession of the models are given in Table 3.4. Panels are the same as in Fig. 3.19.

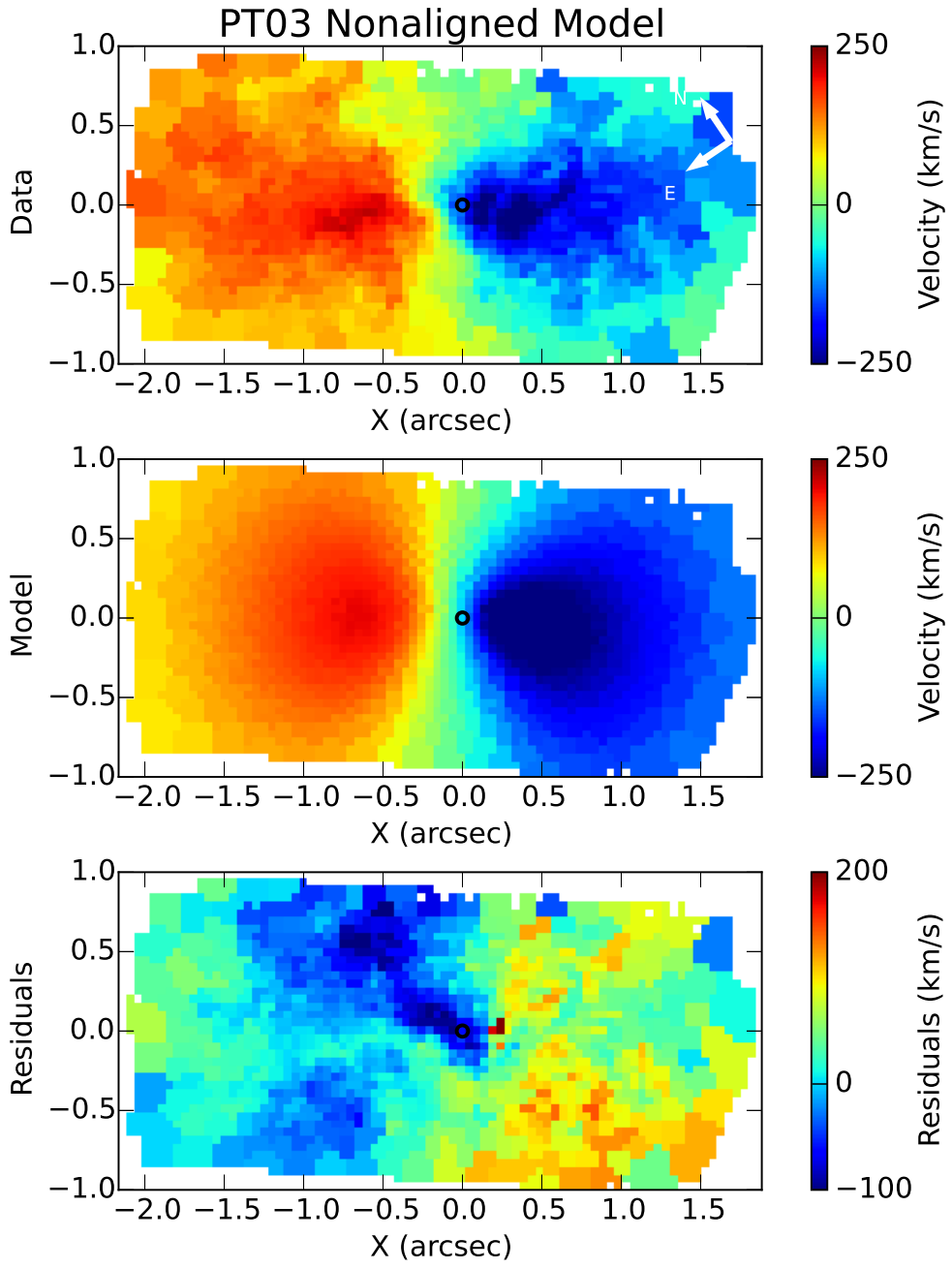

Figure 3.21 Comparison of velocity data and PT03 nonaligned models; similar to Fig. 3.19.

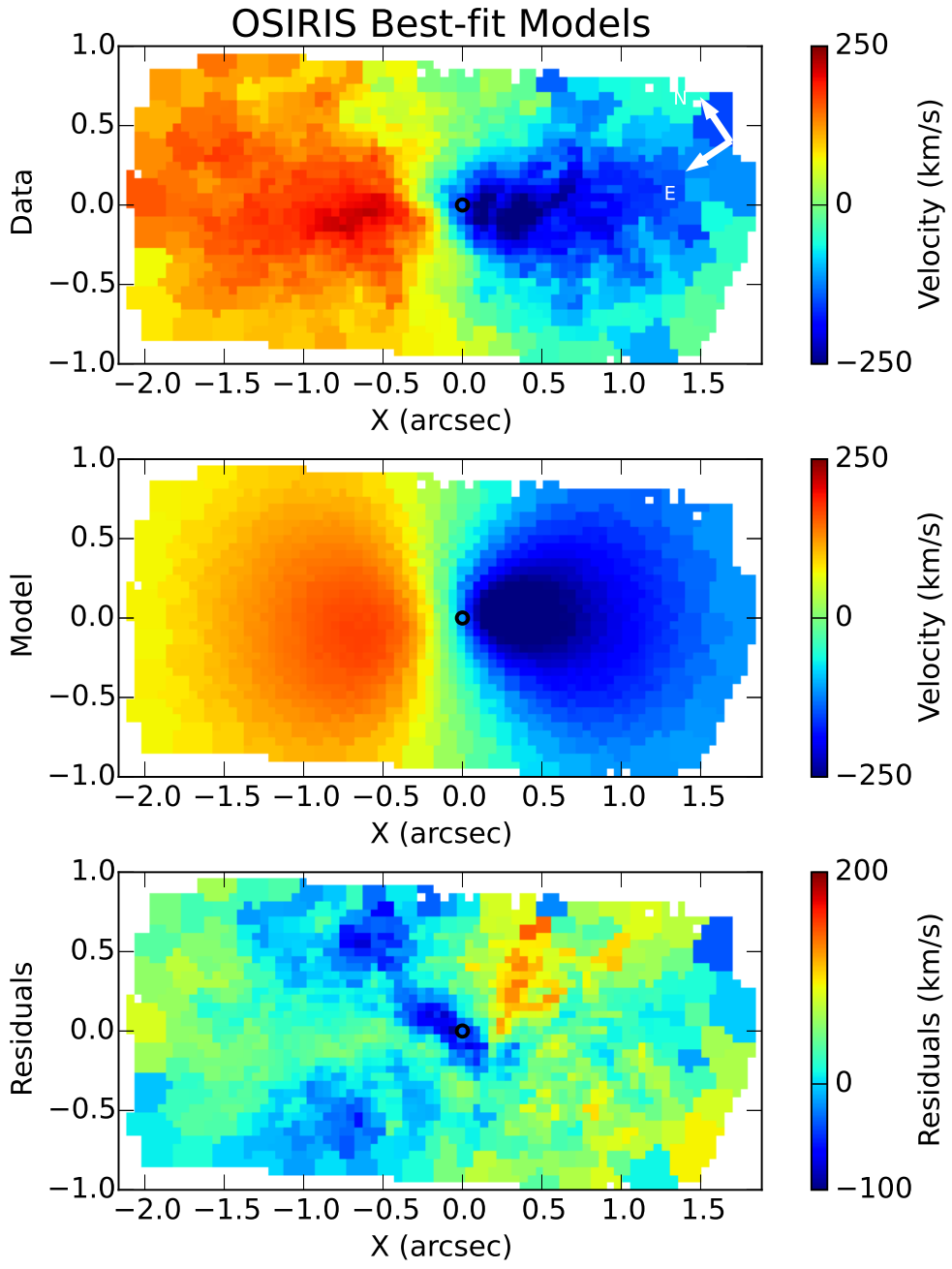

Figure 3.22 Comparison of velocity data and best-fit models; similar to Fig. 3.20.

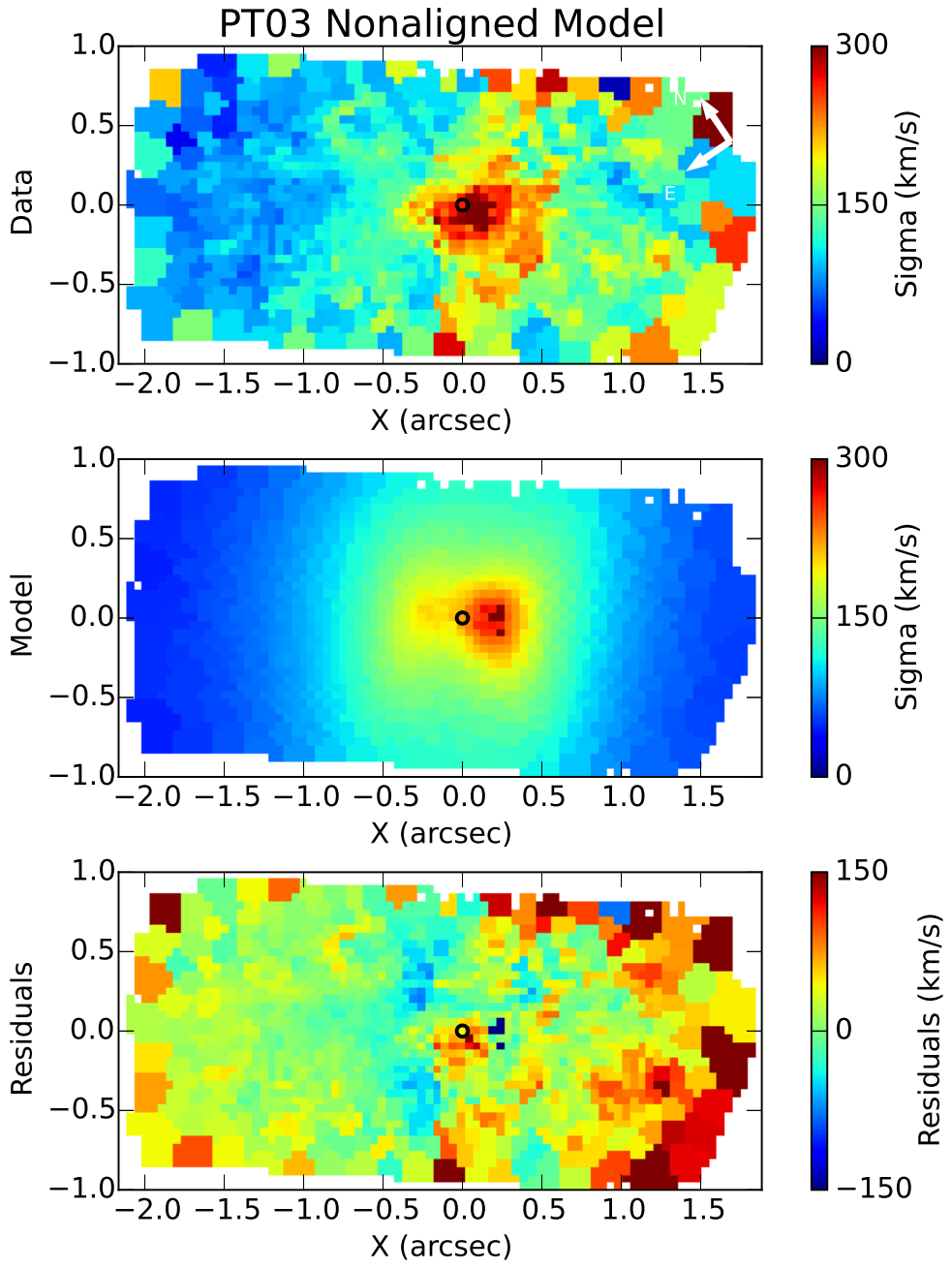

Figure 3.23 Comparison of dispersion data and PT03 nonaligned models; similar to Fig. 3.19.

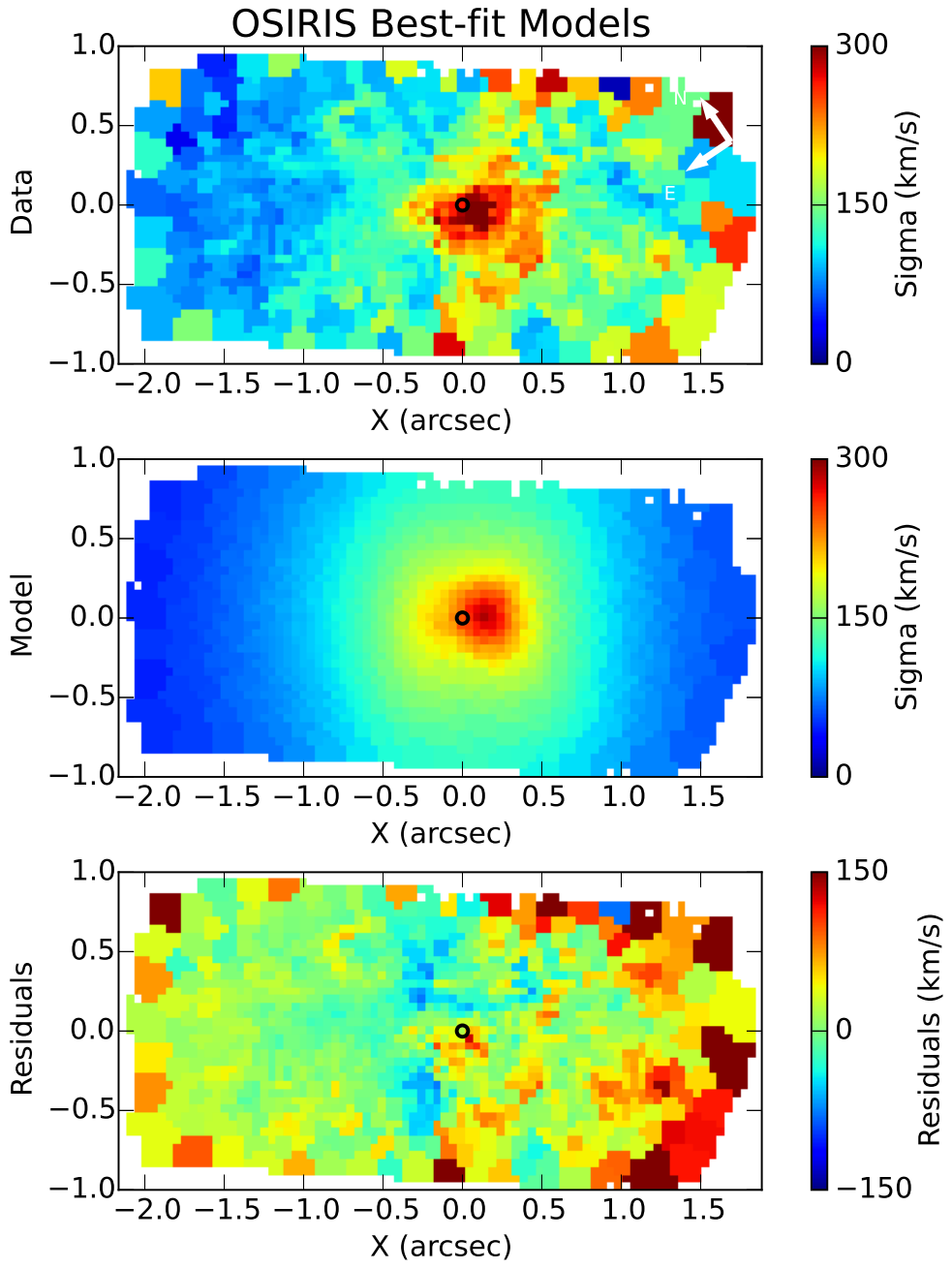

Figure 3.24 Comparison of dispersion data and best fit models; similar to Fig. 3.20.

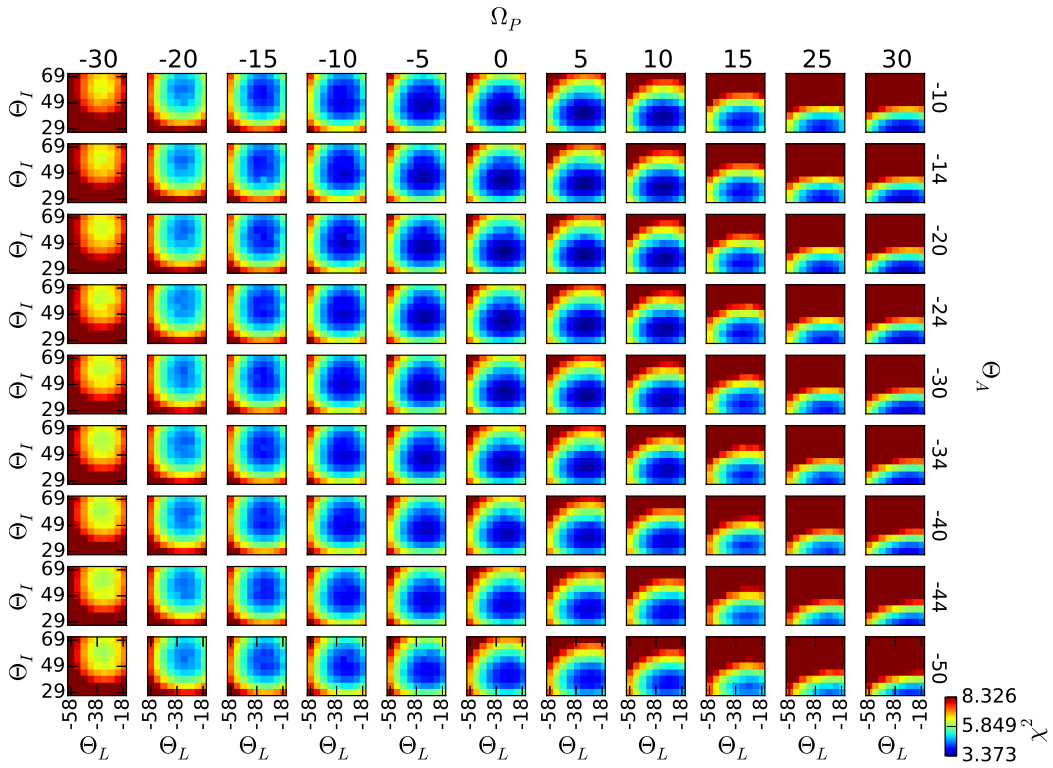

Figure 3.25 Map of the weighted sum of the reduced χ^2 values for the full range of all four modeled parameters (θ_l, θ_i, θ_a, and Ω_P). Each small box shows the range of θ_i (y-axis) and θ_l (x-axis), while θ_a increases along the large-scale y-axis and Ω_P increases along the large-scale x-axis. The color stretch in each panel has been adjusted to emphasize the χ^2 minimum.

Table 3.4 Model Fitting Results

Parameter	Aligned[a]	Nonaligned[a]	Best fit[b]
θ_l	$-52.3°$	$-42.8°$	$-32.8°\pm3.5°$
θ_i	$77.5°$	$54.1°$	$44.1°\pm1.8°$
θ_a	$-11.0°$	$-34.5°$	$-14.5°\pm14.6°$
Ω_P^c	...	...	0.0 ± 3.4

[a]PT03[b]This work[c]Not fit in PT03, units are km s^{-1} pc^{-1}

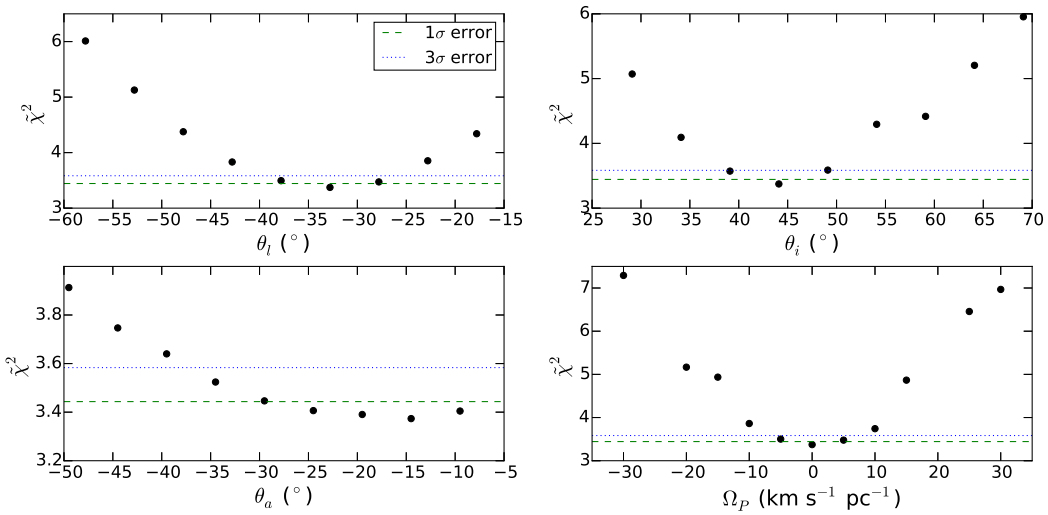

Figure 3.26 The reduced, weighted, and summed χ^2 is shown as a function of the four fitted parameters: θ_l, θ_i, θ_a, and Ω_P. For each, the three non-plotted parameters are held constant at their best-fit value and only the given parameter is varied. The 1σ error, taken as the standard deviation of the minimum reduced, weighted, and summed χ^2 from the MC simulations, is shown as the dashed horizontal line. The 3σ errors from the same is shown as the dotted horizontal line.

Table 3.5 Minimum reduced χ^2 by model

Moment	PT03	TW Ω_P	Best fit moments	Total best fit
Flux	154.8	99.6	95.6	99.7
Velocity	21.9	190.8	11.3	14.1
Dispersion	4.0	3.6	3.1	3.3
$h3^a$	13.2	11.6	7.7	9.5
$h4^a$	8.2	7.4	6.5	6.9
Weighted total	4.7	18.9	...	3.4

3.5.3 Precession

The reduced χ^2 values for the flux and velocity residuals preferred a positive precession, while the dispersion residuals preferred a negative precession, but overall the preferred precession is 0.0±3.4 km s^{-1} pc^{-1}. We show the data, model, and residuals for the best fitting orientation and precession in Figs. 3.20, 3.22, and 3.24.

We also fit the precession using the 1D method formulated in Tremaine & Weinberg (1984, hereafter TW) and modified by Sambhus & Sridhar (2000). Briefly, the original method requires 1D profiles of both the surface brightness and the LOS velocity along the line of nodes, or the intersection of the sky and disk planes. The modified method allows for the profiles to be taken along the P1−P2 line. In either, the formulation is

$$\Omega_P \; sin \; \theta_i \int_{-\infty}^{\infty} dX \; \Sigma \; X = \int_{-\infty}^{\infty} dX \; \Sigma \; V_{\rm LOS}$$

We take the surface brightness and LOS velocity profiles along the P1−P2 line, or parallel to the long axis of our FOV, and calculate the precession along the profile intersecting with the SMBH position. The method allows determination of the precession along strips parallel to this line. The precession along two strips on either side of the profile intersecting the SMBH position is also calculated, for a total of 5 determinations. The standard deviation is taken as the error. Using the best-fit value for θ_i, we derive $\Omega_P = -18.1\pm5.4$ km s^{-1} pc^{-1}.

However, the original method by TW assumes that the disk is thin; the models from PT03 show that the best fit disk is quite thick ($h/r \sim 0.4$). We check the results of the TW method by calculating the precession for the models of the same orientation as the best fit model into which a known precession value has been injected. We find that the values obtained using the TW method for these models are systematically too high. A line is fit to the output TW precessions to calibrate the method for the best fit orientation. We extrapolate the fit to obtain the calibrated TW precession for our data: 62.2±5.1 km s^{-1} pc^{-1}. A model is generated using this precession along with the best-fit orientation

angles and the goodness of fit to the data is calculated (Table 3.5); this precession gives a significantly worse fit to the data than the best-fit precession does, particularly to the velocity map. A comparison of the data and the models derived using the TW precession is shown in Appendix 3.9.

3.6 DISCUSSION

Chang et al. (2007) derived the maximum value for the precession of the eccentric disk, Ω_P, in order for gas released via stellar winds to end up on crossing orbits. Gas on these crossing orbits is able to collide, shock, cool, and fall into orbit around the SMBH on timescales faster than the viscous timescale. There, it collects into an accretion disk around P3 until it acquires enough mass to reach the Toomre instability limit and collapse to form stars. Based on a range of values for the disk thickness (h/r = 0.1–0.3), they calculated that the maximum precession that would allow these crossing orbits was $\Omega_p \lesssim$ 3–10 km s^{-1} pc^{-1}.

The model fitting in § 3.5.1 yielded a best-fit value for the precession equivalent to zero: 0.0±3.4 km s^{-1} pc^{-1}. This is smaller than other values found for the precession of the disk (see Fig. 3.27), but benefits from a combination of 2D FOV coverage and high spatial resolution unmatched by other observational studies. Out of prior observational constraints on the precession, only B01 obtains a similarly small value of Ω_P = 3 km s^{-1} pc $^{-1}$ with their OASIS IFS data and N-body modeling. Sambhus & Sridhar (2002) also fit their models to the IFS observations from B01, but using Schwarzschild-type modeling, obtain a higher value of Ω_P = 16 km s $^{-1}$ pc^{-1}.

Other modeling studies (Jacobs & Sellwood 2001; Salow & Statler 2001, 2004) have fit their models to long-slit spectroscopic data and obtain values of Ω_P ranging from 14 km s^{-1} pc^{-1} to over 30 km s^{-1} pc^{-1}. Sambhus & Sridhar (2000) use a modified Tremaine & Weinberg (1984) method with long-slit spectroscopy to estimate $\Omega_P \lesssim$ (sin 77°/sin i) 30 km s^{-1} pc^{-1}. However, we found that this method produces precession values that are

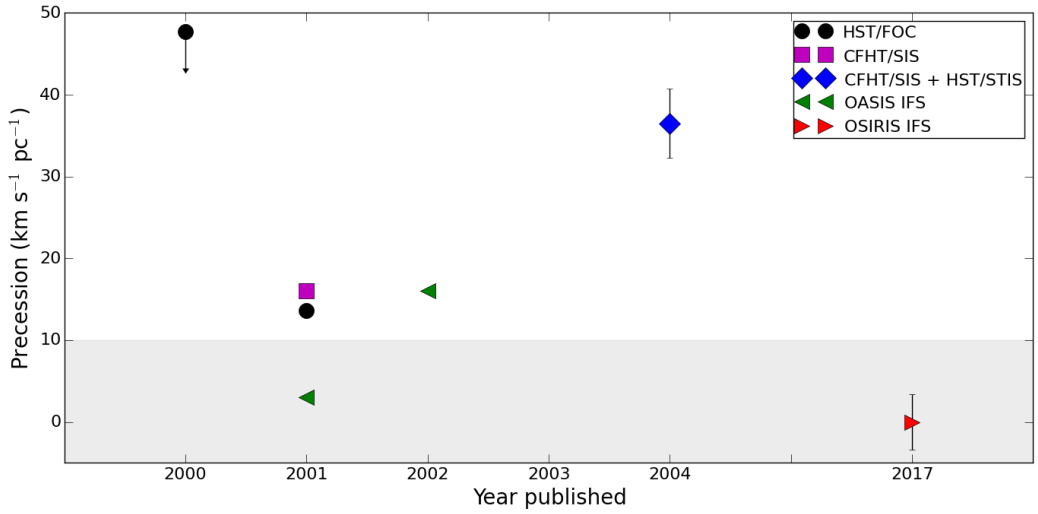

Figure 3.27 Previous estimates of the precession value of the eccentric disk, as a function of year published. Markers represent the source of the observations used in the analysis; all are long-slit observations except for the OASIS IFS green triangles and the red triangle, representing the current work. Error bars and upper limits are shown where provided in their respective papers. The precession value from Sambhus & Sridhar (2000) was given as a function of disk inclination and has been adjusted to match our best-fit disk inclination. The shaded gray box represents the theoretical limits from Chang et al. (2007).

systematically offset from the known input model values and hence this method appears to be unreliable for this system.

Our best-fit precession is in line with the Chang et al. (2007) theory. The lack of precession in the eccentric disk allows gas released via stellar winds to quickly move into the vicinity of P3 and collect there, until enough gas has collected to collapse and form stars every 500 Myr.

Our best-fit disk orientation is tilted with respect to both the PT03 nonaligned orientation and to the larger-scale galactic disk. It is more misaligned with the larger-scale galactic disk than was the PT03 nonaligned model. Examination of Figs. 3.15 and **??** (right panel) shows that this is partly due to the differential morphology of the secondary brightness peak P2 in the NIR (see Appendix 3.10 for a comparison of the nonaligned models with the data they were fit to). In previous observations in the optical, the PA of a line connecting P1 and P2 is 43° (Lauer et al. 1993). However, in our NIR data, the PA of the P1−P2 line is aligned with the long axis of the OSIRIS FOV, or a PA of ∼56°. The angle θ_l has decreased to compensate for this shift in morphology with wavelength. Our best-fit value for θ_l is more in line with that found by Brown & Magorrian (2013, $\theta_l = -35°$) in their modeling of the disk using observations from HST/WFPC2 (Lauer et al. 1998), HST/STIS (B05), and OASIS (B01). In addition, the P1 peak is narrower and more elongated along the P1−P2 line in the NIR than in optical observations. The best-fit value for θ_i, which controls the inclination of the disk, is equivalent to a more face-on disk orientation. The angle θ_a roughly controls the inclination of the disk along the minor axis, and thus effectively adjusts the brightness at P1 and P2 to compensate for the change in the other angles. The source of the morphological differences between the optical and infrared is not understood; however, the 2D OSIRIS spectroscopy can be used to investigate the nature of the stellar populations in the eccentric disk.

The NIR data also allow insight into the distribution of the old stellar population in the nuclear region. Figure 3.7 shows that the UV-bright P3 gives way to a hole in the stellar distribution at redder wavelengths. This lack of cusp at the SMBH is similar to that seen

in the Milky Way (Do et al. 2013). However, the inner core (or, potentially, hole) seen in the Milky Way's nuclear star cluster has a radius of at least 0.5 pc. At the distance of M31, this is equivalent to a core radius of $0\farcs13$ on the sky, which is larger than that observed here ($< 0\farcs1$). Future modeling efforts will aim to better model the size of the central hole in the stellar distribution in the NIR.

Previous high spatial resolution kinematics for this system were obtained using long-slit spectroscopy with HST. We find a similar kinematic structure to that seen in the STIS long-slit measurements from B05, though we note some discrepancies with our data, which may be attributable to different bulge subtraction methods. The previous highest spatial resolution kinematics with full 2D FOV coverage were limited by early generation AO correction and the resolution obtained, a factor of 4 poorer than that of the OSIRIS observations presented here, was a small improvement over seeing-limited observations. Comparison of the OASIS data from B01 with our OSIRIS kinematics, smoothed to their resolution, shows some discrepancies in alignment of the profiles, which may be attributable to differing SMBH positions. In addition, the dispersion peak reported by OASIS is much higher than that in our smoothed data; differing bulge subtraction methods may be the culprit. The results presented here show the value of the combination of the power of full 2D kinematic mapping with high spatial resolution and will be valuable for future modeling.

3.7 CONCLUSION

We present high-resolution, 2D kinematic maps of the nucleus of M31, enabling us to measure the orientation and precession rate of the eccentric disk of old stars. In comparison with previous HST optical images, the infrared data presented here shows no signs of a central star cluster and rather shows a hole in the infrared light at the black hole position. The 2D kinematics are largely in agreement with previous long-slit kinematic measurements. However, the new NIR flux maps favor a different orientation for the eccentric nuclear disk than the previous best-fit model fitted to optical data of Peiris & Tremaine (2003). The best-

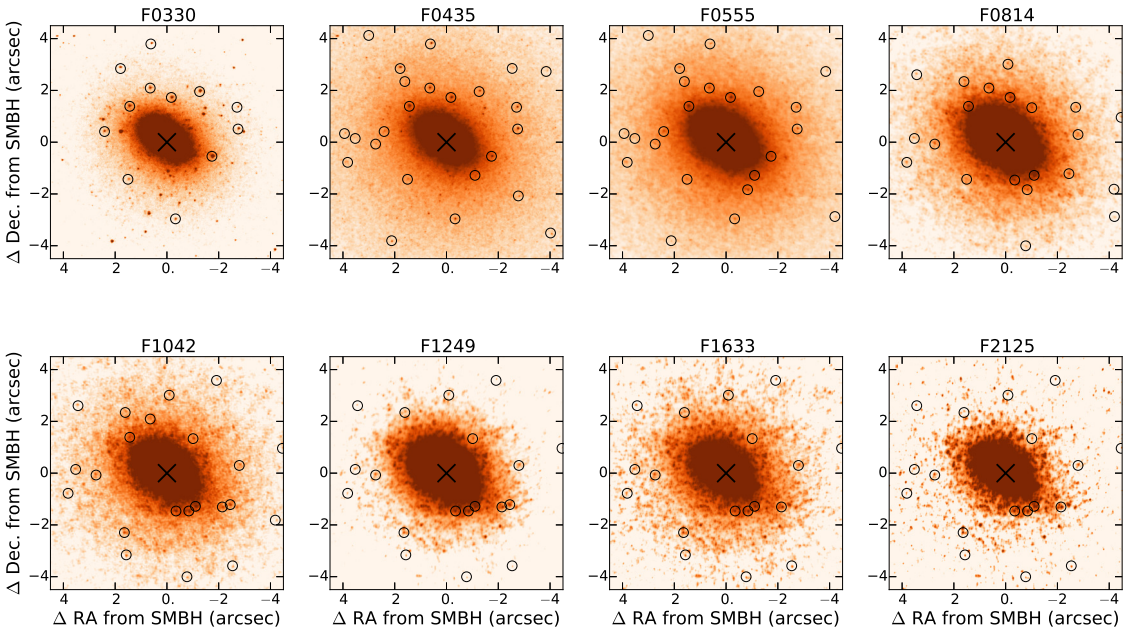

Figure 3.28 Images are aligned as in § 3.3.4, and are shown scaled to match the F330W frame (pixel scale of 0.025″ pixel^{-1}). The position of the SMBH is marked with the black cross and is accurate to 0.033″ in the F2125 frame. The color scaling has been chosen to emphasize the faint outer region and the compact sources used for alignment. The alignment sources are circled in black.

fit orientation for the morphology seen in the NIR is $[\theta_l, \theta_i, \theta_a] = [-32.8° \pm 3.5°, 44.1° \pm 1.8°, -14.5° \pm 14.6°]$, or offset from the best-fit model from Peiris & Tremaine (2003) by [10°, −10°, 20°].

We also present a measurement of the precession rate for the eccentric disk of 0.0±3.4 km s^{-1} pc^{-1}. This slow precession rate favors the scenario put forth by Chang et al. (2007) suggesting that stellar winds from the AGB and red giant stars in the old eccentric disk provide the fuel for the starburst that produced the young nuclear cluster.

3.8 Appendix A

P3, the compact young cluster assumed to be coincident with M31's SMBH, is bright in the UV but dark in the NIR. Locating the SMBH in the OSIRIS data thus requires registering

the UV and the NIR images. However, as there are essentially no compact sources bright in both bandpasses, we instead register pairs of frames adjacent in wavelength. We step through a total of 8 frames, starting in the UV and ending in the NIR $K'-$band. The alignment sources used are circled in Fig. 3.28. The position of P3 is marked with a black cross, but as the color scaling is set to emphasize the fainter alignment sources, the inner nuclear disk structure is not visible in this figure.

3.9 Appendix B

The precession of the eccentric disk is found using the method from Tremaine & Weinberg (1984), which only requires a one-dimensional slice in both surface brightness and line-of-sight velocity. We show in §**??** that this produces a value for the precession, $\Omega_P = 63.0 \pm 5.3$ km s^{-1} pc^{-1}, that is higher than that derived from the two-dimensional model fitting. The goodness-of-fit is not improved for this value of the precession. Figures 3.29 and 3.30 show the OSIRIS kinematic maps compared to the models derived using the best-fit orientation and the precession from the TW method. While the flux and dispersion residuals are small, the velocity residuals are much higher than for the best-fit precession value of 0 km s^{-1} pc^{-1}.

3.10 Appendix C

Lauer et al. (1998) observed the nuclear eccentric disk in M31 with HST/WFPC2 in the F300W, F555W, and F814W filters. We show the F555W image in Fig. 3.31 (top panel). PT03 used this photometry, in combination with spectroscopy from KB99, to fit the orientation of their models. Their best-fit models to the data are not aligned with the larger-scale galactic disk of M31 and are designated as the nonaligned models (Table 3.4). Figure 3.31 shows the nonaligned models and the residuals between the F555W photometry and these models. Comparison of this figure with Fig. **??** shows that while the nonaligned

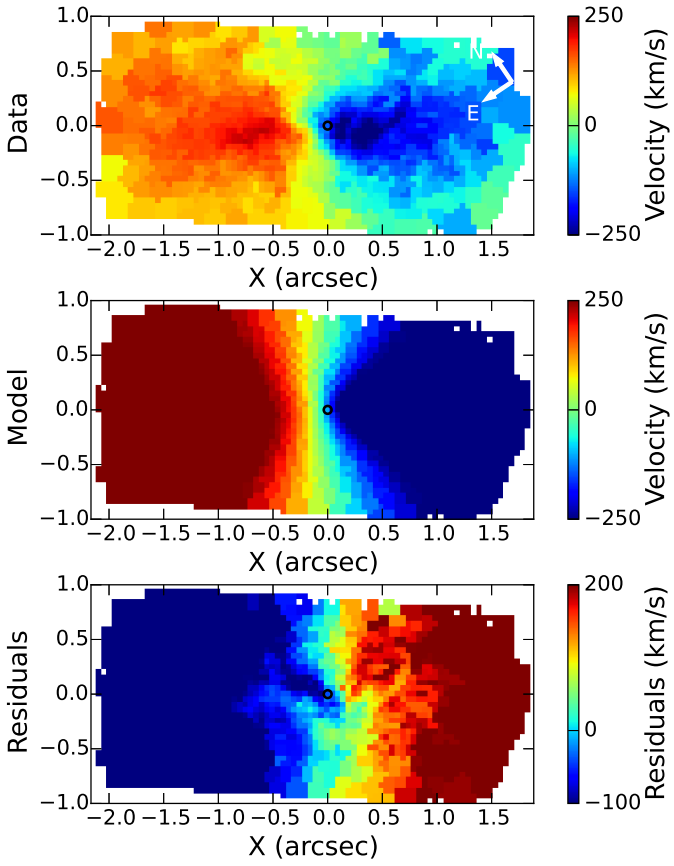

Figure 3.29 Comparison of OSIRIS data with the models suggested by the TW method. The orientation is the same as for our best-fit models, but the precession was derived using the TW method and calibrated using models with known precessions. While the dispersion residuals are small, the velocity residuals are much higher than in with our best-fit precession value of 0 km s^{-1} pc^{-1}. The flux residuals are unchanged by the high precession and are identical to those in Fig. 3.20.

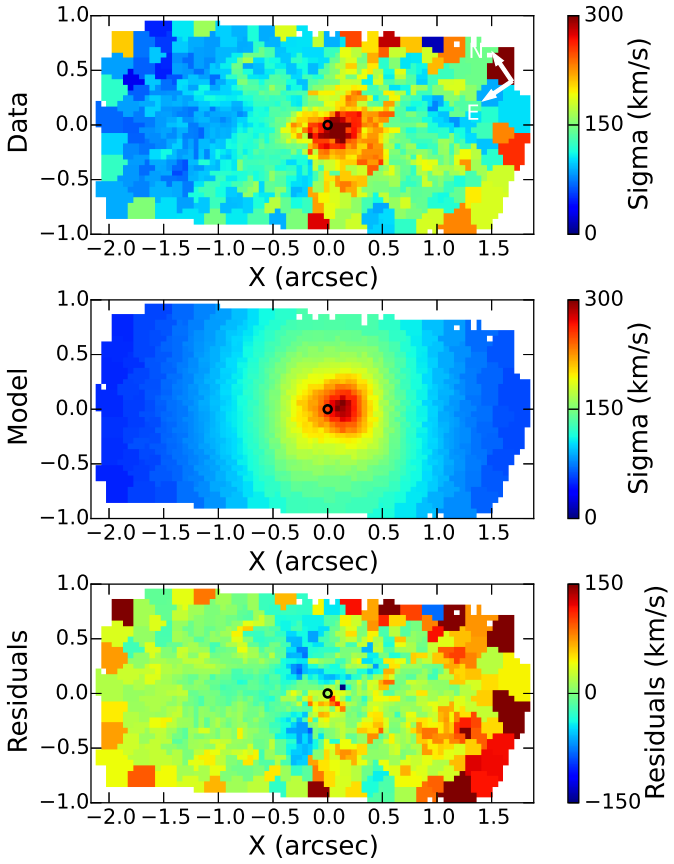

Figure 3.30 Similar to Fig. 3.29 but for the dispersion.

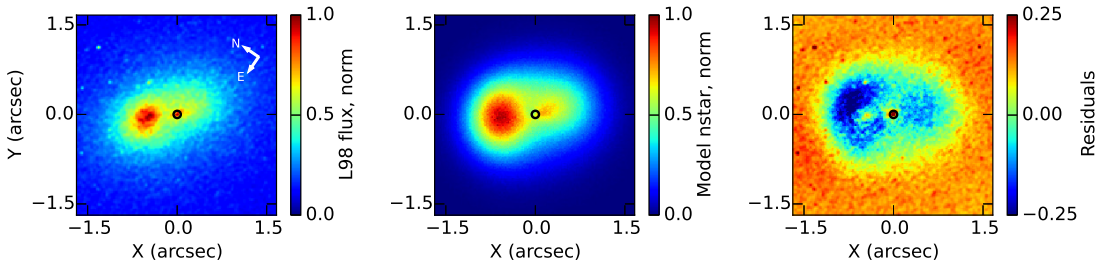

Figure 3.31 Comparison of F555W flux map from Lauer et al. (1998) with the nonaligned models from PT03. These photometric data were used for the fitting of the original models. In all, the SMBH position is marked with the black circle, and the PA = 55.7°, the original PA from Lauer et al. (1998) (note that this PA differs from that of the OSIRIS figures). *Top:* F555W flux map, scaled so the peak flux is equal to 1. *Middle:* Modeled number of stars per spatial bin, binned to the subsampled F555W pixel scale of $0\farcs0228$ pix^{-1}. The models are oriented using the nonaligned orientation from PT03 (angles given in Table 3.4) and scaled so the peak is equal to 1. *Bottom:* Residuals, data minus models.

models are a good fit to the F555W photometry, they are not a good fit to the OSIRIS NIR photometry.

We would like to thank Shelley Wright for help with OSIRIS observations, and the OSIRIS Pipeline Working Group for their work on the OSIRIS data reduction pipeline and discussions on its improvement. We also thank Tod Lauer for sharing HST images. We thank Scott Tremaine for his helpful comments on the manuscript. HVP was partially supported by the European Research Council (ERC) under the European Community's Seventh Framework Programme (FP7/2007-2013)/ERC grant agreement number 306478-CosmicDawn. RMR acknowledges support from NSF AST-121095, 13755, and 1518271. AMG was supported by NSF AST-1412615. NSO/Kitt Peak FTS data used here were produced by NSF/NOAO. This research has made use of NASA's Astrophysics Data System. Based on observations made with the NASA/ESA Hubble Space Telescope, and obtained from the Hubble Legacy Archive, which is a collaboration between the Space Telescope Science Institute (STScI/NASA), the Space Telescope European Coordinating Facility (ST-ECF/ESA) and the Canadian Astronomy Data Centre (CADC/NRC/CSA). This research has made use of the Keck Observatory Archive (KOA), which is operated by the W. M. Keck

Observatory and the NASA Exoplanet Science Institute (NExScI), under contract with the National Aeronautics and Space Administration. The data presented herein were obtained at the W.M. Keck Observatory, which is operated as a scientific partnership among the California Institute of Technology, the University of California and the National Aeronautics and Space Administration. The Observatory was made possible by the generous financial support of the W.M. Keck Foundation. The authors wish to recognize and acknowledge the very significant cultural role and reverence that the summit of Mauna Kea has always had within the indigenous Hawaiian community. We are most fortunate to have the opportunity to conduct observations from this mountain.

References

Allen, D. A., Hyland, A. R., & Hillier, D. J. 1990, MNRAS, 244, 706

Bacon, R., Emsellem, E., Combes, F., Copin, Y., Monnet, G., & Martin, P. 2001, A&A, 371, 409

Battistini, P. L., Bonoli, F., Casavecchia, M., Ciotti, L., Federici, L., & Fusi-Pecci, F. 1993, A&A, 272, 77

Bender, R., Kormendy, J., Bower, G., Green, R., Thomas, J., Danks, A. C., Gull, T., Hutchings, J. B., Joseph, C. L., Kaiser, M. E., Lauer, T. R., Nelson, C. H., Richstone, D., Weistrop, D., & Woodgate, B. 2005, ApJ, 631, 280

Brown, C. K. & Magorrian, J. 2013, MNRAS, 431, 80

Cappellari, M. & Copin, Y. 2003, MNRAS, 342, 345

Cappellari, M. & Emsellem, E. 2004, PASP, 116, 138

Chang, P., Murray-Clay, R., Chiang, E., & Quataert, E. 2007, ApJ, 668, 236

Courteau, S., Widrow, L. M., McDonald, M., Guhathakurta, P., Gilbert, K. M., Zhu, Y., Beaton, R. L., & Majewski, S. R. 2011, ApJ, 739, 20

Do, T., Martinez, G. D., Yelda, S., Ghez, A., Bullock, J., Kaplinghat, M., Lu, J. R., Peter, A. H. G., & Phifer, K. 2013, ApJ, 779, L6

Dorman, C. E., Widrow, L. M., Guhathakurta, P., Seth, A. C., Foreman-Mackey, D., Bell, E. F., Dalcanton, J. J., Gilbert, K. M., Skillman, E. D., & Williams, B. F. 2013, ApJ, 779, 103

Galleti, S., Bellazzini, M., Federici, L., Buzzoni, A., & Fusi Pecci, F. 2007, A&A, 471, 127

Genzel, R., Crawford, M. K., Townes, C. H., & Watson, D. M. 1985, ApJ, 297, 766

Goodman, J. 2003, MNRAS, 339, 937

Hanson, M. M., Conti, P. S., & Rieke, M. J. 1996, ApJS, 107, 281

Hopkins, P. F. & Quataert, E. 2010, MNRAS, 405, L41

Jacobs, V. & Sellwood, J. A. 2001, ApJ, 555, L25

Kausch, W., Noll, S., Smette, A., Kimeswenger, S., Barden, M., Szyszka, C., Jones, A. M., Sana, H., Horst, H., & Kerber, F. 2015, A&A, 576, A78

Kazandjian, M. V. & Touma, J. R. 2013, MNRAS, 430, 2732

Kolykhalov, P. I. & Syunyaev, R. A. 1980, Soviet Astronomy Letters, 6, 357

Kormendy, J. & Bender, R. 1999, ApJ, 522, 772

Krabbe, A., Gasaway, T., Song, I., Iserlohe, C., Weiss, J., Larkin, J. E., Barczys, M., & Lafreniere, D. 2004, in Proc. SPIE, Vol. 5492, Ground-based Instrumentation for Astronomy, ed. A. F. M. Moorwood & M. Iye, 1403–1410

Larkin, J., Barczys, M., Krabbe, A., Adkins, S., Aliado, T., Amico, P., Brims, G., Campbell, R., Canfield, J., Gasaway, T., Honey, A., Iserlohe, C., Johnson, C., Kress, E., LaFreniere, D., Lyke, J., Magnone, K., Magnone, N., McElwain, M., Moon, J., Quirrenbach, A., Skulason, G., Song, I., Spencer, M., Weiss, J., & Wright, S. 2006, in Proc. SPIE, Vol. 6269, Society of Photo-Optical Instrumentation Engineers (SPIE) Conference Series, 62691A

Lauer, T. R., Bender, R., Kormendy, J., Rosenfield, P., & Green, R. F. 2012, ApJ, 745, 121

Lauer, T. R., Faber, S. M., Ajhar, E. A., Grillmair, C. J., & Scowen, P. A. 1998, AJ, 116, 2263

Lauer, T. R., Faber, S. M., Groth, E. J., Shaya, E. J., Campbell, B., Code, A., Currie, D. G., Baum, W. A., Ewald, S. P., Hester, J. J., Holtzman, J. A., Kristian, J., Light, R. M., Ligynds, C. R., O'Neil, Jr., E. J., & Westphal, J. A. 1993, AJ, 106, 1436

Levin, Y. & Beloborodov, A. M. 2003, ApJ, 590, L33

Livingston, W. & Wallace, L. 1991, An atlas of the solar spectrum in the infrared from 1850 to 9000 cm-1 (1.1 to 5.4 micrometer)

Lu, J. R., Ghez, A. M., Hornstein, S. D., Morris, M. R., Becklin, E. E., & Matthews, K. 2009, ApJ, 690, 1463

Maiolino, R., Rieke, G. H., & Rieke, M. J. 1996, AJ, 111, 537

McConnachie, A. W., Irwin, M. J., Ferguson, A. M. N., Ibata, R. A., Lewis, G. F., & Tanvir, N. 2005, MNRAS, 356, 979

McConnell, N. J., Lu, J. R., & Mann, A. W. 2015, ArXiv e-prints

Melchior, A.-L. & Combes, F. 2013, A&A, 549, A27

Menezes, R. B., Steiner, J. E., & Ricci, T. V. 2013, ApJ, 762, L29

Morris, M. 1993, ApJ, 408, 496

Nieten, C., Neininger, N., Guélin, M., Ungerechts, H., Lucas, R., Berkhuijsen, E. M., Beck, R., & Wielebinski, R. 2006, A&A, 453, 459

Olsen, K. A. G., Blum, R. D., Stephens, A. W., Davidge, T. J., Massey, P., Strom, S. E., & Rigaut, F. 2006, AJ, 132, 271

Paumard, T., Genzel, R., Martins, F., Nayakshin, S., Beloborodov, A. M., Levin, Y., Trippe, S., Eisenhauer, F., Ott, T., Gillessen, S., Abuter, R., Cuadra, J., Alexander, T., & Sternberg, A. 2006, ApJ, 643, 1011

Peiris, H. V. & Tremaine, S. 2003, ApJ, 599, 237

Rich, R. M., Mighell, K. J., Freedman, W. L., & Neill, J. D. 1996, AJ, 111, 768

Rossa, J., van der Marel, R. P., Böker, T., Gerssen, J., Ho, L. C., Rix, H.-W., Shields, J. C., & Walcher, C.-J. 2006, AJ, 132, 1074

Saglia, R. P., Fabricius, M., Bender, R., Montalto, M., Lee, C.-H., Riffeser, A., Seitz, S., Morganti, L., Gerhard, O., & Hopp, U. 2010, A&A, 509, A61

Salow, R. M. & Statler, T. S. 2001, ApJ, 551, L49

—. 2004, ApJ, 611, 245

Sambhus, N. & Sridhar, S. 2000, ApJ, 539, L17

—. 2002, A&A, 388, 766

Sanders, R. H. 1992, Nature, 359, 131

Seth, A. C., Dalcanton, J. J., Hodge, P. W., & Debattista, V. P. 2006, AJ, 132, 2539

Smette, A., Sana, H., Noll, S., Horst, H., Kausch, W., Kimeswenger, S., Barden, M., Szyszka, C., Jones, A. M., Gallenne, A., Vinther, J., Ballester, P., & Taylor, J. 2015, A&A, 576, A77

Sofue, Y. & Yoshida, S. 1993, ApJ, 417, L63+

Statler, T. S., King, I. R., Crane, P., & Jedrzejewski, R. I. 1999, AJ, 117, 894

Tremaine, S. 1995, AJ, 110, 628

Tremaine, S. & Weinberg, M. D. 1984, ApJ, 282, L5

van Dam, M. A., Bouchez, A. H., Le Mignant, D., Johansson, E. M., Wizinowich, P. L., Campbell, R. D., Chin, J. C. Y., Hartman, S. K., Lafon, R. E., Stomski, Jr., P. J., & Summers, D. M. 2006, PASP, 118, 310

van der Marel, R. P. & Franx, M. 1993, ApJ, 407, 525

Winge, C., Riffel, R. A., & Storchi-Bergmann, T. 2009, ApJS, 185, 186

Wizinowich, P. L., Le Mignant, D., Bouchez, A. H., Campbell, R. D., Chin, J. C. Y., Contos, A. R., van Dam, M. A., Hartman, S. K., Johansson, E. M., Lafon, R. E., Lewis, H., Stomski, P. J., Summers, D. M., Brown, C. G., Danforth, P. M., Max, C. E., & Pennington, D. M. 2006, PASP, 118, 297

Yelda, S., Ghez, A. M., Lu, J. R., Do, T., Meyer, L., Morris, M. R., & Matthews, K. 2014, ApJ, 783, 131

Chapter 4

Characterizing and Improving the Data Reduction Pipeline for the OSIRIS Integral-Field Spectrograph

Note: This chapter will be submitted for publication by the end of the summer, with co-authors Tuan Do, James E. Larkin, Anna Boehle, Randy D. Campbell, Samantha Chappell, Devin Chu, Anna Ciurlo, Maren Cosens, Michael P. Fitzgerald, Andrea Ghez, Jessica R. Lu, Jim E. Lyke, Etsuko Mieda, Alexander R. Rudy, Andrey Vayner, Gregory Walth, and Shelley A. Wright.

Abstract

OSIRIS is a near-infrared (1.0–2.4 μm) integral field spectrograph operating behind the adaptive optics system at Keck Observatory. Since its commissioning in 2005, it has been a productive instrument, producing nearly half the laser guide star adaptive optics (LGS AO) papers on Keck. The complexity of its raw data format necessitated a custom data reduction pipeline (DRP) delivered with the instrument in order to iteratively assign flux in overlapping spectra to the proper spatial pixel or spaxel. Other than bug fixes and updates required for hardware upgrades, the bulk of the DRP has not been updated since initial instrument commissioning. We report on efforts to characterize and improve the DRP including improvements to the rectification matrix calibration files, characterization of the

flux assignment algorithm, and exploration of spatial rippling in the reduced data cubes. We also present lessons learned that are relevant to the next generation of integral-field spectrographs.

4.1 INTRODUCTION

The OSIRIS (OH Suppressing InfraRed Imaging Spectrograph; Larkin et al. 2006) instrument behind the Adaptive Optics (AO) system at the W. M. Keck Observatory has proven to be a revolutionary tool for extragalactic, Galactic, and solar system observational astrophysics. OSIRIS has produced nearly one-half of the laser guide star (LGS) AO publications from Keck since its commissioning in 2005, including the majority of the extragalactic LGS papers. Results from OSIRIS observations span fields from planetary science (e.g., Laver & de Pater (2009), Laver et al. (2009), Brown & Hand (2013)), some of the first spectroscopic characterization of extrasolar planets (e.g., Bowler et al. (2010), Barman et al. (2011), Konopacky et al. (2013)), studies of crowded fields such as the center of the Milky Way galaxy (e.g., Do et al. (2013), Lu et al. (2013), Yelda et al. (2014)), measurement of the masses of supermassive black holes (SMBHs) in nearby galaxies (e.g., McConnell et al. (2011), Medling et al. (2011), Walsh et al. (2012)), and studies of high redshift (1 ¡ z ¡ 3) galaxies (e.g., Wright et al. (2007), Stark et al. (2008), Law et al. (2009), Jones et al. (2010)).

OSIRIS is a pathfinder among near-infrared (NIR) integral field spectrographs (IFS) due to its unique use of a lenslet array to split the field into spaxels while preserving the high Strehl ratio point spread function (PSF) of the Keck AO system. The new planet finding spectrographs (e.g., Gemini Planet Imager, SPHERE) have a similar configuration but with a very different output data format. The OSIRIS IFS was designed to have very stable spectra that always fall at the exact same position on the detector, using a single, fixed grating and no moving components after the lenslet array. In order to maximize the field of view, the spectra from adjacent spaxels are only separated by 2 pixels and overlap

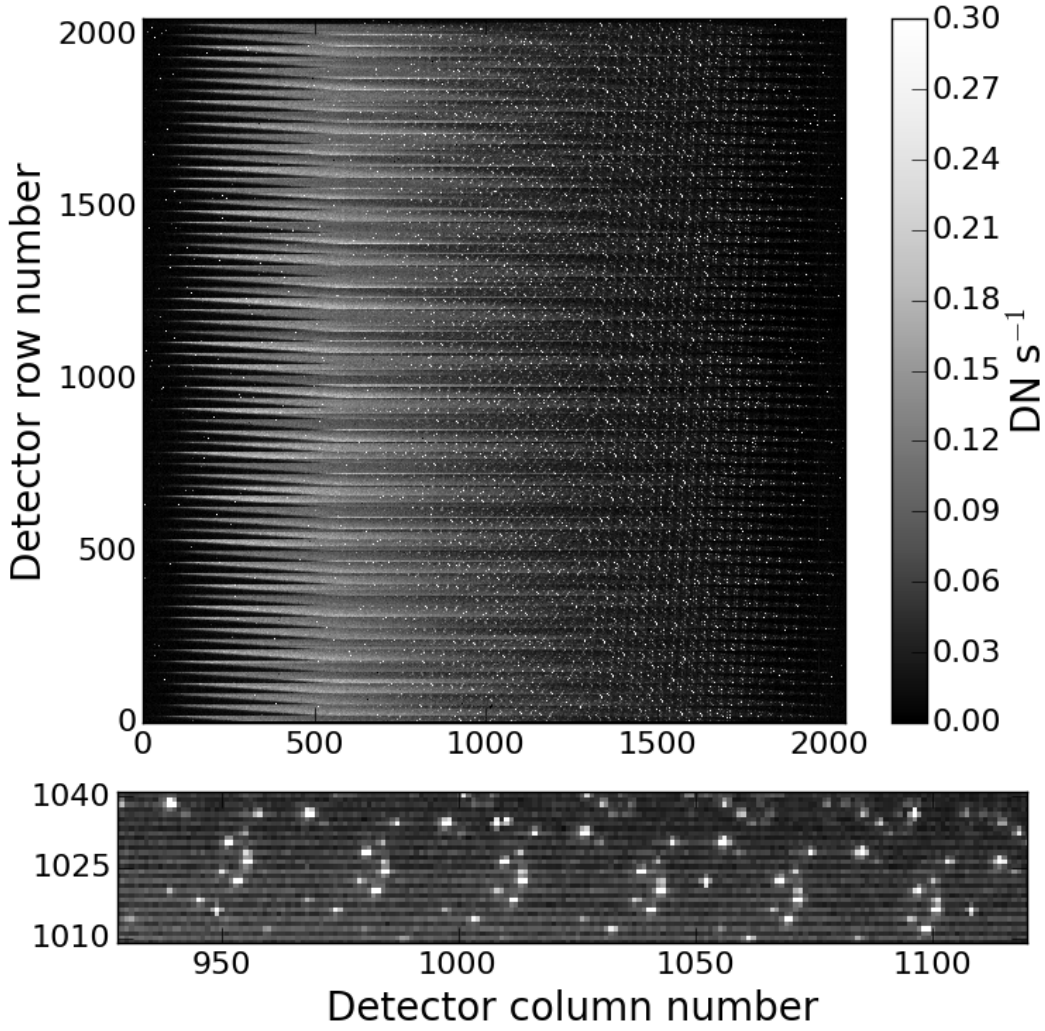

Figure 4.1 The OSIRIS spectra are closely packed on the detector. *Top:* Raw detector image of a Kbb/35 sky frame. Individual spots are OH sky lines. The wavelength direction increases to the left; the bright bands at the left are the rising thermal background in the red. *Bottom:* Zoom in of the panel above. Individual gray rows, alternating with the darker background, represent the thermal continuum in individual sky spaxels. Bright spots are OH sky lines. Neighboring spectra are staggered by 32 detector columns, which translates to a stagger of 32 spectral channels in the reduced cube.

(see figure 4.1). However, the stable format enables the use of a deconvolution process to separate the raw, interleaved spectra and to assign flux to each spaxel at every wavelength. The output is a data cube of dimensions (x, y, lambda). OSIRIS uses a combination of four spatial samplings $0\farcs02$ to $0\farcs1$ per spaxel with 19 filters that generates up to 76 modes that need to be characterized and calibrated. The calibration files are then used in the OSIRIS data reduction pipeline to assign the correct amount of flux from adjacent pixels to each spectrum. The DRP is essential for both real-time processing at the telescope and for post-processing of all data.

4.1.1 The OSIRIS data reduction pipeline

The complexity of the raw data output from the instrument necessitated a well-developed data reduction pipeline from delivery (DRP, Krabbe et al. 2002), the first for an instrument on Keck. The DRP, written primarily in IDL with computationally intensive processes passed into C, is modularized, such that individual modules of the reduction can be turned on or off as needed at runtime. Typical reduction modules, such as dark subtraction, cosmic ray removal, and telluric correction, are available. The DRP also includes an implementation of the scaled sky subtraction algorithm detailed by Davies (2007).

However, the most unique part of the DRP is the spatial rectification module (`spatrectif`), which performs a deconvolution the utilizing the Gauss-Seidel method to iteratively assign flux from the raw detector image to individual spatial pixels (spaxels, Krabbe et al. 2004).

The OSIRIS spectral format allocates only 2 pixels between neighboring spectra and there is a stagger in wavelength of about 32 pixels between lenslet neighbors. While the PSF of each lenslet in the spatial direction, perpendicular to the dispersion direction, is currently below 2 pixels in FWHM, this has not always been true, and in all cases some blending occurs which must be extracted with the deconvolution. The current procedure involves using the empirically determined rectification matrices (§4.2.4) to iteratively assign flux from pixels from the 2D detector image to the 3D cube. In addition to mapping the

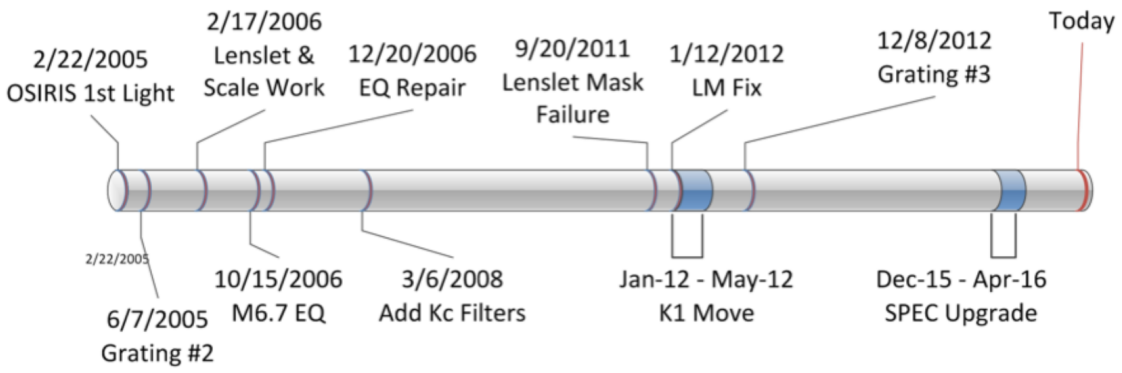

Figure 4.2 Timeline of OSIRIS hardware changes and upgrades since first light.

lenslet response as a function of spatial pixel and wavelength, the rectification matrices also serve as flat fields to determine the detector pixel response.

To run the pipeline, the user designates which modules will be used, along with setting any module-specific options or keywords, in an XML file. This XML file is saved to a queue folder that is regularly checked by the DRP. The DRP then processes any new XML files and saves the output as requested.

4.1.2 Hardware upgrades

OSIRIS has been operational on Keck for over a decade. Over the course of that that time, it's been subject to repairs and upgrades which are summarized in figure 4.2. Two major hardware upgrades have occurred in recent years.

In December 2012, the dispersion grating was upgraded (Mieda et al. 2014), increasing the grating efficiency and flux on the raw detector by a nearly a factor of 2. At the same time, OSIRIS was moved from Keck-II to Keck-I, to take advantage of Keck-I's new laser guide star (LGS) AO system. At this time, the DRP was updated to include an updated wavelength solution, to account for the different image orientation, to update the world coordinate system (WCS), and to account for differential dichroic dispersion between Keck-II and Keck-I.

In January 2016, the detector behind the spectrograph portion of OSIRIS was upgraded from a Hawaii-2 detector to a Hawaii-2RG (Boehle et al. 2016). The new detector shows a lower dark current and improved throughput by up to a factor of 2 in raw detector frames. The DRP was updated with a new wavelength solution, revised locations of the spectra on the raw detector, and the removal of glitch modules only needed for the old Hawaii-2 detector.

4.1.3 Motivation

However, while the 2012 OSIRIS move to Keck I and grating upgrade increased throughput in the the raw data, this improvement was not fully translated to the reduced data cubes. While the raw detector frames saw an increase of a factor of 2 in S/N, a limited increase was observed in the reduced cubes, potentially indicating an issue with the DRP. At roughly the same time of the OSIRIS move and upgrade, observers noticed that reduced science data of QSO observations incorrectly showed dark spaxels near the central bright compact source. In addition, many observers had noticed unphysically large positive and negative spikes at a few wavelength channels in a small number of spaxels in their reduced data. Finally, single channel maps of OH sky lines or other evenly illuminated sources were no longer flat, but instead displayed a rippling pattern unrelated to incident illumination. These issues led to an effort to better characterize the behavior of the DRP and to improve the quality of the reduced data.

Since initial delivery, the DRP has historically been maintained by Keck, with coding and testing performed by volunteered time from a few instrument team members. Upgrades to the software have primarily occurred after hardware upgrades that necessitated changes to the wavelength calibration, for instance. However, the scope of the necessary DRP characterization to resolve these issue was beyond the scope of usual DRP maintenance, and the OSIRIS Pipeline Working Group was formed. We detail our efforts in the following report. We outline the data we used for this work in § 4.2, improvements to the calibration files in § 4.3, artifacts from the flux assignment algorithm in § 4.4, and spatial rippling

Table 4.1. Keck OSIRIS Observations

Observation Type	Date (UT)	Exposure Time (s)	Filter	Plate Scale) (mas)
arc	2015 Dec 17	32	Kbb	50
arc	2016 Mar 18	60	Jbb	50
arc[a]	2016 Sep 02	30	Kbb	35
arc[a]	2016 Sep 02	30	Kbb	50
QSO	2014 May 19	4x600	Hn3	100
QSO	2015 Aug 09	7x600	Kn1	100
sky	2013 May 11	900	Kbb	35
sky	2014 May 17	900	Kbb	50
sky	2016 May 14	900	Kbb	35
sky	2016 Jul 11	900	Kbb	35
white light[a]	2015 Sep 04	8	Kbb	50

[a]Single column of lenslets illuminated

in § 4.5. Many of the issues and improvements we outline here are relevant to the future generation of IFSs on the next generation of telescopes; we outline our recommendations in § 4.6.

4.2 DATA

Throughout this paper, we will use several on-sky science and engineering data sets to investigate the OSIRIS spectral extraction routine and performance. These data sets are described below and summarized in Table 4.1.

4.2.1 Example Science Data Sets

Bright quasars and their host galaxies are a particularly useful data set for testing the DRP as they contain an extremely compact (<2 spaxels), bright point-like quasar with both continuum and strong emission lines, and underlying faint galaxy emission (<1 arcsecond). A clean spectral extraction and high quality AO performance is needed for these data sets,

since the science objective is to resolve the host galaxies of high-redshift (z>1) quasars (Vayner et al. 2016).

On 2014 May 19 and 2015 August 9 OSIRIS observations were taken of the quasars 3C 298 and 3C 9 using the 100mas plate scale with the Hn3 (λ_{cen}=1.64 μm) and Kn1 (λ_{cen}=2.01 μm) filters, respectively. The laser guide star AO (LGS-AO) system was used for both. For 3C 298 there was a total of four 600 second frames with on-chip dithering, while for 3C 9, there was a total of seven 600 second frames with on-chip dithering. Separate sky frames were acquired during both observations.

Initial data reduction in 2014 indicated potential issues with the DRP. The combination of the bright continuum source with strong emission lines made identification of spatial and spectral flux assignment artifacts easy. We further describe the QSO DRP results in Section 4.4.1 using these two quasars: 3C 298 (z=1.439; R=16.0 mag; H=14.5 mag) and 3C 9 (z=2.012; R=17.4 mag; H=15.6 mag).

4.2.2 Skies

NIR sky spectra are useful for testing DRP effects on emission line spectra due to the abundance of narrow OH sky lines. In addition to the OH emission lines, the sky spectrum exhibits a thermal background continuum, increasing in the K-band. Sky observations are frequently taken during the normal course of observing; however, several dedicated "deep skies" were taken in order to maximize the signal-to-noise.

4.2.3 Arc lamps

Calibration frames using Ar, Kr, and Xe arc lamps were obtained. Emission lines were identified using a NIR line list[1]. Arc lamp spectra are useful as a calibration source due to their high S/N emission lines, narrow line widths, and well-constrained wavelengths.

Arc lamp spectra were obtained in two ways: first, with the entire lenslet array illuminated, as for most science exposures. In addition, arc lamp spectra were observed

[1]http://www2.keck.hawaii.edu/inst/nirspec/lines.html

using a single lenslet column mask. This mask consists of a slit wide enough to illuminate only one column of lenslets, which corresponds to one illuminated column of spaxels in the reduced data cube. On the detector, this produces spectra that are well-separated (i.e. separated by many times the FWHM of each spectrum) and thus flux on the detector can be assigned unambiguously to a single spaxel. The resulting data cube is expected to contain a single column of spaxels with full arc spectra, while the unilluminated lenslets correspond to dark spaxels with no spectra.

4.2.4 Rectification Matrices

Flux on the detector is assigned to a spaxel in the data cube using an empirically determined matrix, the rectification matrix, of lenslet response curves. White light exposures are taken through the single lenslet column mask without the dispersion grating in place. The mask is stepped across the lenslet array, illuminating one column of lenslets at a time. The resulting frames display well-separated white light bands with no emission lines (see figure 4.3 for a single example scan).

As the illumination source is uniform and the light is not dispersed, the resulting flux on the detector is a function of lenslet response and pixel response only. These response curves are measured and encoded in the resulting rectification matrix.

The rectification matrix file contains three extensions. The first extension is the y position (lower and upper bounds) of each spectrum on the detector, numbered in descending order from the top of the detector. The second extension is a quality flag. The spectra from some edge spaxels do not fall completely on the detector and thus are excluded from the final data cube; these are marked with a 0 in this extension. The third extension is the three-dimensional matrix containing the lenslet response curves. The first dimension is the width of the detector along the dispersion direction (2048 pixels), the second is the extent of the vertical response of each lenslet on the detector (16 pixels), and the third is the spectrum number (dependent on the mode selected). The lenslet response curves for the spectra flagged in the second extension are set to zero here.

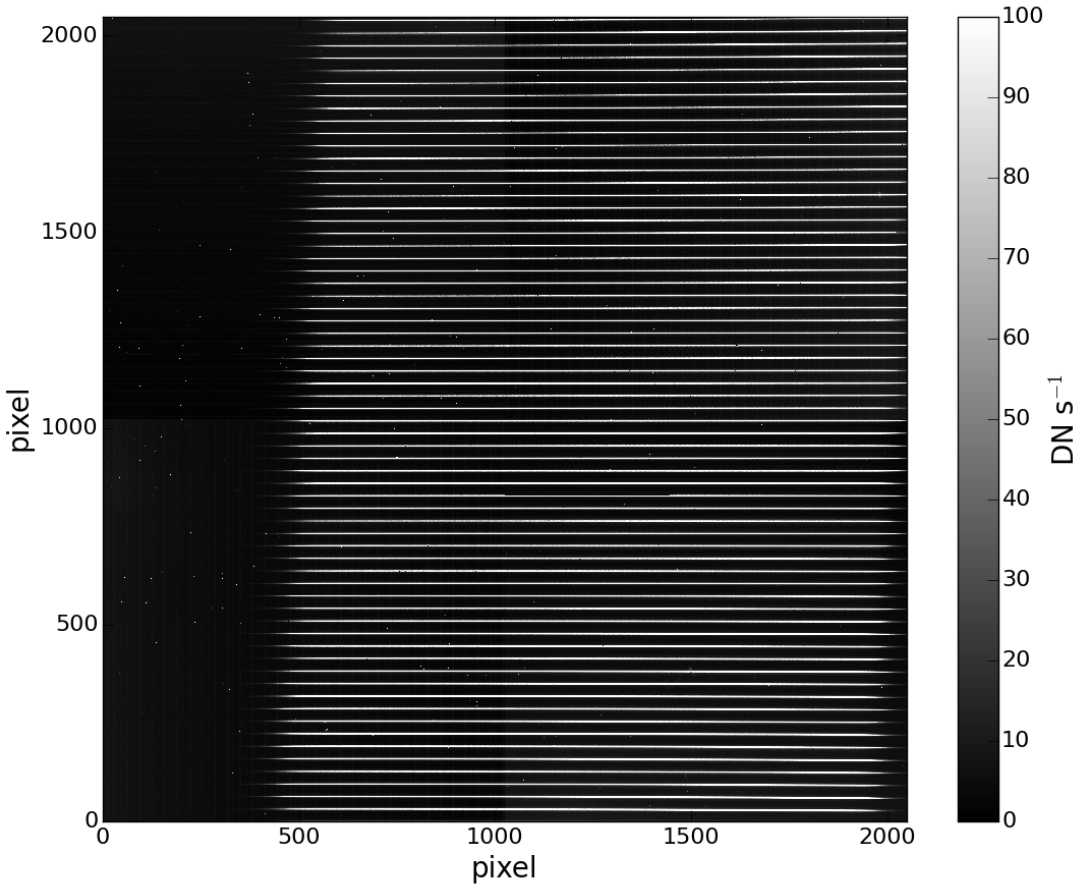

Figure 4.3 Example white light scan, used to create a rectification matrix. Only one column of lenslets is illuminated. This produces well-separated traces and is used to determine the lenslet response curves. The x direction corresponds to the dispersion direction when the grating is in place.

4.3 COSMIC RAYS IN THE RECTIFICATION MATRICES

The publicly available rectification matrices suffer from inadequate cosmic ray removal in the corresponding white light scans, which results in large flux spikes in the final reduced data cubes (figure 4.4, bottom panel). These spikes occur in just a few spectral channels in a few spaxels, but display flux values up to 10^8 DN s^{-1} (both positively and negatively signed), while the maximum real flux in a single spectral channel in one spaxel of a 900 s sky frame is on the order of 1 DN s^{-1}. In addition, the saturation limit of the detector is 33,000 DN (pre-2016) or 65,535 DN (2016–present), so such high counts are unphysical.

Prior to 2015, the rectification matrices were created using a single white light scan at each position of the lenslet column mask. To remedy the inadequate cosmic ray removal, new rectification matrices were created in 2015 using a set of three white light scans at each lenslet column position. The scans at each lenslet column position are medianed together to more robustly remove cosmic rays (Randy Campbell, private communication). The matrix made with the medianed scans produces a data cube that is free from unphysical spikes. Rectification matrices using the median method were created for each OSIRIS mode in 2015, covering the period between December 2012 and December 2015, and are publicly available on the OSIRIS instrument website[2]. All new rectification matrices, including for the period beginning in January 2016, are created using this median scan method.

New white light scans and new rectification matrices are created each time the instrument is modified and are unique to its physical setup. Therefore, data taken prior to the physical configuration beginning in December 2012, when this issue was discovered, must be reduced using a rectification matrix that still suffers from cosmic ray effects. However, the rectification matrix itself is simply a three-dimensional array and any cosmic rays are easily identified and interpolated over.

[2]http://tkserver.keck.hawaii.edu/osiris/

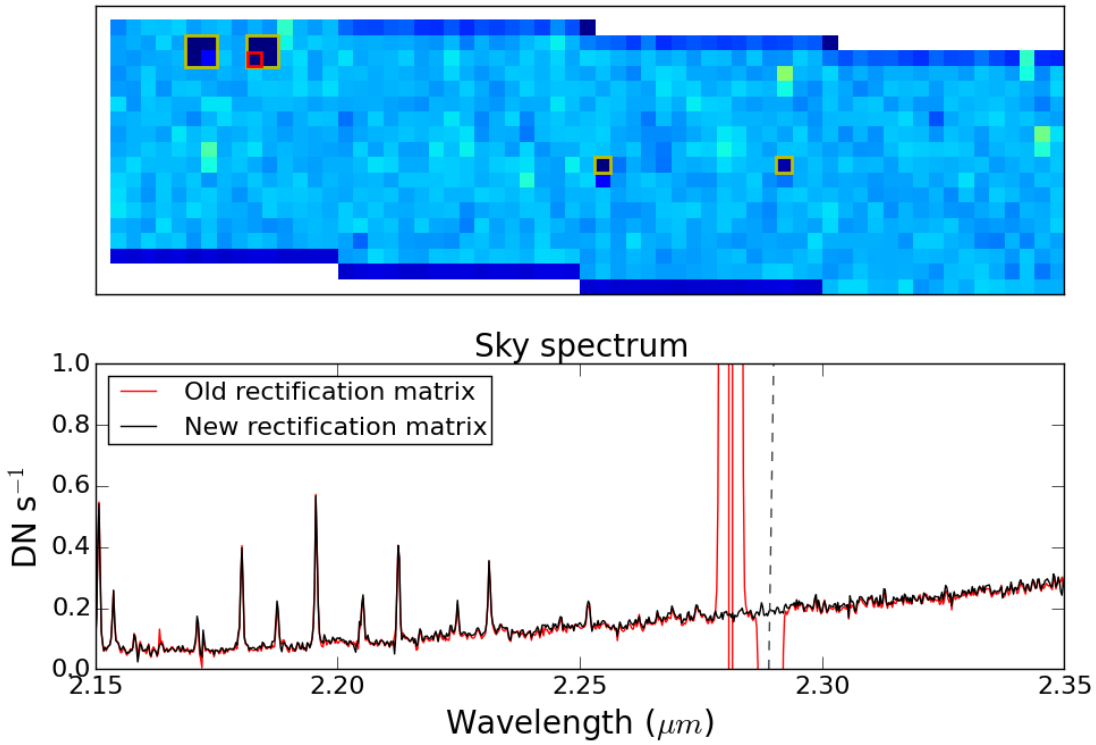

Figure 4.4 Old rectification matrices did not properly account for cosmic rays; these led to artifacts in the reduced data cubes. These artifacts can be seen here in a reduced sky cube. *Top:* Channel map (single wavelength slice) from a reduced sky cube. The spaxel shown in the bottom panel is boxed in red. Other spaxels contaminated by improper cosmic ray removal in the rectification matrix are boxed in yellow. *Bottom:* Section of the spectrum from the reduced sky cube, at the position shown by the red box in the top panel. In *red* is the spectrum from the cube reduced using the old rectification matrix, still contaminated by cosmic rays. In black is the same spectrum, reduced using the new rectification matrix that has been corrected for cosmic rays. The dashed vertical line shows the spectral channel represented by the map at top.

4.4 FLUX ASSIGNMENT ARTIFACTS

The *Spectral Extraction* DRP module (`spatrectif`) works to model the spectral PSF from each lenslet (which has a one-to-one correspondence with a single spaxel) using the average 1D PSF in the spatial direction, as further described in Section 4.1.1. The current spectral extraction routine does not model the 2D structure of the PSF, which means that any asymmetries in the PSF will not be accounted for in the wavelength direction. Problems with the flux assignment algorithm were first noted beginning in December 2012, after OSIRIS moved to the Keck I telescope and the new grating was installed. These issues manifested in reduced data cubes in both the *spatial* direction, with artifacts affecting the total flux in neighboring spaxels, and in the *spectral* direction, with artifacts appearing over a limited wavelength range in neighboring spaxels. In this section we describe the symptoms and problems seen with flux assignment artifacts with on-sky data sets, engineering data, and then follow with discussion on potential causes to the problem and future solutions.

4.4.1 Quasar data

Flux assignment artifacts (both spatial and spectral) are evident in the QSO data taken between 2014 and 2015 using the 100 mas plate scale, as further described in Section 4.2.1. These artifacts are easily seen in broad-line Hα emission from the quasar which should be represented by a broad Gaussian function ($\sim$3000 km s^{-1}). Instead, in some individual spaxels the broad-line Hα emission had large discrepant dips, and other spaxels showed unusual-looking spectra. In Figure 4.5, the 3C 298 reduced data cube, collapsed in the wavelength direction, is shown with the spectra from two spaxels highlighted. Spaxel A marks the spectrum at the center of the flux distribution showing the expected broad-line Hα emission. The spectrum in the nearby spaxel B shows an unphysical dip at the location of the broad-line Hα emission; this spaxel should look nearly identical to spectrum A but at a lower integrated intensity. Other neighboring spaxels at the core of the 3C 298 QSO have unusual spectra that also deviate from the integrated spectrum of a normal broad-line

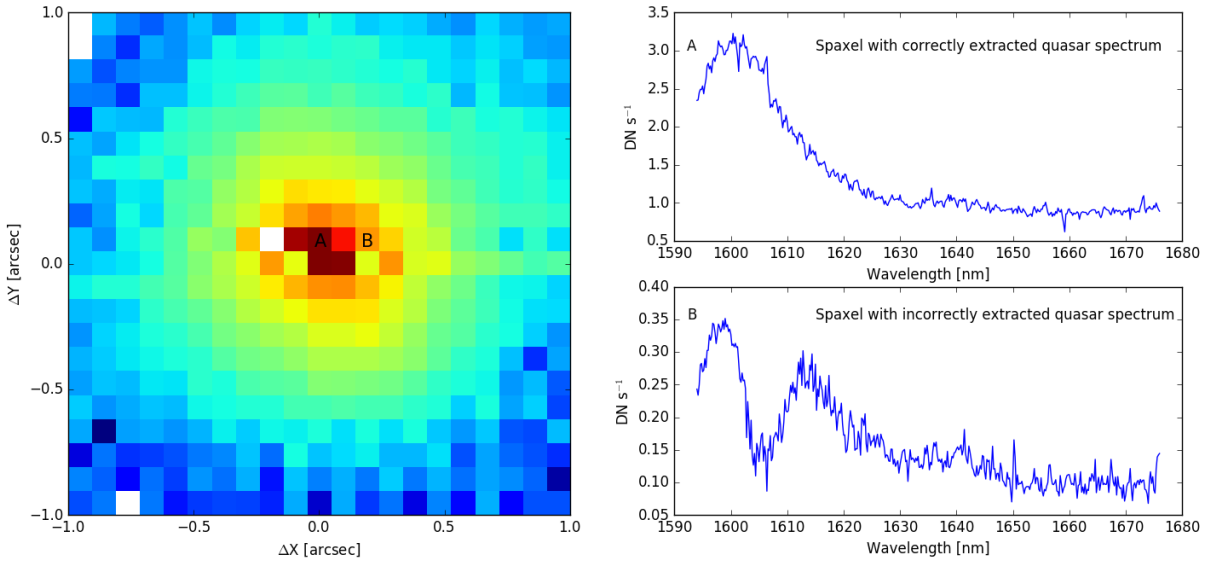

Figure 4.5 Flux mis-assignment example for the 3C 298 quasar observed in 100 mas plate scale with Hn3 filter. *Left:* The collapsed data cube of the obesrvations showing the spatial PSF of the quasar; a number of spaxels show flux that is considerably different from the neighboring spaxels. These spaxels typically have spectra that with spectral artifacts, such as a missing broad Hα feature. *Top right:* Spaxel A exhibits the correct spectrum, complete with the characteristic broad Hα emission line that originates from the quasar broad-line region. *Bottom right:* The spectrum from spaxel B shows a large unphysical dip at 1605 nm and is missing flux from the broad line Hα emission. Spaxel A and B should be virtually identical, with broad Gaussian emission lines, and should only deviate by total integrated intensity.

region quasar. This 2014 data set signaled that there were major issues with the spectral extraction routine and flux assignment.

One of the leading culprits for these flux assignment artifacts is differences between the PSF of on-sky data sets and of the white light scans used to create the rectification matrices. The calibration unit that feeds the Keck AO system and instruments with continuum and arc lamp light sources includes an integrating sphere and a simulated Keck pupil. If there are any deviations between the calibration unit pupil and the on-sky pupil, this will directly effect the spectral PSF's shape and the location of spectra on the detector. Using calibration data and on-sky observations we investigated the differences between the spectral PSFs. At

the 100 mas plate scale there is a small shift or translation between the white light scans and the science data. In addition, the widths of the PSFs of the white light scans are different from that of the on-sky science data.

We investigate this effect by comparing the quasar continuum emission location on the raw detector to that of the white light scan for the same lenslet. We fit a Gaussian profile both to the quasar continuum spectrum on the raw detector and to the white light scan in the spatial direction, perpendicular to the dispersion direction. We find that in the Kn1 filter the peak of the quasar continuum emission is translated by 0.53 pixels in the spatial direction from the white light scan at a given wavelength. Furthermore, we find that the Gaussian profile fit to the white light scan is broader by $\sim$0.2 pixels compared to the on-sky PSF. Applying a shift to the quasar spectrum and blurring the on-sky data in the spatial direction to match the location and width of the white light scan improves the reduced data cubes. In Figure 4.6, we demonstrate the results of this process using the continuum of the quasar 3C 9. In the original data cube (top panels), spaxel A shows a spectrum that does not resemble the expected quasar broad emission line (upper right panel). The collapsed data cube (upper left) shows inappropriately dark spaxels, due to incorrectly extracted flux. After applying the shift and blur to the on-sky raw data and re-reducing, we see the expected broad emission line in the quasar spectrum (bottom right panel) and the spatial artifacts disappear, showing the expected spatial point-source profile (bottom left).

It is important to note that these tests make use of the 100 mas plate scale, where the on-sky pupil is slightly different than that of the calibration unit. OSIRIS' four spatial scales ($0\farcs02$, $0\farcs035$, $0\farcs05$, and $0\farcs1$) are achieved by swapping in matched pairs of lenses that magnify the images onto the lenslet array, and have an effective pupil size matched to each beam size. This leads to differences in sensitivities and backgrounds for each of the four spatial scales.

Each of the three fine scales ($0\farcs02$, $0\farcs035$, $0\farcs05$) have cold pupil stops mounted within the camera wheel, while the coarse scale ($0\farcs1$) has a fixed cold stop permanently mounted

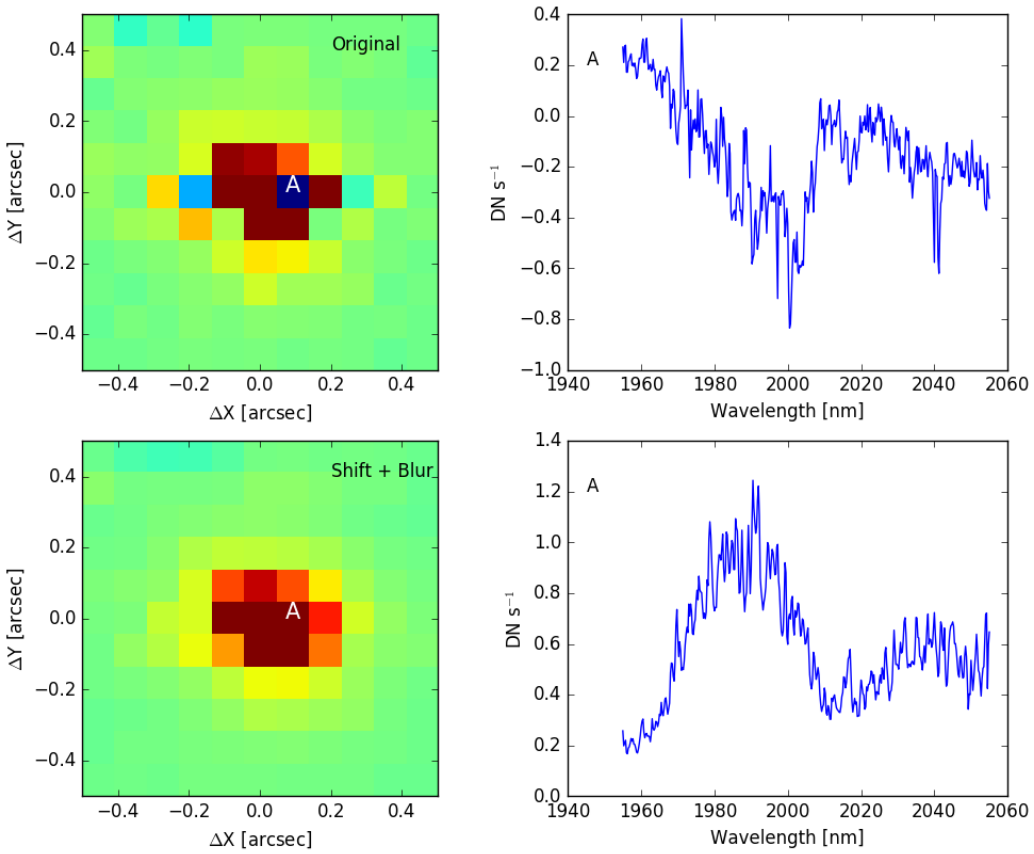

Figure 4.6 Integrated images of differing reductions of the 3c 9 quasar and the associated spectra. *Top left:* Collapsed data cube; abherently low-flux spaxels are visible near the quasar center. *Top right:* Spectrum from spaxel A at left. The spectrum shows an unphysical Hα feature. *Bottom left:* Collapsed data cube after correction of the rectification matrix. The PSF of the quasar is smoother. *Bottom right:* Spectrum from spaxel A in the correctly reduced data cube. The Hα feature is now as expected.

in the optical path[3]. This has the unfortunate effect that the 0.″1 pupil must be oversized to ensure that when using other spatial scales their beams do not vignette. This was a known issue at the time of delivery, but will cause minor mismatch between the calibration and on-sky PSFs and higher thermal noise. Indeed the 100 mas reductions were cleaner and did not have these flux assignment artifact issues before 2012 when OSIRIS was on Keck-2 with the old grating. To date, we believe that the pupil change between Keck-2 and Keck-1 calibration unit may be a significant cause of the problem, as we further discuss in Section 4.4.3.

4.4.2 Arc lamps

Issues with the flux assignment algorithm in the spectral direction are most evident in the presence of a bright emission line. Here, the flux assignment artifacts manifest as increased noise in neighboring spaxels, shifted by 32 spectral channels away from the line. Figure 4.9 shows a single-column arc lamp spectrum. The top panel is a channel map centered on a bright emission line. The bright horizontal row represents the column of lenslets that have been illuminated by the arc lamp, while the dark spaxels are lenslets that were masked during this exposure. The bottom 3 panels show the region of the spectrum around the channel shown at top in each of the three boxed spaxels. The center spectrum is from an illuminated spaxel and the upper and lower spectra are from the dark neighboring spaxels. Increased noise from the flux assignment artifacts can be seen in the dark spaxels, shifted by 32 channels from the bright line.

The 32 channel shift is due to the stagger in wavelength between neighboring spaxels; when the spectra from the raw detector are assembled into the data cube and the wavelength calibration is applied, this translates into a shift of 32 spectral channels in neighboring

[3]In 2006, the 0.″035 and 0.″05 scale pupils were redesigned, fabricated, and installed to match the mean aperture size of Keck (10.0 m) to lower the thermal background. These new pupils reduced the thermal background by ∼65% with respect to the original pupils. In March 2008, we conducted a servicing mission for OSIRIS to install duplicate K broadband (Kbb) and narrowband (Kn3, Kn4, Kn5) filters in the filter wheel with new smaller pupils attached (9 m, effective). These K-band filters with their pupils are optimized to only work with the 0.″1 lenslet scale, and are referred to as Kcb, Kc3, Kc4, and Kc5 within the software, where "c" stands for "coarse."

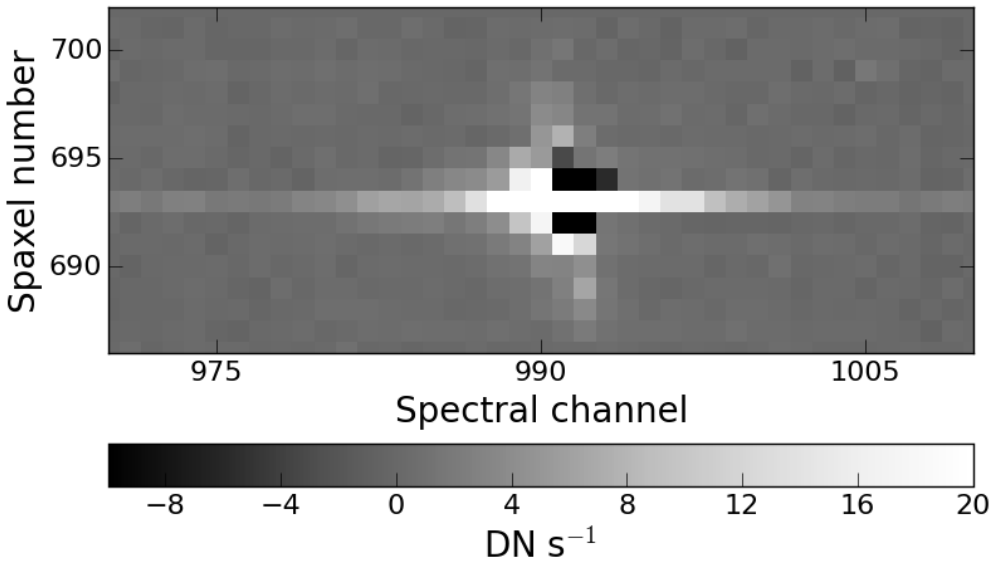

Figure 4.7 Example of flux assignment artifacts, shown after the raw flux has been assigned to a single spaxel but before wavelength calibration or assembly into a cube. A section of a September 2016 reduced Kbb 50 mas single-column arc lamp frame centered on a bright emission line is shown, so all flux should fall in spaxel 693. Each row corresponds to an individual spaxel, while each column corresponds to a spectral channel. The wavelength solution has not yet been applied so there is not a one-to-one correspondence between channel number and wavelength. Neighboring spaxels are shifted by 32 spectral channels with respect to each other. Residual flux above and below the bright emission line at roughly channel 990 is evidence of flux assignment artifacts. The shape of the artifacts reflects the shape of the 2D PSF.

spaxels. The flux assignment artifacts are thus more easily pictured without this wavelength calibration applied. Figure 4.7 shows a segment of a single-column arc, centered on a bright emission line. Flux has been assigned to a specific spaxel but the wavelength calibration has not yet been applied. Each row corresponds with one spaxel, and each column with a column on the raw detector. As this is a single-column arc, all flux in this given frame segment should fall in spaxel 693. However, positive and negative artifacts are evident both above and below the emission line in the illuminated spaxel. These are the cause of the artifacts in the dark spaxels seen in figure 4.9.

The positive and negative artifacts around the bright emission line show a clear asymmetry—positive artifacts are preferentially seen blueward of the emission line peak while negative artifacts appear redward of the line peak. This artifact shape corresponds with the PSF of lines on the raw detector. Figure 4.8 shows the supersampled PSF of a bright arc lamp emission line, which was constructed by stacking the raw 2D detector image of this line in all spaxels in a single detector frame and supersampling it by a factor of 100. The gray boxes mark the scale of the detector pixels. The PSF is asymmetric and flared towards the left, reflecting a coma from the instrument optics. The correspondence between the flux assignment artifacts and the PSF reflects the cause of the artifacts: the rectification matrix is constructed using white light scans to estimate the PSF perpendicular to the dispersion direction. It then uses this PSF estimate to assign flux iteratively from the detector into the correct spaxel. However, this method effectively smooths or averages the PSF at each spectral channel. So the white light PSF is too narrow at the blue wing of a bright emission line compared to the point source PSF and too wide at the red wing of the same, producing the flux assignment artifacts. When the wavelength calibration is applied, these artifacts get shifted to +/- 32 spectral channels.

From testing, it appears that flux is conserved in the presence of spectral flux assignment artifacts. An aperture on a bright emission line in the detector frame, before flux assignment, shows roughly the same amount of flux as appears in the integrated emission line in the final data cube. The positive and negative artifacts thus mostly cancel each other out. However,

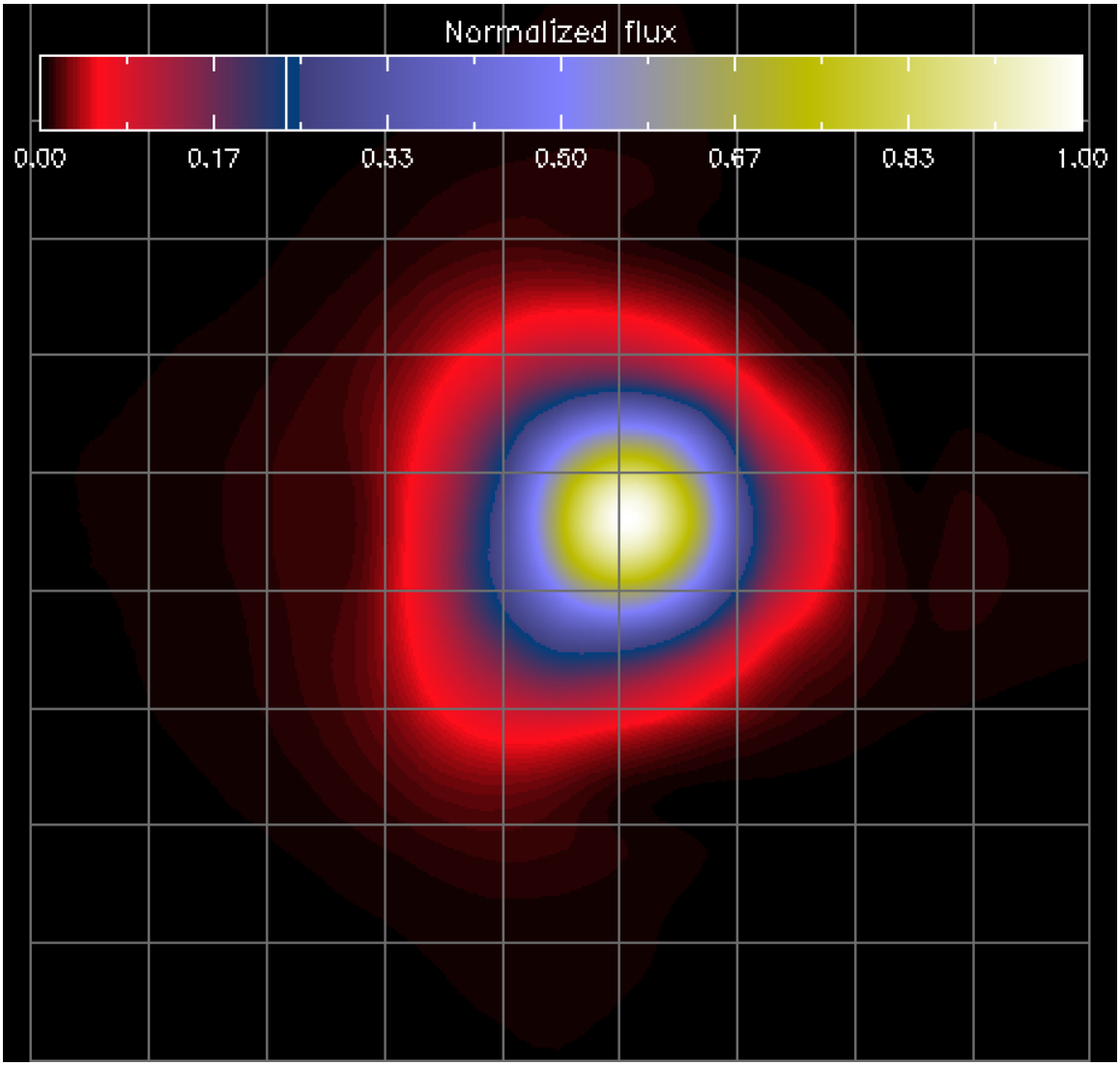

Figure 4.8 PSF on the detector, supersampled by a factor of 100. This PSF is derived from a single bright emission line in March 2016 Jbb/50 mas arc lamp data; the centroid of the given emission line has been found in every spectrum on the detector and all emission line images have been stacked and added. Gray lines represent the detector pixel boundaries, for scale. The asymmetry of the PSF is apparent.

Table 4.2. Flux Assignment Artifacts

Period	Data type	Absolute value of peak artifacts -1 spaxel	+1 spaxel
2012–2015	arc	6.5%	5.4%
2012–2015	sky	2.1%	3.0%
2016–present	arc	2.1%	5.7%
2016–present	sky	2.6%	6.2%

this issue induces extra noise due to artifacts from both emission lines in the science data and from OH sky lines.

In addition, the level of the artifacts has changed with time. We create a metric to measure the level of the flux assignment artifacts with time. We measure the absolute value of the peak of the flux assignment artifacts resulting from a bright emission line as a percentage of the peak of the line itself. As the artifacts can be asymmetric, we measure the artifacts separately in the two neighboring spaxels. We calculate this metric separately for both arc lamp and sky spectra. As the sky spectra are generally much lower in S/N than the arc lamps, we calculate the metric on a median spectrum of a column of spaxels in the sky cube. For the arc lamps, the metric is calculated separately on each individual spaxel. We report the median values from our investigation for each observation type and time period in table 4.2.

Prior to December 2012, the artifacts were much smaller but this issue became more prominent after the grating upgrade. The effect has lessened somewhat since the most recent hardware upgrade, the detector replacement in 2016, but is still a stronger effect than it was prior to 2012.

4.4.3 Diagnosis & Potential solutions

We're investigating possible solutions for the flux assignment artifacts. Flux appears to be conserved, but the additional noise may be a concern. In addition, the placement of the artifacts, if they fall on a spectral feature of interest, may impact science measurements.

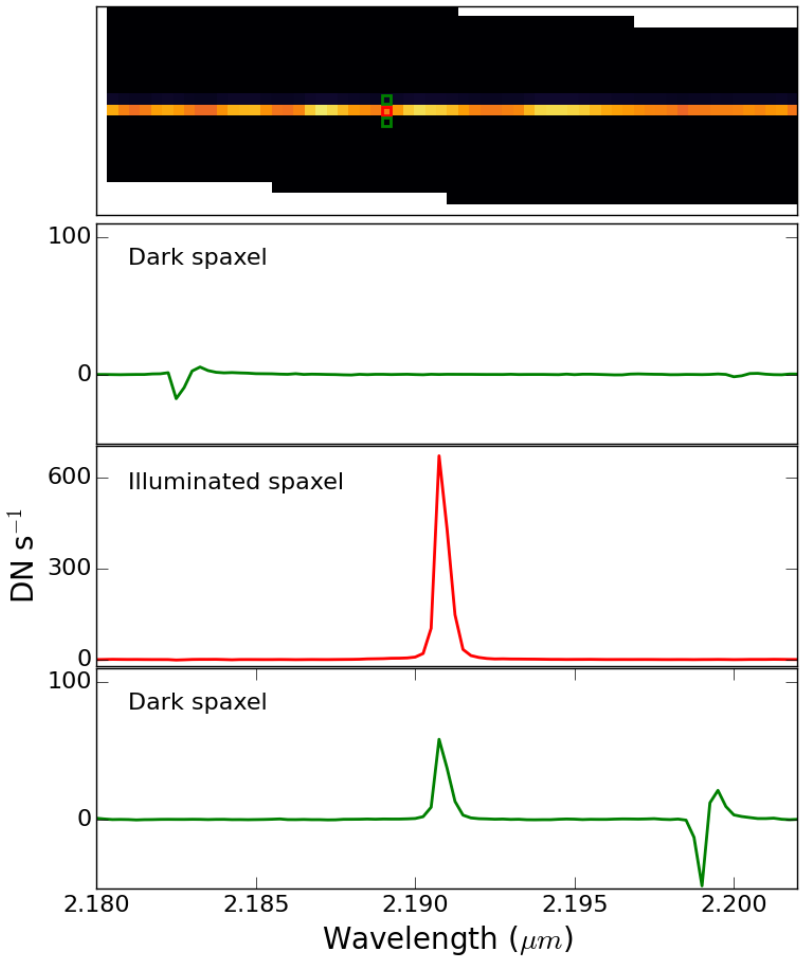

Figure 4.9 Example of flux assignment artifacts in a September 2106 single-column arc lamp spectrum, taken with the Kbb filter and plate scale 0.″035. Flux is conserved in the correct spaxel, but flux assignment artifacts are visible at ±32 spectral channels in adjacent spaxels. *Top panel:* Spectral channel map at 2.191 μm, the peak of a bright Kr emission line. Only one column of lenslets is illuminated. The green boxes mark the two dark spaxels whose spectra are shown at right, while the red box marks the shown illuminated spaxel. *Bottom panels:* Segment of a spectrum in the three adjacent spaxels indicated in the channel map. *Second panel:* Dark spaxel adjacent to an illuminated spaxel. This spaxel should show no flux, but negative artifacts are visible. The artifacts are offset by -32 spectral channels from the emission line in the middle panel. *Third panel:* Illuminated spaxel. *Bottom:* Dark spaxel adjacent to an illuminated spaxel. This spaxel should not show flux, but positive and negative artifacts are visible. The blue artifacts are at the same spectral channel as the emission line in the middle panel, while the red artifacts are offset by +32 spectral channels.

However, the ultimate cause is likely the method of assigning flux to spaxels (e.g. the white light scans and rectification matrices). Ultimately, an implementation of a two-dimensional PSF estimation and spectral extraction algorithm may be necessary, though the task is non-trivial. We would need a 2D estimate of the PSF on the detector for every spaxel and wavelength combination. However, as the internal structure of OSIRIS is fixed, we can currently only sample the 1D PSF. The CHARIS IFS on Subaru utilizes a tunable laser to sample the 2D PSF at all wavelengths (Brandt et al. 2017); something similar would need to be installed on OSIRIS to implement a 2D flux extraction algorithm.

4.5 SPATIAL RIPPLING

Individual spectral channel maps in the reduced OSIRIS cubes show spatial rippling, or a pattern of brighter and fainter spaxels unrelated to incident flux. The spatial rippling is especially apparent for bright emission lines, is wavelength dependent, and changes rapidly with wavelength. Figure 4.10, left panels, shows an example of this rippling. Each panel is a 2D cut at a single wavelength channel in a reduced arc lamp cube. The three channels shown are each centered on a bright emission line in this bandpass.

The rippling pattern is roughly consistent at a single spectral channel across filters and pixel scales, with some magnification, and stays roughly consistent with time. However, the scale of the rippling, or the magnitude difference between the bright and faint spaxels in the pattern, has changed with time. In particular, it was much less evident before the grating upgrade in 2012.

The spatial rippling is caused by the subsampled PSF on the detector. Figure 4.10, right panels, shows the pixel phase of the bright emission lines in the corresponding left panels. These pixel phases are measured in the dispersion direction on the raw detector. In this color scheme, lighter colors represent a line that is more centered on a given detector pixel, while darker colors represent a line that falls closer to the edge of a pixel.

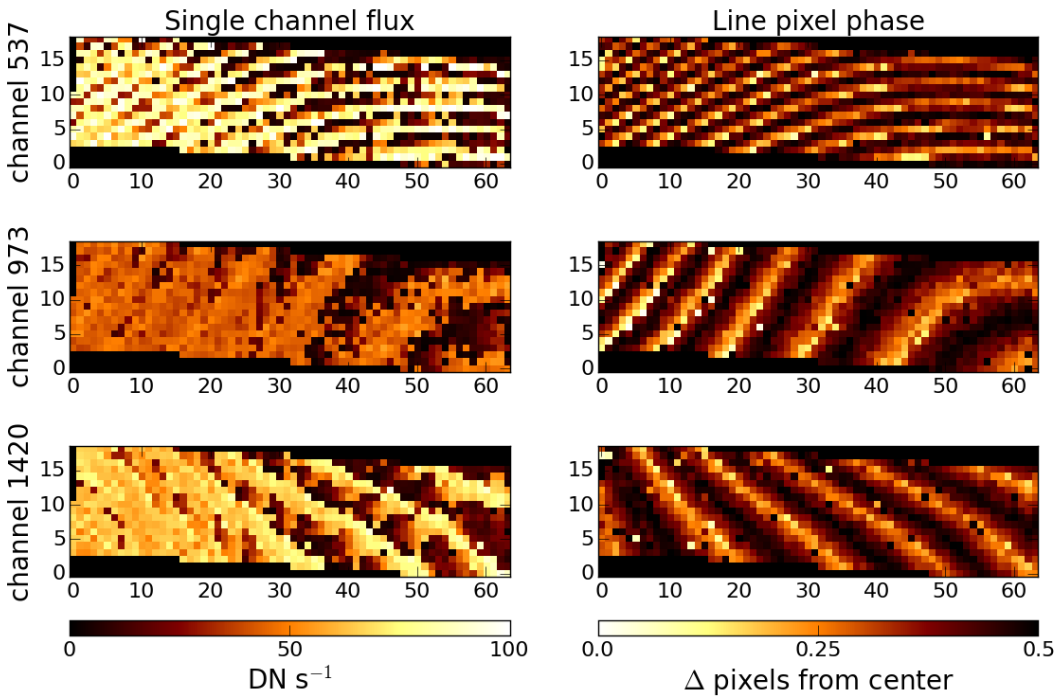

Figure 4.10 A pattern of spatial rippling, best seen in bright emission line single-channel maps, is caused by the undersampled PSF in the dispersion direction on the raw detector. *Left:* Single channel maps from a reduced Kbb/50 mas arc lamp cube from December 2015. Selected channels are chosen at the peak of several bright emission lines. *Right:* Pixel phase of the emission lines (*left*) along the dispersion direction on the detector. Units are the absolute value of the pixel phase; lighter colors indicate a more centered emission line, while darker colors indicate an emission line whose peak falls near the edge of a pixel.

The correspondence between the pixel phase of a given emission line and its channel map is due to the narrowness of the PSF on the detector. After the 2012 grating upgrade, the focus on the detector was sharpened along the dispersion direction, leading to a PSF that is subsampled in the dispersion direction. Emission lines that are centered on a pixel have more of their flux assigned to a single spectral channel in the reduced cube, while lines that fall at the edge of a pixel have their light split across two channels. This leads to the rippling in the reduced cube channel maps.

The rippling pattern can affect science data, particularly because the pattern changes rapidly. Figure 4.11 shows single channel maps across one arc lamp emission line. The channel corresponding to the peak of the line is shown in the center panel, and the maps corresponding to the line wings are shown in the top and bottom panels. Without blinking the images, differences between neighboring channels are difficult to detect by eye; however, comparing the three panels, separated by up to five spectral channels, shows visible differences. The bottom panel of figure 4.11 shows a vertical 10-spaxel wide cut along the right side of all three panels, normalized so the median flux in each profile is equal to one. The bright bands in each channel are shifted by 1–2 rows with respect to each other. This change of pattern with wavelength induces extra noise into the cube, and may affect measurements such as kinematics or channel maps.

While individual channel maps show a strong rippling pattern, integrated line flux is conserved in data from most epochs. However, data taken in the period from December 2012 to December 2015 is subject to a stronger spatial rippling pattern that does not resolve after integrating over the emission line. Figure 4.12 shows the peak and integrated line flux of an OH sky line in frames taken in 2013 and in 2016. In 2016 (bottom panels), while the rippling pattern is evident in single channel maps, the integrated line maps are smooth. On the other hand, integrated emission line maps from 2013 data (top panels) show spatial rippling in both the single channel and in the integrated flux maps. The PSF in the dispersion direction is slightly narrower in the period between December 2012 and December 2015 than in the current configuration; during the 2016 detector upgrade, the

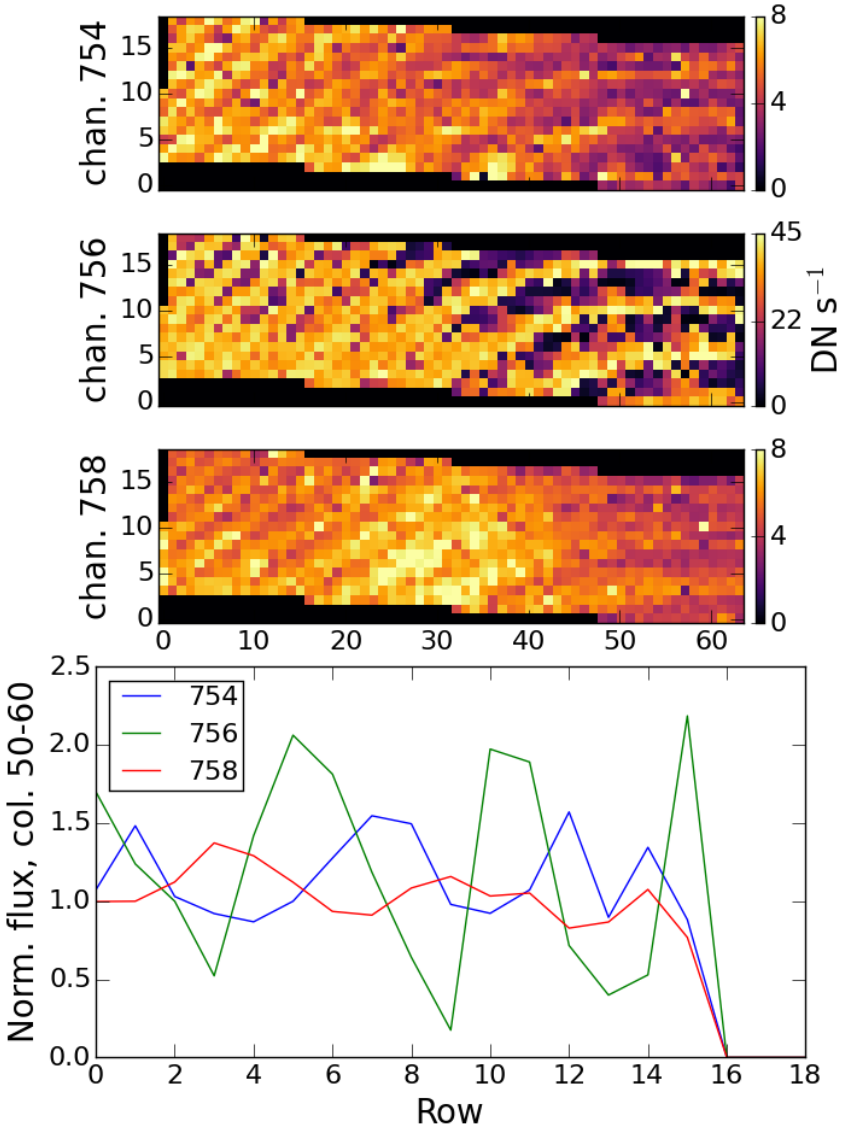

Figure 4.11 The spatial rippling patterns change from channel to channel. *Top:* Channel maps across a single emission line, at the peak of the line and at 2 channels away on either side. The change in rippling pattern with wavelength is quite apparent, particularly when comparing the right sections of the top and bottom panels. *Bottom:* Vertical cuts across all three channel maps, taken between columns 50 and 60 (columns have been median combined). The cuts have been normalized for display. The vertical position of the horizontal stripes is different in the three channels.

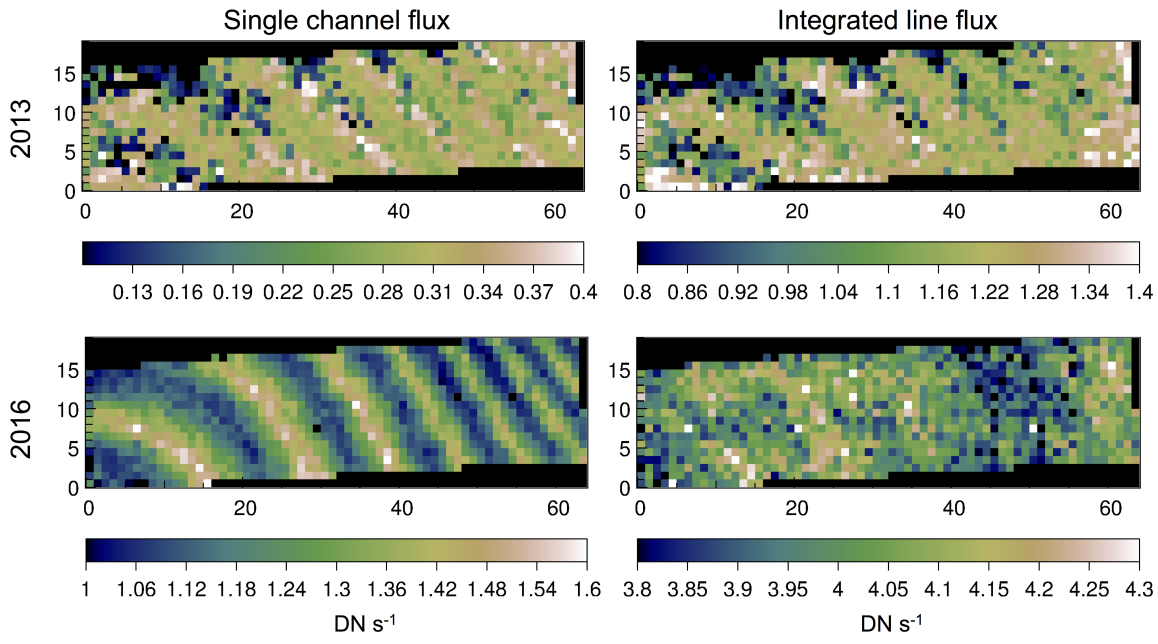

Figure 4.12 *Left:* Single channel maps of a OH line (2.196 μm, channel 925) from a reduced Kbb/35 mas sky cube from May 2013 (*top*) and May 2016 (*bottom*). *Right:* integrated flux over 10 channels (920–930).

PSF elongation was rotated so as to be broadened slightly in the dispersion direction. In addition, during the period from December 2012 to December 2015, the PSF perpendicular to the dispersion direction was wider. The confluence of the flux assignment algorithm issues plus the PSF subsampling is the most likely cause of the persistent rippling seen in integrated flux maps.

4.5.1 Potential solutions

In most data epochs, the spatial rippling issue is a nuisance but does not affect science data. Integrated line maps do not contain a residual rippling pattern, though single channel maps may. In addition, if emission lines are intrinsically broadened, as for some science cases, the lines may be sampled sufficiently to produced smooth single channel maps without integration. However, caution must be used with data taken between December 2012 and December 2015 that contains narrow emission lines, potentially including OH sky lines. Examination of single channel and integrated line maps of these sharply peaked lines may show this rippling pattern.

4.6 RECOMMENDATIONS

Many of the issues we've outlined here for the OSIRIS DRP also have the potential to be of concern for the data pipelines for the next generation IFSs, such as IRIS on TMT. We discuss those implications here.

In § 4.3, we discussed the discovery of improper cosmic ray removal in the rectification matrix calibration files. These noisy spikes propagate non-intuitively through the reduction process, particularly in data as complex as those output from IFSs. Without proper treatment before use in data reduction, errant cosmic rays can make affected science data unusable. Care should be taken to clean the calibration files as thoroughly as science data before use.

Perhaps more importantly, we've shown the perils of closely packed spectra on the detector. The deconvolution of raw data is non-trivial, especially when the raw spectra are spaced by a width similar to the FWHM in the spatial direction. In this situation, a 1D spatial rectification algorithm may work with ideal data, but can fall short with real data. In this situation, flux may be misassigned (§ 4.4.1) or cause artifacts in neighboring spaxels (§ 4.4.2). Ultimately, a 1D estimation of the spectral PSF in the spatial direction may not be an accurate enough representation of real data, particularly for point sources. A 2D estimation of the PSF for every spaxel and wavelength may be necessary to fully resolve this issue.

A similar issue involves the PSF of a point source on the detector in the spectral direction. Sharpening the instrumental PSF allows for higher spectral resolution in science observations, but can induce large-scale patterns. In § 4.5, we showed that sharpening the spectral PSF to the point of undersampling introduced a spatial rippling effect. This pattern is most evident in single channel maps in reduced data cubes, but when in combination with inadequate spatial rectification, the same pattern can appear in integrated line maps, leading to larger uncertainties in integrated line quantities.

The complexity of IFS raw data outputs means that upcoming IFSs should consider the ease of data reduction from the beginning. Incorporating the lessons learned from the OSIRIS DRP will greatly improve the ease of data reduction and resulting data quality for future IFS instrumentation.

The data presented herein were obtained at the W.M. Keck Observatory, which is operated as a scientific partnership among the California Institute of Technology, the University of California and the National Aeronautics and Space Administration. The Observatory was made possible by the generous financial support of the W.M. Keck Foundation. The authors wish to recognize and acknowledge the very significant cultural role and reverence that the summit of Maunakea has always had within the indigenous Hawaiian community.

References

Barman, T. S., Macintosh, B., Konopacky, Q. M., & Marois, C. 2011, ApJ, 733, 65

Boehle, A., Larkin, J. E., Adkins, S. M., Aliado, T., Fitzgerald, M. P., Johnson, C. A., Lyke, J. E., Magnone, K. G., Sohn, J. M., Wang, E., & Weiss, J. L. 2016, in Proc. SPIE, Vol. 9908, Ground-based and Airborne Instrumentation for Astronomy VI, 99082Q

Bowler, B. P., Liu, M. C., Dupuy, T. J., & Cushing, M. C. 2010, ApJ, 723, 850

Brandt, T. D., Rizzo, M., Groff, T., Chilcote, J., Greco, J. P., Kasdin, N. J., Limbach, M. A., Galvin, M., Loomis, C., Knapp, G., McElwain, M. W., Jovanovic, N., Currie, T., Mede, K., Tamura, M., Takato, N., & Hayashi, M. 2017, ArXiv e-prints

Brown, M. E. & Hand, K. P. 2013, AJ, 145, 110

Davies, R. I. 2007, MNRAS, 375, 1099

Do, T., Martinez, G. D., Yelda, S., Ghez, A., Bullock, J., Kaplinghat, M., Lu, J. R., Peter, A. H. G., & Phifer, K. 2013, ApJ, 779, L6

Jones, T. A., Swinbank, A. M., Ellis, R. S., Richard, J., & Stark, D. P. 2010, MNRAS, 404, 1247

Konopacky, Q. M., Barman, T. S., Macintosh, B. A., & Marois, C. 2013, Science, 339, 1398

Krabbe, A., Gasaway, T., Song, I., Iserlohe, C., Weiss, J., Larkin, J. E., Barczys, M., & Lafreniere, D. 2004, in Proc. SPIE, Vol. 5492, Ground-based Instrumentation for Astronomy, ed. A. F. M. Moorwood & M. Iye, 1403–1410

Krabbe, A., Gasaway, T. M., Weiss, J., Larkin, J. E., Barczys, M., Quirrenbach, A., & LaFreniere, D. 2002, in Proc. SPIE, Vol. 4847, Astronomical Data Analysis II, ed. J.-L. Starck & F. D. Murtagh, 448–451

Larkin, J., Barczys, M., Krabbe, A., Adkins, S., Aliado, T., Amico, P., Brims, G., Campbell, R., Canfield, J., Gasaway, T., Honey, A., Iserlohe, C., Johnson, C., Kress, E., LaFreniere, D., Lyke, J., Magnone, K., Magnone, N., McElwain, M., Moon, J., Quirrenbach, A., Skulason, G., Song, I., Spencer, M., Weiss, J., & Wright, S. 2006, in Proc. SPIE, Vol. 6269, Society of Photo-Optical Instrumentation Engineers (SPIE) Conference Series, 62691A

Laver, C. & de Pater, I. 2009, , 201, 172

Laver, C., de Pater, I., Marchis, F., Ádámkovics, M., & Wong, M. H. 2009, , 204, 574

Law, D. R., Steidel, C. C., Erb, D. K., Larkin, J. E., Pettini, M., Shapley, A. E., & Wright, S. A. 2009, ApJ, 697, 2057

Lu, J. R., Do, T., Ghez, A. M., Morris, M. R., Yelda, S., & Matthews, K. 2013, ApJ, 764, 155

McConnell, N. J., Ma, C.-P., Gebhardt, K., Wright, S. A., Murphy, J. D., Lauer, T. R., Graham, J. R., & Richstone, D. O. 2011, Nature, 480, 215

Medling, A. M., Ammons, S. M., Max, C. E., Davies, R. I., Engel, H., & Canalizo, G. 2011, ApJ, 743, 32

Mieda, E., Wright, S. A., Larkin, J. E., Graham, J. R., Adkins, S. M., Lyke, J. E., Campbell, R. D., Maire, J., Do, T., & Gordon, J. 2014, PASP, 126, 250

Stark, D. P., Swinbank, A. M., Ellis, R. S., Dye, S., Smail, I. R., & Richard, J. 2008, Nature, 455, 775

Vayner, A., Wright, S. A., Do, T., Larkin, J. E., Armus, L., & Gallagher, S. C. 2016, ApJ, 821, 64

Walsh, J. L., van den Bosch, R. C. E., Barth, A. J., & Sarzi, M. 2012, ApJ, 753, 79

Wright, S. A., Larkin, J. E., Barczys, M., Erb, D. K., Iserlohe, C., Krabbe, A., Law, D. R., McElwain, M. W., Quirrenbach, A., Steidel, C. C., & Weiss, J. 2007, ApJ, 658, 78

Yelda, S., Ghez, A. M., Lu, J. R., Do, T., Meyer, L., Morris, M. R., & Matthews, K. 2014, ApJ, 783, 131

Chapter 5

Conclusions

Our ability to resolve the centers of galaxies greatly affects our ability to understand the mechanisms by which they can affect galactic evolution and by which they themselves can form stars and evolve. In this dissertation, we have used high spatial resolution imaging and integral field spectroscopy to explore the central regions of two local galaxies. We also have presented work to characterize and improve the DRP of the OSIRIS IFS, which has proved vital to this work.

5.1 The connection between Arp 220's nucleus and its galactic outflow

In chapter 2, we presented new HST/WFC3 optical narrowband imaging of Arp 220. After continuum subtraction, we extracted optical emission line maps of the system. We discovered a previously unresolved bubble structure in Hα+[NII] 375 pc northwest of the western SMBH. Comparison with NIR kinematics shows that the bubble is coincident with increased velocity dispersion in the nuclear gas disk. We calculated the energy necessary to excite the amount of ionized gas estimated to be in the bubble and found that the most likely drivers of the bubble were the young, obscured AGN in the western nucleus, or the intense nuclear starburst. Via morphology, we conclude that the bubble is associated with both the western nucleus and with the large-scale galactic outflow, thus connecting the nuclear activity with the outflow.

Previous studies (Arribas et al. 2001) had noted the peak in Hα at the location of the bubble, but were unable to resolve its structure and hence firmly connect it to the nuclear region. The resolving power of HST was necessary show the impact of Arp 220's active nuclear region on the galaxy as a whole.

5.2 Star formation in M31's nuclear star cluster

In chapter 3, we presented new Keck/OSIRIS NIR IFS observations of the old stellar eccentric disk of the NSC of M31. We fit stellar templates and a LOSVD to spectra across the FOV and extracted line-of-sight kinematics for the entire old stellar population in the NSC. We confirm that our kinematic results are consistent with previous long-slit observations and lower-resolution IFS observations. We then fit the models of Peiris & Tremaine (2003) to the kinematics to determine the orientation and the precession of the disk. The best-fit orientation to the eccentric disk is more inclined than found previously with optical imaging. The best-fit precession is 0 ± 5 km s^{-1} pc^{-1}. This result is consistent with that predicted by Chang et al. (2007), who theorized that the gas needed to form the younger population in the NSC could come from the winds from the old stellar population in the eccentric disk, but required that the disk be precessing slowly. Given the constraints on the precession imposed by our data and the Peiris & Tremaine (2003) models, we confirm that it is possible for the material needed for star formation within the NSC to come from the NSC itself.

Previous studies (Sambhus & Sridhar 2000; Bacon et al. 2001; Jacobs & Sellwood 2001; Salow & Statler 2001; Sambhus & Sridhar 2002; Salow & Statler 2004) had derived the precession rate for the eccentric disk, but the values ranged from 3 to over 30 km s^{-1} pc^{-1}, with little consistency even for studies using similar methods or data sets. Long-slit studies were hampered by lack of spatial coverage, which led them to use one-dimensional methods for estimating the precession. We showed that these 1D methods can be biased and require calibration. Previous IFS studies were hindered by low spatial resolution, which limited the

power of their modeling. Our data set is the first high spatial resolution data set with the full FOV coverage necessary for this measurement.

5.3 Characterizing and improving the DRP of OSIRIS

In chapter 4, we reported on work to characterize and improve the OSIRIS DRP. The DRP was delivered along with the instrument (Larkin et al. 2006), and for the past decade, DRP maintenance has included only general bug fixes and small changes necessary after hardware upgrades. However, the DRP had not been characterized or substantially improved since delivery. Our characterization showed the importance of the removal of cosmic rays from calibration frames and demonstrated the consequences of packing spectra too closely on the detector. We also show that subsampling the detector PSF in the spectral direction can have unintended consequences for narrow emission line data.

5.4 Future work

Advances in instrumentation will greatly improve the ability of observations to resolve and map the small, complex centers of galaxies in galaxies further from our own. Open questions remain: what other formation mechanisms are available to NSCs? While M31's young nuclear cluster formed via a self-feeding mechanism, two other nearby galactic centers demonstrate different processes. NGC 6946 is host to a nuclear starburst (Tsai et al. 2013) fed by an inflow of gas driven by the galactic bar (Schinnerer et al. 2006). The Milky Way has no such large inflow, but instead hosts a gas reservoir in the form of a circumnuclear cold molecular gas disk ($>10^4$ $M_\odot$, Genzel et al. 1985) with a hot inner edge (Lau et al. 2013; Feldmeier-Krause et al. 2015) within $\sim$5 pc of the SMBH. High resolution integral field spectroscopy of a large sample of nearby galaxy centers is necessary to determine the most common formation mechanisms, and hence answer how NSCs are able to grow in concert with their hosts.

The next generation of IFS are being planned and built for upcoming thirty-meter class telescopes, including IRIS on the Thirty Meter Telescope. With the combination of large aperture size and upgrades in AO capability, these upcoming instruments will be even more powerful than instruments like OSIRIS. With our recommendations for DRP improvements, these instruments may be able to avoid some of the pitfalls of the complex algorithms needed to reduce the output data. Eventually, this next generation of IFSs may answer the question of the formation of NSCs and the connection between galactic centers and their hosts.

References

Arribas, S., Colina, L., & Clements, D. 2001, ApJ, 560, 160

Bacon, R., Emsellem, E., Combes, F., Copin, Y., Monnet, G., & Martin, P. 2001, A&A, 371, 409

Chang, P., Murray-Clay, R., Chiang, E., & Quataert, E. 2007, ApJ, 668, 236

Feldmeier-Krause, A., Neumayer, N., Schödel, R., Seth, A., Hilker, M., de Zeeuw, P. T., Kuntschner, H., Walcher, C. J., Lützgendorf, N., & Kissler-Patig, M. 2015, A&A, 584, A2

Genzel, R., Crawford, M. K., Townes, C. H., & Watson, D. M. 1985, ApJ, 297, 766

Jacobs, V. & Sellwood, J. A. 2001, ApJ, 555, L25

Larkin, J., Barczys, M., Krabbe, A., Adkins, S., Aliado, T., Amico, P., Brims, G., Campbell, R., Canfield, J., Gasaway, T., Honey, A., Iserlohe, C., Johnson, C., Kress, E., LaFreniere, D., Lyke, J., Magnone, K., Magnone, N., McElwain, M., Moon, J., Quirrenbach, A., Skulason, G., Song, I., Spencer, M., Weiss, J., & Wright, S. 2006, in Proc. SPIE, Vol. 6269, Society of Photo-Optical Instrumentation Engineers (SPIE) Conference Series, 62691A

Lau, R. M., Herter, T. L., Morris, M. R., Becklin, E. E., & Adams, J. D. 2013, ApJ, 775, 37

Peiris, H. V. & Tremaine, S. 2003, ApJ, 599, 237

Salow, R. M. & Statler, T. S. 2001, ApJ, 551, L49

—. 2004, ApJ, 611, 245

Sambhus, N. & Sridhar, S. 2000, ApJ, 539, L17

—. 2002, A&A, 388, 766

Schinnerer, E., Böker, T., Emsellem, E., & Lisenfeld, U. 2006, ApJ, 649, 181

Tsai, C.-W., Turner, J. L., Beck, S. C., Meier, D. S., & Wright, S. A. 2013, ApJ, 776, 70